EXPERIMENTAL AND NUMERICAL ANALYSIS OF THE STRAIN RATE DEPENDENT COMPRESSIVE STRENGTH OF A CELLULAR CONCRETE

A Thesis Submitted to
the Graduate School of Engineering and Sciences of
İzmir Institute of Technology
in Partial Fulfillment of the Requirements for the Degree of

MASTER OF SCIENCE

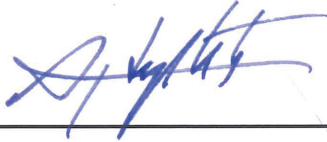in Mechanical Engineering

by
Burak AKYOL

December 2019
İZMİR

We approve the thesis of **Burak AKYOL**

Examining Committee Members:

_____
Prof. Dr. Mustafa GÜDEN

Department of Mechanical Engineering, İzmir Institute of Technology

_____
Prof. Dr. Ali Aydın GÖKTAŞ

Department of Metallurgical and Materials Engineering, Dokuz Eylül University

_____
Assist. Prof. Dr. Selçuk SAATCI

Department of Civil Engineering, İzmir Institute of Technology

6 December 2019

_____
Prof. Dr. Mustafa GÜDEN

Supervisor, Department of
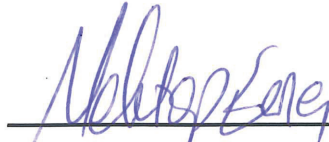Mechanical Engineering
İzmir Institute of Technology

_____
Prof. Dr. Alper TAŞDEMİRCİ

Co-Supervisor, Department of
Mechanical Engineering
İzmir Institute of Technology

_____
Prof. Dr. Sedat AKKURT

Head of the Department of
Mechanical Engineering

_____
Prof. Dr. Mehtap EANES

Dean of the Graduate School of
Engineering and Sciences

ACKNOWLEDGMENTS

ABSTRACT

EXPERIMENTAL AND NUMERICAL ANALYSIS OF THE STRAIN RATE DEPENDENT COMPRESSIVE STRENGTH OF A CELLULAR CONCRETE

Experimental and numerical quasi-static and high strain rate tests, including compression, indentation and direct impact, were performed on a cellular concrete in order to investigate the effect of strain rate on the compressive strength. The results of compression tests indicated three distinct regions of the compressive strength dependence on strain rate. A relatively lower strain rate dependent compressive stress was found in the quasi-static strain rate-regime, 2×10^{-3}-2×10^{-1} s^{-1}, a relatively high strain rate dependent compressive stress in the dynamic strain rate-regime, 180-10^3 s^{-1} and a cut-off strength above 10^3 s^{-1}. The dynamic increase factor (DIF=dynamic/static fracture strength) varied between 1 and 2.5 from quasi-static to dynamic strain rate-regime with a sharp increase after about 100 s^{-1}. The indentation tests using 25 and 30 mm-diameter indenters in the quasi-static strain rate-regime (uniaxial state of strain) and resulted in moderate DIF values (1-1.13), very similar with those of the quasi-static compression tests (1-1.15). In the indentation tests, the DIF values significantly and also confirmed the numerically determined DIF values of concrete at 1000 s^{-1} (~1.30) without radial and axial inertia. The compression and direct impact tests in the Split Hopkinson Bar (SHPB) set-up were implemented numerically in LS-DYNA using an anisotropic strain rate insensitive material model, MAT_096 (MAT BRITTLE DAMAGE). The stress readings were performed at the specimen different locations of the SHPB and indicated that radial and axial inertia were dominant between 1 and 30 m s^{-1} (30-1000 s^{-1}).

ÖZET

GAZ BETONUN DEFORMASYON HIZINA BAĞLI BASMA MUKAVEMETİNİN DENEYSEL VE NÜMERİK ANALİZİ

Gaz betonlar basma, girinti ve direkt çarpma yöntemleriyle deneysel ve nümerik olarak yarı-statik ve yüksek deformasyon hızlarında test edilmiş ve deformasyon hızının basma mukavemeti üzerindeki etkisi gözlemlenmiştir. Basma testleri sonucunda deformasyon hızına bağlı üç farklı basma mukavemeti bölgesi belirlenmiştir. Yarı-statik deformasyon hızında daha düşük hıza dayalı mukavemet artışı gözlenirken ($2x10^{-3}$-$2x10^{-1}$ s^{-1}), yüksek deformasyon hızlarında yapılan testlerde daha yüksek hıza dayalı mukavemet artışı olduğu saptanmıştır (180 s^{-1}-10^3 s^{-1}). 10^3 s^{-1} deformasyon hızından sonra mukavemet artışı sabit kalmıştır. Yüksek deformasyon hızlarındaki mukavemetin yarı-statik deformasyon hızlarındaki mukavemete oranı Dinamik Artış Faktörü (DAF) olarak tanımlanmaktadır. Söz konusu oran yapılan çalışmalar sonucunda 1-2.5 arasında çıkmış ve 100 - 1000 s^{-1} deformasyon hızlarında ani bir artış göstermiştir. 25 ve 30 mm basma uçlarıyla yarı-statik deformasyon hızlarında yapılan girinti testleri makul bir DAF oranı (1-1.15) ile tek eksenli gerinim durumu sağlamış ve basma testlerinin yarı-statik deformasyon hızlarındaki DAF'a (1-1.13) benzer bir sonuç göstermiştir. Deneysel sonuçlar girinti testlerinin DAF'ı düşürdüğünü göstermiştir. Deformasyon hızı etkisinin girilmediği nümerik çalışmalarda 1000 s^{-1}'deki DAF'ın 1.30 olduğu gözlenmiştir. Deneysel basma testleri nümerik olarak LS-DYNA ile deformasyon hızı etkisi olmayan anizotropik malzeme modeli MAT_096 (MAT BRITTLE DAMAGE) kullanılarak modellenmiştir. Farklı hızlardaki mukavemet, numune-bar temas alanındaki merkez ile yüzey elemanlarından ve deneysel çalışmalardaki gerinim ölçerin bulunduğu konumdaki elemandan belirlenmiştir. Radyal ve eksenel ataletin 1 ve 30 m s^{-1} çarpma hızlarında (30-1000 s^{-1}) mukavemet üzerinde etkili olduğu gözlemlenmiştir.

TABLE OF CONTENTS

LIST OF FIGURES

LIST OF TABLES

CHAPTER 1

INTRODUCTION

Aerated concrete (AC) and autoclaved aerated concrete (AAC) are light-weight cellular structures exhibiting relatively high compressive strength, low thermal conductivity, high sound absorption, non-flammability and long-term life utilization. AAC is made of sand, lime, cement and water and was discovered in Sweden in 1923. The first industrial production of AAC started at the beginning of 1930s. Nowadays, AAC is one of the most widely used construction materials, as structural and heat and sound insulating elements. In these applications, AAC may be subjected to dynamic loading during earthquakes, explosions and projectile impacts. So far, the experimental studies on the mechanical behavior of AAC have been performed at quasi-static strain rates, while the mechanical behavior of AAC at high strain rates has not been investigated extensively.

This thesis study was aimed to investigate the mechanical response of an AAC sample from quasi-static (1×10^{-3} s^{-1}) to dynamic (1000 s^{-1}) strain rates. The mechanisms for the strain-rate-sensitive strength behavior were further analyzed in the content of the thesis. The numerical models of the compression tests were further implemented in order to identify the effect of inertia on the compressive strength at increasing strain rates. Various test methods were used in the thesis, including quasi-static and dynamic compression tests, quasi-static indentation tests, quasi-static and dynamic confinement tests and quasi-static and dynamic Brazilian tests. The quasi-static compression tests were performed at the velocities between 5×10^{-5} and 5×10^{-3} m s^{-1}, corresponding to the strain rates of 2×10^{-3} and 2×10^{-1} s^{-1}. The low-velocity impact tests were performed in a Drop Tower at a velocity of 1 m s^{-1}, corresponding to a strain rate of ~30 s^{-1}. The dynamic compression tests were performed in a compression type Split Hopkinson Pressure Bar (SHPB) at the velocities between 8 and 108 m s^{-1}, corresponding to the strain rates between 180 and 4150 s^{-1}. The numerical models of the tests were

implemented at the same velocities with the tests using a strain rate independent material model in order to determine the effect of inertia on the compressive strength. The confinement and indentation tests were performed to determine the compressive strength in a uniaxial state of strain and the Brazilian tests were performed to invastigate the tensile strength variations with strain rates.

CHAPTER 2

AUTOCLAVED AERATED CONCRETE

AC is a light-weight foam, also known as cellular concrete. Its structure, as with other foams is composed of cells, cell walls and cell edges. The main raw materials of AC are sand, lime, cement and water. The process starts with mixing raw materials and water to obtain an expandable viscous slurry. The expansion of slurry is accomplished by using two methods (Figure 2.1). In the first, the expansion is accomplished by injecting an organic or syntactic foam into slurry. The resulting cellular structure is called foamed concrete or non-autoclaved aerated concrete. In the second, a predetermined amount of aluminum powder (foaming agent) is added to slurry. The resultant expanded green structure is later strengthened by autoclaving under a steam pressure at an elevated temperature. During autoclaving, nanoscale tobermorite $(5CaO.6SiQ.5H_2O)$ [1] and well-crystallized C-S-H form as main binding phases. The resultant cellular structure is called AAC. The picture of commercial AAC blocks is shown in Figure 2.2.
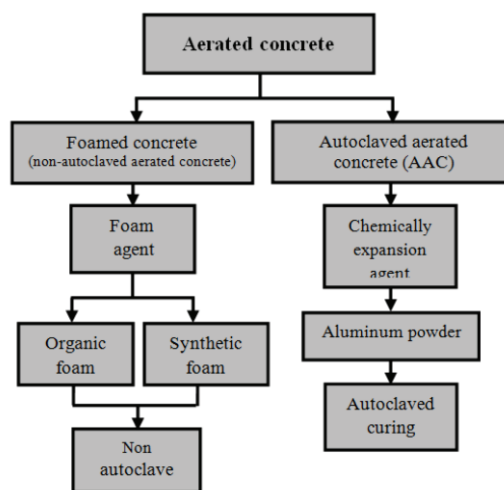
Figure 2.1. Classification of AC [2]

Figure 2.2. The picture of commercial AAC blocks

AAC is a widely used, commercial construction material with bulk densities varying between 150 and 800 kg m^{-3} and the porosities up to 90%. AAC has relatively high strength to weight ratio, good tensile strain capacity, low thermal expansion coefficient and high heat and sound insulation characteristics. Therefore, AAC blocks are widely used in the thermal and sound insulation of buildings and also they are used as structural elements. AAC is normally grouped into brittle cellular ceramics as its cellular structure is composed of varying sizes of pores which crush very easily under compressive loads [3].

2.1. Processing and Microstructure of AAC

The major steps of AAC processing are shown in Figure 2.3. It consists of three steps. Mixing raw materials, foaming the slurry (microstructure formation) and curing the foamed and dried cellular structure (autoclaving). Before autoclaving, the green AAC blocks are sliced into plates or blocks using a wire cutter.

The slurry is foamed by adding Al powder. Aluminum reacts with lime releasing hydrogen gas which expands the slurry with the following reaction [4]

$$2Al\ (s) + 3Ca(OH)_2\ (s) + 6H_2O\ (l) \rightarrow 3CaO.Al_2O_3.6H_2O\ (s) + 3H_2\ (g)$$
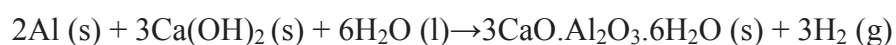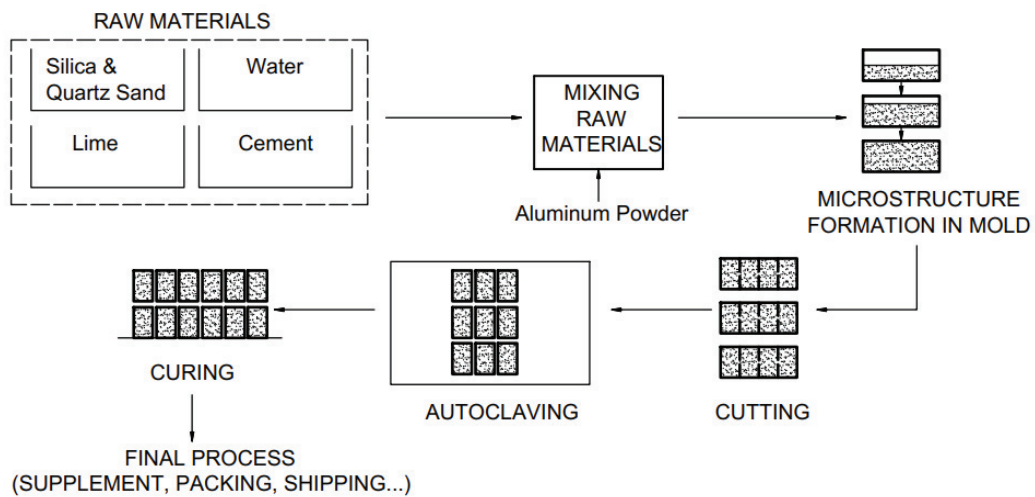
Figure 2.3. Steps of AAC processing

As the reaction between Al powder and hydrated lime continuous, the volume of slurry increases with the release of H_2 gas and a tricalcium hydrate phase forms. The volume expansion depends on the weight percentage of Al powder used and the rheological behavior of slurry. The volume of slurry increases typically 2 to 5 times of the initial volume. Since the hydrogen gas is lighter than air, later in the process, it is replaced by air. Aluminum powder plays a key role in AAC processing because it allows the slurry to be foamed into a uniform structure [5] and it forms a crystalline phase which enhances the strength of AAC. In commercial AAC processing, Al particles are usually in flake-shape with the sizes less than 50 μm (Figure 2.4). The flake-shape increases the surface area of powder which results in increased reaction with lime.

Aluminum dust from aluminum dross recycling industry has been recently investigated for the replacement with the more expansive Al powder in the processing of AAC [6]. The used Al dust particles were irregular in shape, nearly in plate form. Results showed that 15.6 g of Al dust was able to generate the same amount of gas with 1 g of flake-shape Al powder. The used Al dust resulted in smaller pore but could not achieve low densities. Bottom ash was also investigated as foaming agent[7]. Results have shown an increased strength of AAC using bottom ash as foaming agent. The increased strength with the use of bottom ash was attributed to the development of a more uniform and finer pore structure.
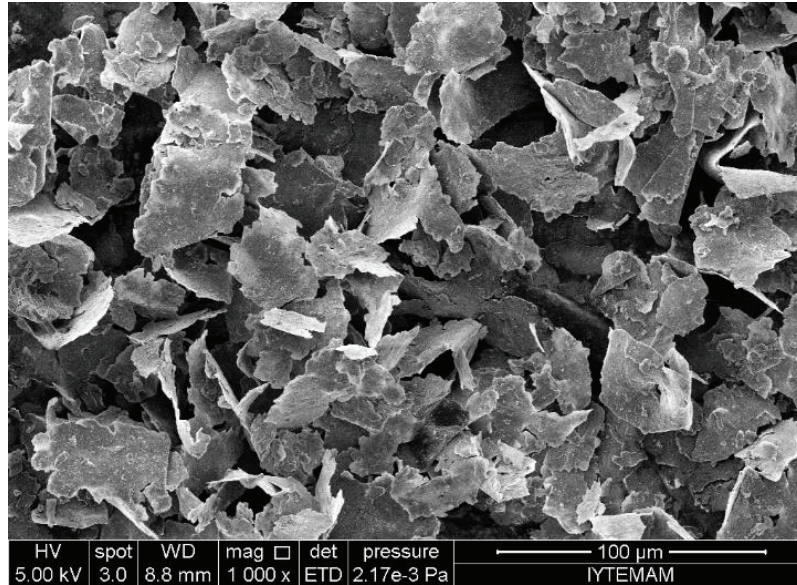
Figure 2.4. The SEM picture of a commercially used Al flake-shape powder in the foaming of AAC slurry

The last step of AAC processing is autoclaving green AAC in a pressurized and steam-heated chamber. Autoclaving is applied at a pressure between 4 and 16 MPa with a duration between 8 and 16 h at $180^{\circ}C$ [2]. Autoclaving reduces the drying shrinkage of AAC by about 6 times [8]. During autoclaving, a crystalline phase known as tobermorite (Figure 2.5) and other crystal phases including hydroganet $[Ca_3Al_2(SiO_4)(OH)_8]$, xonolite $[Ca_6Si_6O_{17}(OH)_2]$ and gyrolite $(Ca_2Si_3O_8 \ 2.5H_2O)$ form depending on temperature, curing time and starting materials [9]. However, tobermorite formation is the most desirable one as it has the highest effect on the strength enhancement of AAC.

Few studies investigated the effect of calcium on the formation of tobermorite and C-S-H phase [11-13]. The Ca/Si ratio played a critical role in the formation and morphology of crystal phases. Higher Ca/Si ratios, greater than 1, tended to form needle-like, while lower ratios, less than 0.8, promoted plate like tobermorite formation [10]. Tobermorite formation increases the strength of AAC [14-16]. Increasing the autoclaving time from 8 to 18 h was shown to have no effect on the formation of tobermorite and the mechanical and microstructural properties of AAC remained stable after 8 h of autoclaving, indicating that the formation of tobermorite was inhibited after 8 h of autoclaving [9]. Increasing pressure in autoclaving increased the tobermorite formation [17]. A reduction in quartz particle size reduced the autoclaving processing time

and promoted gyrolite formation at longer autoclaving times, while the crystallinity of tobermorite increased with increasing quartz particle size [18].
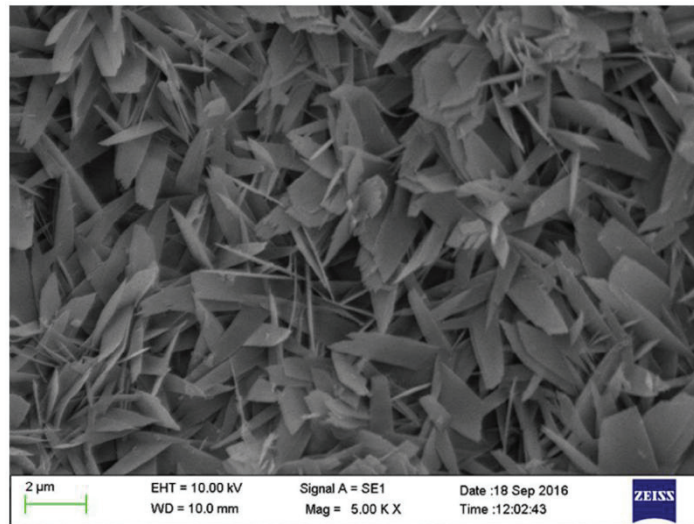
Figure 2.5. The SEM image of AAC prepared at 180°C and 8 h of autoclaving time [10]

In AAC processing, silica sand and lime can be changed with quartz sand and gypsum, respectively. The coarser quartz sand promoted tobermorite formation and increased the strength [18]. The reactants may be changed with additives or replacements and these affect the tobermorite formation. The replacement of coal bottom ash, in the place of quartz sand, increased the tobermorite formation and affected the mechanical properties [19]. Air cooled slag used in the place of lime improved the tobermorite constitution [20]. The water/solid ratio has a significant effect on the microstructure. The smaller ratios decreased pore size and induced higher compressive strengths [7].

The additives are used as reinforcements to enhance the flexural strength of AAC samples (Table 2.1). The additives include hybrid-synthetic fiber [21], bottom ash [14,19,22], stone-sawing mud [5], pulverized bone [23], carbon fiber [24-27], calcium sulfate dihydrate [11], polycarboxylic admixture [3], polypropylene fiber [28], basalt fiber [28] and glass fiber [28]. Although, fiber additives did not affect the tobermorite formation [24], they altered the microstructure of AAC. Few additives also increased the ductility of AAC by altering the microstructure [26,27,29].

Table 2.1. Technical parameters of fibrous additives [10]

Fibrous additive	Average length (mm)	Average diameter (μm)	Tensile strength (GPa)	Density (g/cm³)	Thermal conductivity (W/m·K)	Highest compressive strength ratio of sample with fiber to that without fiber	Highest flexural strength ratio of sample with fiber to that without fiber
Carbon fiber [29]	5	6.15	2.50			1.42[†]	2.32[†]
Polypropene fiber [29]	5	7.50	3.40			1.32[†]	2.06[†]
Basalt fiber [29]	5	4.60	2.50			1.26[†]	1.93[†]
Kaoline fiber [29]	5	3.30				1.08[†]	1.37[†]
Carbon fiber [30,31]	8		3.60–6.20	1.74–1.80	21–180	1.13[‡] 1.23[§] 1.31[‖]	1.53[‡] 1.53[§] 1.61[‖]
Polypropene fiber [30,31]	10		0.55–0.70	0.91	0.11–0.22	1.06[‡] 1.08[§] 1.13[‖]	1.34[‡] 1.32[§] 1.40[‖]
Basalt fiber [30,31]	8		4.15–4.80	2.50–2.80	0.031–0.038	1.10[‡] 1.17[§] 1.22[‖]	1.32[‡] 1.23[§] 1.16[‖]
Glass fiber [30,31]	24		3.45	2.54–2.60	0.034–0.40	1.04[‡] 1.03[§] 1.06[‖]	1.07[‡] 1.10[§] 1.04[‖]

Notes:
[†] The density of AAC sample is 450 kg/m³;
[‡] The density of AAC sample is 600 kg/m³;
[§] The density of AAC sample is 500 kg/m³;
[‖] The density of AAC sample is 400 kg/m³.

2.2. Mechanical Properties of AAC

Most of the studies on the mechanical behavior of AAC were conducted at quasi-static strain rates. ASTM C39/C 39M–03 (Standard Test Method for Compressive Strength of Cylindrical Concrete Specimens) defines the geometry of compression test sample [30]; but, the test sample geometry depends also the type of test applied such as rupture test, split tensile test, compression test and etc [23].

The schematic of the stress-strain response of AAC and fiber reinforced aerated concrete (FRAC) under compressive and tensile loads are shown in Figure 2.6 [27]. Both AAC and FRAC samples crush under compression after a maximum stress with a plateau region usually associated with the progressive crushing at one of the end of sample. However, AAC shows very brittle crushing behavior under tension, while FRAC exhibits fiber bringing which increases the toughness.

Brittle cellular structures show characteristic deformation under compression: a catastrophic failure following a maximum or collapse stress [31]. The collapse stress of brittle cellular structures with closed-cell is given as

$$\sigma_f = \sigma_s[C\varphi\rho_{rel}^{3/2} + (1 - \varphi)\rho_{rel}]$$

(2.1)

where, σ_s is the strength of solid material, C is a constant, ρ_{rel} is the relative density of foam and φ is the volume fraction of the solids contained on plateau borders. The relative density is $\frac{\bar{\rho}}{\rho_s}$, where $\bar{\rho}$ is the density of the foam and ρ_s is the density of the solid. The value of C is given as 0.2 [31]. The first term in Equation 2.1 is due to the bending and the second term is due to the membrane stretching of cells. Equation 2.1 predicts the collapse stress of an open-cell foam when φ is equal to 1, and the collapse stress of a closed-cell foam when φ value is equal to 0.
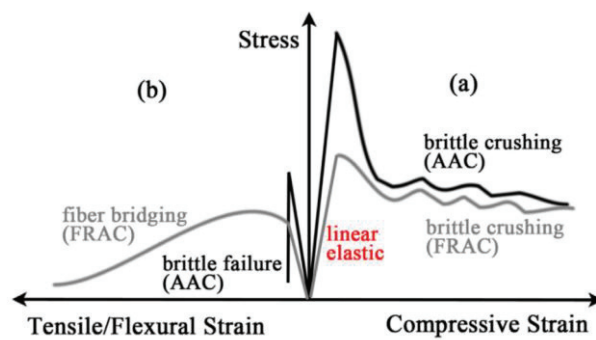
Figure 2.6. The schematic presentation of stress-strain behavior of AAC (FRAC denotes to fiber reinforced AC) [27]

The thermo-mechanical properties of AAC are tabulated at increasing densities in Table 2.2. The compressive strength, elastic modulus and thermal conductivity increase, while drying shrinkage decreases with increasing density. The compressive strength and thermal conductivity of AAC have almost a linear relation with density (Figures 2.7(a-b)). The tensile strength depends on the compressive strength and increases with increasing compressive strength.

Table 2.2. Thermo-mechanical properties of AAC [32]

Dry density (kg/m³)	Compressive strength (MPa)	Modulus of elasticity (E-value) (GPa)	Thermal conductivity (3% moisture) (W/mK)	Drying shrinkage (%)
400	0.5-1.0	0.8-1.0	0.10	0.30-0.35
600	1.0-1.5	1.0-1.5	0.11	0.22-0.25
800	1.5-2.0	2.0-2.5	0.17-0.23	0.20-0.22
1000	2.5-3.0	2.5-3.0	0.23-0.30	0.15-0.18
1200	4.5-5.5	3.5-4.0	0.38-0.42	0.09-0.11
1400	6.0-8.0	5.0-6.0	0.50-0.55	0.07-0.09
1600	7.5-10	10.0-12.0	0.62-0.66	0.06-0.07

(a)   (b)
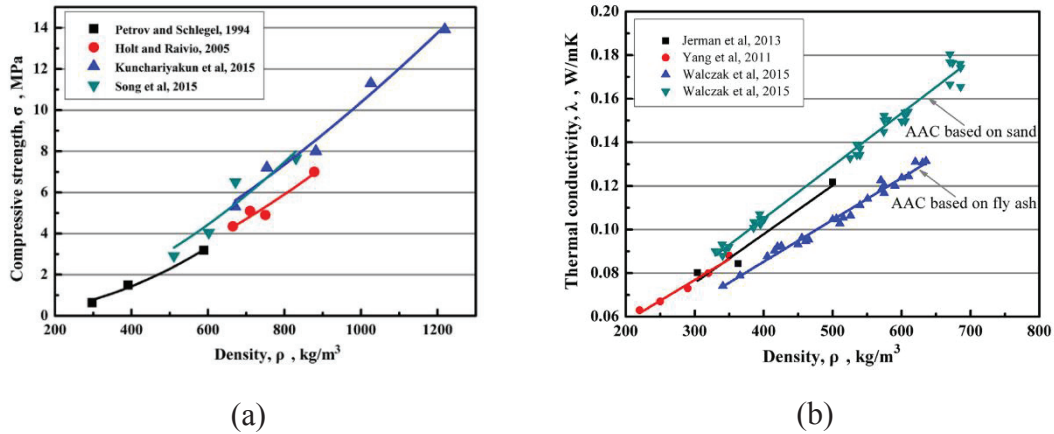
Figure 2.7. The variation of (a) compressive strength and (b) thermal conductivity of AAC with density [10]

The moisture has a significant effect on the mechanical properties. An increase of moisture content decreases the compressive strength, while a lower limit of 15% moisture was shown necessary for compressive and tensile strength [33]. The thermal conductivity also increases with increasing moisture content (Figure 2.8) [34].
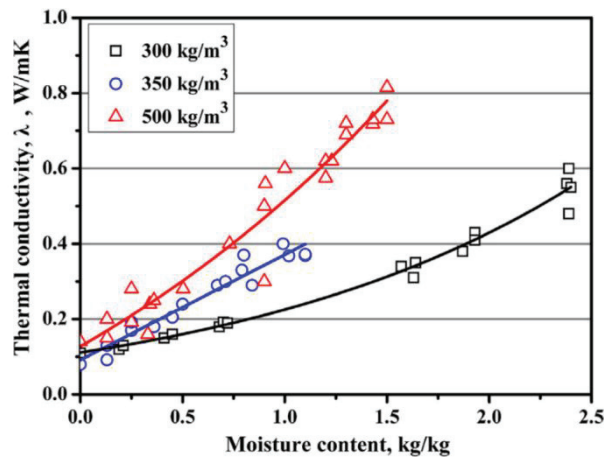
Figure 2.8. The thermal conductivity vs. moisture content [35]

The indentation response of AAC is completely different from compression. An idealized stress-strain relationship was proposed for the indentation of foam structures [36]. The stress-strain curve is composed of 3 regions: a linear elastic regime at low strains, a yielding or collapse region in which the structure crushed under indenter and a strain hardening region in which the deformed material is completely compacted [36]. The

indentation strength was calculated by dividing the applied load to the projected area [37]. The crushed and compacted region under indenter acted as a rigid material that delivered the stress to surrounding [38].

2.3. Dynamic Mechanical Properties of AAC

The response of an AAC sample (500 kg m^{-3}) to explosion was experimentally investigated using a micro-charger (2 mm in diameter rand 25 mm in length) containing 10 mg of pentaerythritol tetranitrate (PETN) as shown in Figure 2.9(a) [39]. The micro-charger produced a stress pulse with a duration of 13 µs, peak pressure of 8 bar and shock velocity of 670 m s^{-1}. Holes drilled in 2 mm size through thickness of AAC sample (25 mm) were used to place the explosion charge. Radial cracks emerging from the boreholes and spalling cracks were observed (Figure 2.9(b)). It was shown that the source-edge distance had a major effect in determining the number of cracks formed in the explosion test.

(a)   (b)
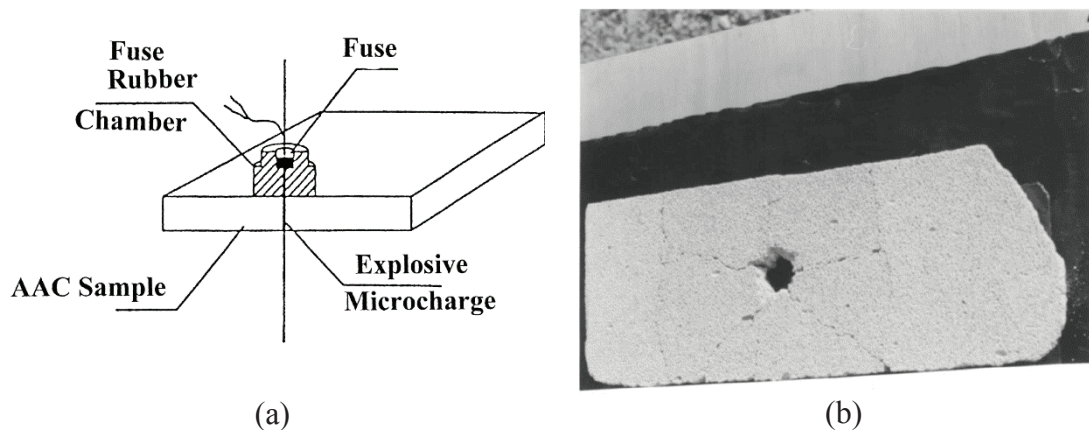
Figure 2.9. (a) schematic of the pulse source and test and (b) radial and spalling cracks [39]

The indentation behavior of AAC (500-1200 kg m^{-3})/Carbon Fiber Reinforced Polymer (CFRP) (HEX 103) composite sandwich structure against low velocity impact (hemispherical impactor 19.5 mm in diameter) was experimentally determined [26]. Opposite to the soft core sandwiches which exhibited face buckling and localized core

crushing at low velocity impact, AAC core exhibited local crushing and progressive conical failure (Figure 2.10). The conical form of progressive failure distributed the load to a wider area at the backing plate, showing energy absorbing capabilities of AAC when used as core in sandwiches.
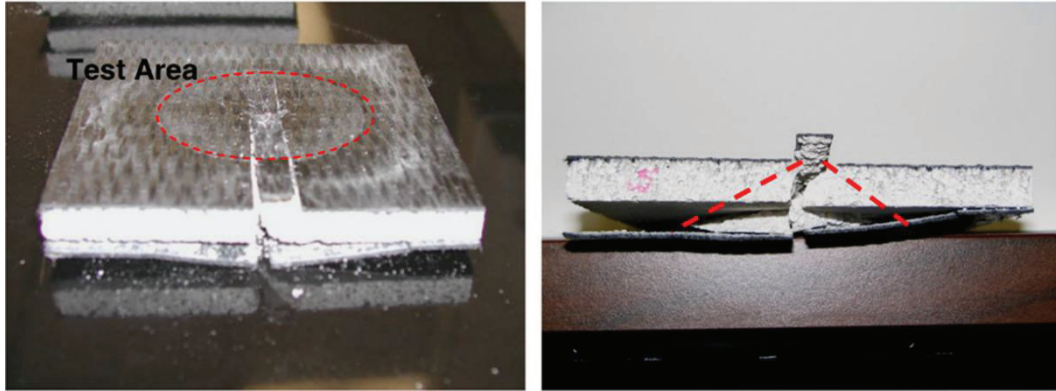
Figure 2.10. Failure of AAC/FRP sandwich panel after testing with hemispherical impactor and the conical failure from impact location to back face [26]

The quasi-static and dynamic compression behavior of an AAC sample (550 kg m^{-3}) were determined until about 10^4 s^{-1} through unconfined and confined tests [40]. The confined tests were performed by inserting 20 mm-diameter sample inside a rigid steel cylinder. The tested samples were completely densified and a continuous load-displacement behavior was reported (Figure 2.11). The compressive strength increased with increasing strain rate, while damage formed earlier in dynamically tested samples. The compressive strength increased 45% of the quasi-static strain rate (3×10^{-3} s^{-1}; 4 MPa) at a strain rate of 515 s^{-1}. The confined test compressive strength (5 MPa) at quasi-static strain rate was also higher than that of unconfined test. But, no high strain rate test on the confined samples was performed in this study.

The blast response of a cellular concrete was investigated using a shock-tube with an instrumented short rod to measure the transmitted stress (Figure 2.12) [3]. It was shown that there existed a critical length for the densification of AAC sample tested. If the sample length was less than the critical length, transmitted stress amplitude was enhanced, if not, the transmitted stress was higher than the applied blast pressure amplitude and the compaction resulted in densification of AAC sample.
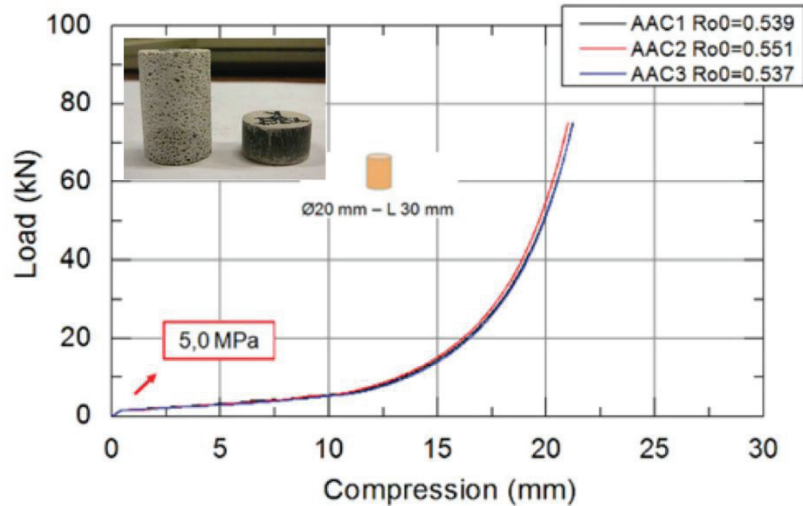
Figure 2.11. Load-displacement curve of confined test and the picture of the sample before and after the test [40]

2.4. Motivation for Thesis

The literature survey given above has clearly indicated that there have been few reports on the strain rate dependent compressive strength of AAC. On the other side, there have been numerous experimental and numerical studies on the strain rate dependent crushing strength of concrete. An excellent review on the compression behavior of concrete at high strain rates have also been recently published [41]. The effect of strain rate on the compressive strength of concrete is generally reported by a dynamic increase factor, the dynamic/static fracture strength ratio (DIF). The DIF of concrete varies between 1 and 2.5, from static and to dynamic strain rates, with a sudden rise after about 100 s^{-1} (Figures 2.13(a-b)). The variations between the tested samples' DIF values were also reported and attributed to the variations in the extent of the radial and axial inertia between the test samples [14,42]. The reported data on the compressive strength of concrete included both the forces that are due to axial and radial inertia.

In present thesis, various experimental quasi-static and dynamic tests including compression, indentation, Brazilian, direct impact and confined compression tests were performed on a cellular concrete (600 kg m^{-3}) in order to investigate the strain rate sensitive crushing strength of such brittle cellular materials. For that, indentation and

13

confined compression tests were performed, in addition to unconfined compression tests, at different strain rate regimes. The tests were further implemented numerically in LS-DYNA using a strain rate insensitive material model, MAT_096 (MAT BRITTLE DAMAGE). Modelling efforts allowed to identify the effect of both radial and axial inertia effects on the crushing of AAC by excluding strain rate effect.
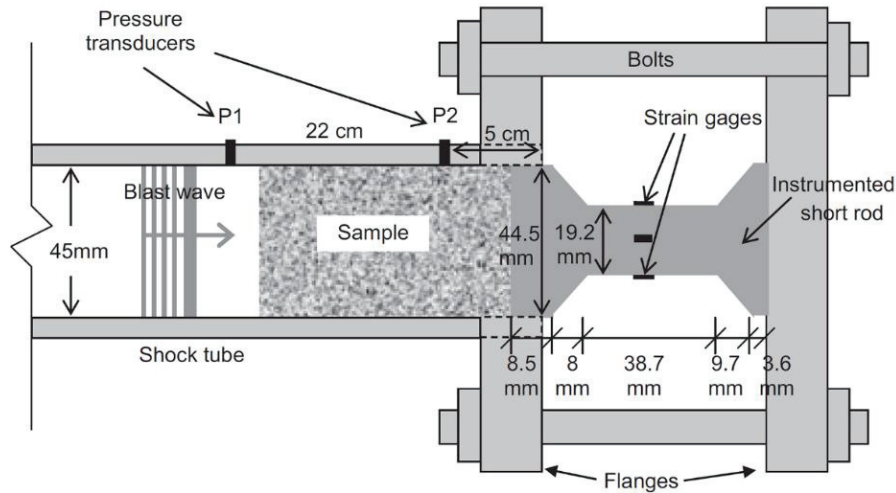
Figure 2.12. The schematic of instrumented test system to measure blast response of AAC [3]

(a)
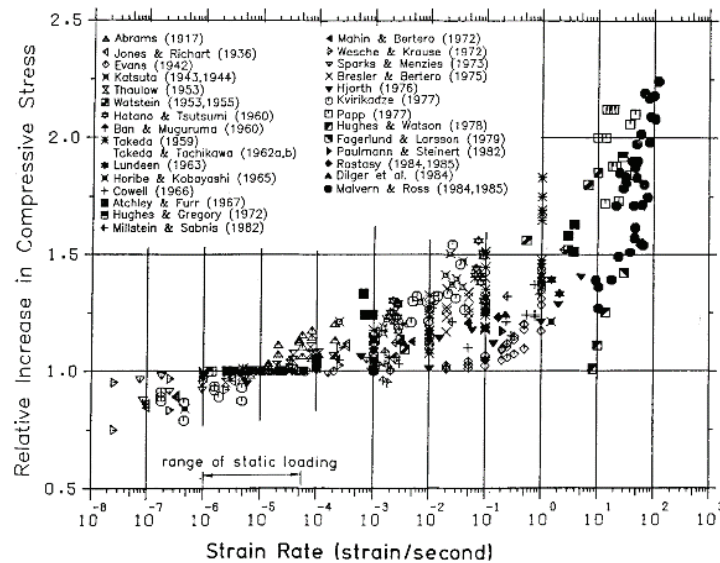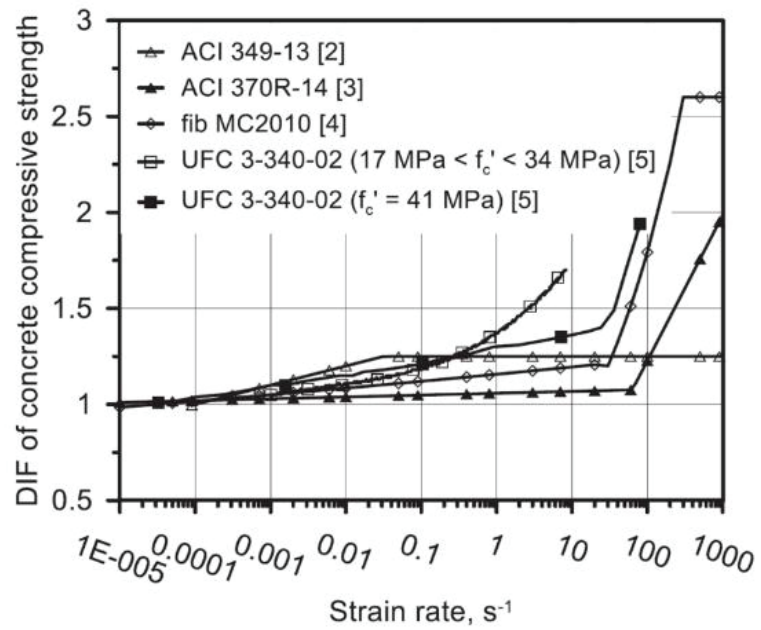
(b)

Figure 2.13. DIFs of the concrete compressive strength from (a) reference [14] and (b) reference [42]

CHAPTER 3

EXPERIMENTAL

3.1. Materials

Two AAC samples with densities of 180 and 600 kg m^{-3} and sequentially coded as Minepor (MP) and G406 were provided by AKG Gaz Beton. Both samples were received in blocks, 30 cm in size, as shown in Figures 3.1(a-b). The cellular structures of MP and G406 sample are seen in Figures 3.2(a-b). MP has larger cell size and higher porosity and is mainly used as thermal insulator. It has a thermal conductivity of 0.05 W m^{-1} K^{-1}, reported by the producer. The sample with higher density, G406, has smaller cell size and lower porosity and is used as thermal insulator and also building material in interior and exterior walls. It has a thermal conductivity of 0.19 W m^{-1} K^{-1}, reported by the producer. Both MP and G406 have A1 flammability class.

| (a) | (b) |

Figure 3.1. The pictures of as-received (a) MP and (b) G406 blocks

(a)　　　　　　　　　　　　　　　　　(b)
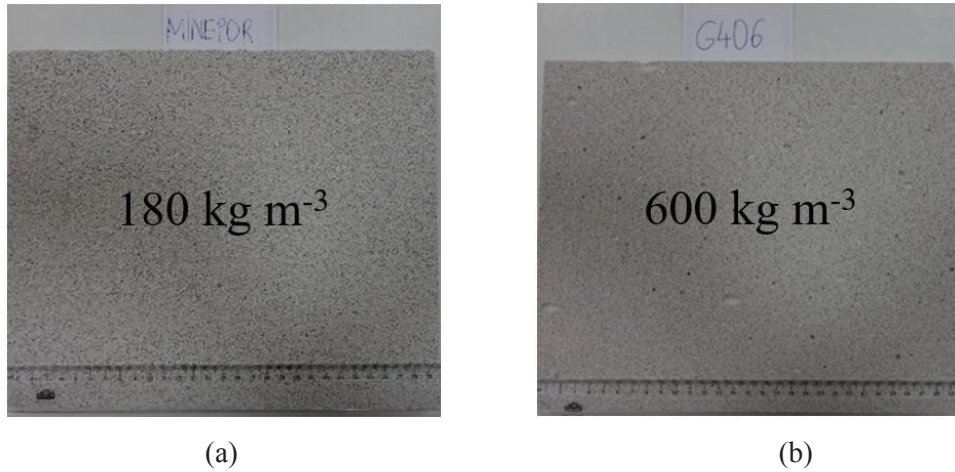
Figure 3.2. The cell structure of AAC samples (a) MP and (b) G406

3.2. Sample Preparation

The compression test samples, 19.7 mm in diameter and 26 mm in length, were core-drilled from 26 mm-thick AAC plates. The indentation tests were performed on 40x40x20 cm AAC blocks. AAC blocks were kept in vacuum bags until they were core-drilled or cut for the indentation tests (Figure 3.3). Before the mechanical tests, the core-drilled samples for compression tests and the blocks for indentation tests were kept in an oven at 70°C for 24 h (Figure 3.4).

Figure 3.3. The picture of an AAC block kept in a vacuum bag

The static and dynamic compression test samples were extracted by using a core drilling machine shown in Figure 3.5(a). The core-drilling was performed using a core-

drill bit having an inner diameter of 19.7 mm. Figure 3.5(b) shows the picture of a 26-mm thick core-drilled MP sample. Since no-coolant was used during core-drilling, the surface of cylindrical compression test samples was covered with powder. The powder on the surfaces was removed by applying pressurized air. The picture of core-drilled G406 compression test samples is shown in Figures 3.6.
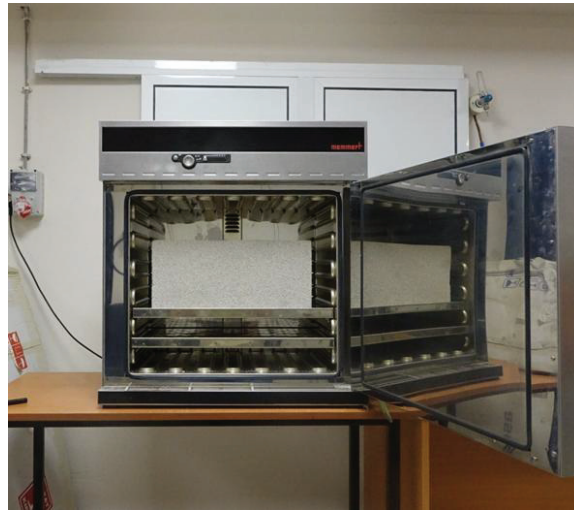
Figure 3.4. The picture of an AAC block inside the ventilated oven
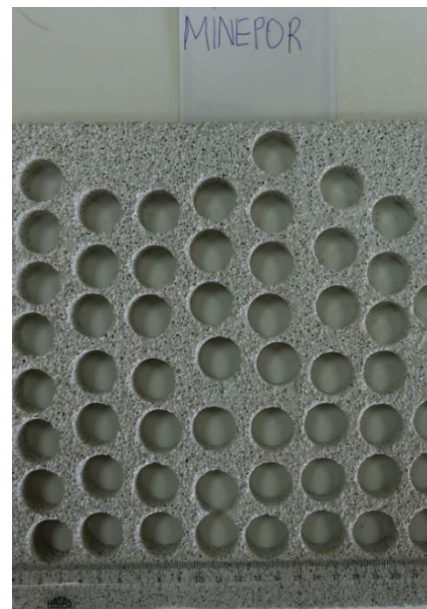
| (a) | (b) |

Figure 3. 5. The pictures of (a) core-drill machine jointed with drill apparatus and
(b) a drilled 26 mm thick MP plate

Figure 3.6. The picture of core-drilled G406 samples after cleaning with pressurized air

3.3. Quasi-static Compression Tests

Quasi-static compression, confined compression, indentation and Brazilian tests were performed using a Shimadzu AG-X Universal Test Machine in the Dynamic Testing and Modelling Laboratory of Izmir Institute of Technology (Figure 3.7). Three different cross-head speeds were selected for the quasi-static tests: $5x10^{-5}$, $5x10^{-4}$, and $5x10^{-3}$ m s^{-1}. In the quasi-static tests, the strain rate ($\dot{\varepsilon}$) was determined

$$\dot{\varepsilon} = \frac{L_s}{v_{cr}}$$

(3.1)

where v_{cr} is the cross-head speed and L_s is the length of specimen. The strain rates corresponding to cross-head velocities of $5x10^{-5}$, $5x10^{-4}$, and $5x10^{-3}$ m s^{-1} were 0.002, 0.02 and 0.2 s^{-1}, respectively. The nominal stress (σ) and strain (ε) were calculated using the following relations

$$\sigma = \frac{P}{A_s}$$

(3.2)

and

$$\varepsilon = \frac{\delta}{L_s}$$

<div align="right">(3.3)</div>

where P, δ and A_s and are the applied load, displacement and the initial area of sample, respectively.

The quasi-static compression tests were performed in accord with ASTM C39/C 39M – 03 "Standard Test Method for Compressive Strength of Cylindrical Concrete Specimens" [30]. The strain was calculated by using the test machine stroke and video extensometer displacement records. An axis-aligned pin-ball upper compression platen was used in the compression tests (Figure 3.8) in order to load the specimen axially. The sample deformation was recorded with a video camera. Total 10 tests were conducted at each quasi-static velocity.

Figure 3.7. Shimadzu AG-X Universal Test Machine

Figure 3.8. Axially aligned pin-ball compression upper platen

3.4. Quasi-static Indentation Tests

The quasi-static indentation tests were conducted on 40x40x20cm blocks. The indentation tests were performed using hemispherical 5, 10, 15, 20, 25 and 30 mm diameter indenters (Figure 3.9). The indenters were machined from 304 steel, then heat-treated to a hardness of 30 in Rockwell scale. The indenters in 5, 10, 15, 25 and 30 mm size were screwed to the Shimadzu Universal Testing Machine at the treated end, while 20 mm indenter was compressed by upper compression platen on the blocks. The pictures of indented AAC blocks are shown in Figure 3.10. In the same figure the pre-determined indentation locations are also seen. In the indentation tests, the load and displacement were recorded and the tests were continued until 25 mm displacement.

Figure 3.9. 5, 10, 15, 20, 25 and 30 mm diameter indenters
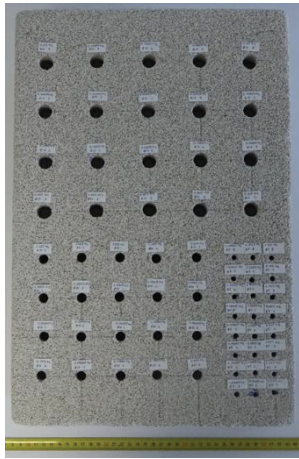
Figure 3.10. The pictures of tested AAC blocks with (a) 5, 10, 15 mm indenters and (b) 25 mm and 30 mm indenter

3.5. Low Velocity Compression Tests

The low velocity compression tests were performed in a FRACTOVIS drop weight tower (Figure 3.11(a)). The test set-up consisted of striker holder, striker and 90 mm diameter cylindrical compression impactor as shown in Figure 3.11(b). The cylindrical compression platen was attached to the tip of a 90 kN striker. In order to control the impact energy, the weights were added or removed. A photocell device, placed in the path of the striker, allowed to measure the velocity of the impactor. The point of initial contact with the specimen and the striker initiated the test and the impactor travelled through the specimen. The load-displacement, force-time and energy-time curves were recorded by a Data Acquisition System. The sampling frequency was 1000 kHz with a 20 ms of test duration. A total weight of 6.42 kg was used in the tests. The initial impact velocity was 1.05 m s^{-1}, corresponding to an initial strain rate of 40.38 s^{-1}. The failure of the specimen was recorded by a Fastcam Photron high speed camera at 20000 fps (Figure 3.12).

(a)
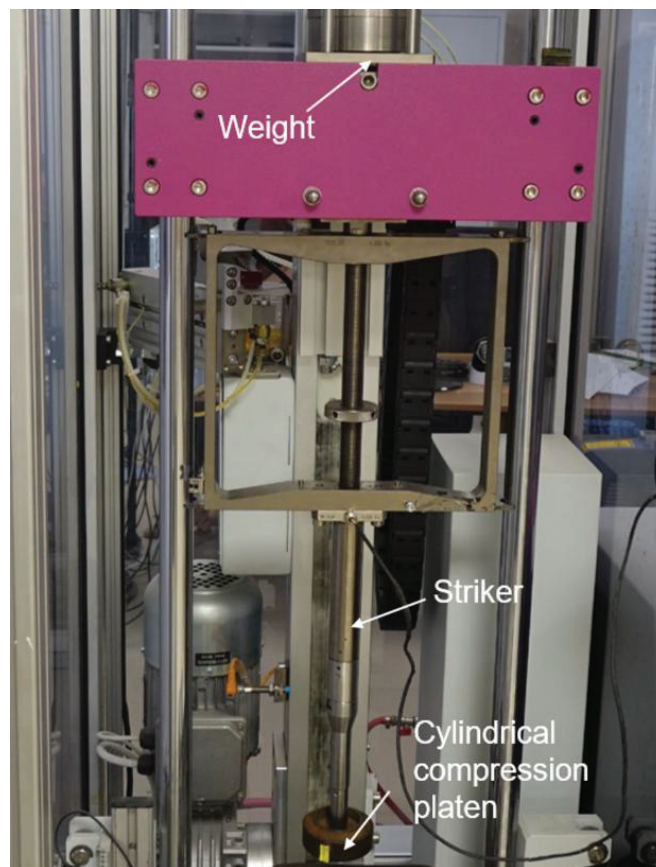
(b)

Figure 3.11. (a) FRACTOVIS low velocity impact test equipment and (b) striker

holder, weights and the impactor

Figure 3.12. The picture of Fastcam Photron high speed camera

3.6. High Strain Rate Compression Tests

High strain rate compression tests were conducted using a strain-gaged compression Split Hopkinson Pressure Bar (SHPB) apparatus (Figure 3.13). The SHPB test setup consisted of a gas gun, striker, incident and transmitter bars and a data acquisition system (Figure 3.14(a)). The test starts with filling the gas gun with nitrogen at a specific pressure. The release of gas fires the striker bar onto the incident bar at a specific velocity. The impact of the striker bar creates a compressive wave on the incident bar. The incident wave is partly reflected as tensile wave at the specimen bar interfaces to the incident bar and partly transmitted as compressive wave to the transmitter bar (Figure 3.14(b)). The incident, reflected and transmitted waves are measured from the strain gages mounted on the incident and transmitter bar.

Figure 3.13. The SHPB test set-up
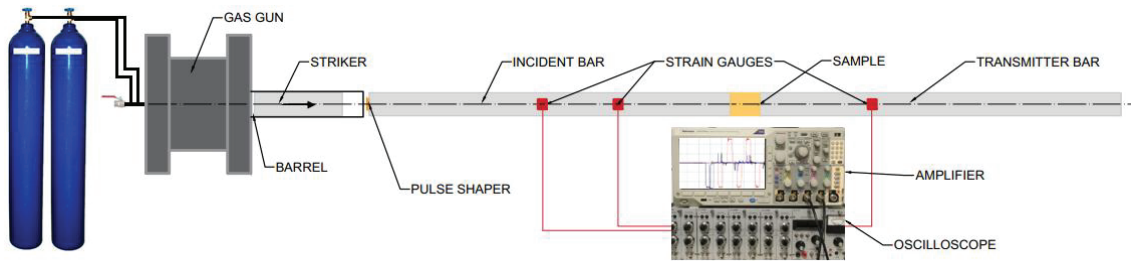
(a)
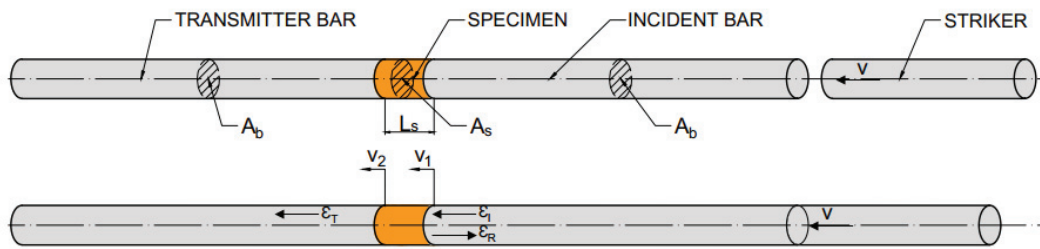
(b)

Figure 3.14. (a) the schematic of SHPB set-up and (b) the waves

The velocity of the striker bar depends on the pressure of the gas gun. Higher the gas gun pressures, higher is the velocity of the striker bar. The wave length of the

incident stress depends on the length of the striker bar; longer is the striker bar, longer the wavelength and duration of incident wave [43]. The time window of the incident stress (T) is

$$T = \frac{2L_{sb}}{C_{sb}}$$

(3.4)

where, L_{sb} and C_{sb} are the length and the elastic wave speed of the striker bar, respectively. The stress (σ_i) and strain (ε_i) developed on the incident bar are sequentially

$$\sigma_i = \frac{1}{2}\rho_b C_b v_{sb}$$

(3.5)

and

$$\varepsilon_i = \frac{1}{2}\frac{v_{sb}}{C_b}$$

(3.6)

where, v_{sb}, ρ_b and C_b are the velocity of the striker bar and the density and elastic bar wave speed of the bar.

The used SHPB consisted of 19.40 mm diameter Inconel 718 incident and transmitter bar. The incident and transmitter bar were 3450 and 2050 mm long, respectively. The elastic modulus and density of the bar material were 204 GPa and 7810 kg m^{-3}, respectively. The stress waves on the bars were measured by 350 Ω foil strain gages in a full Wheatstone-bridge configuration. The bridge voltage was recorded with an oscilloscope and strain gage amplifier (Figure 3.15). The deformation of the specimen was captured by a Fastcam Photron high speed camera at 20000 fps (Figure 3.12). The velocity of the striker bar was measured using laser-velocity gates mounted at the exit of the gas barrel. The velocity of the striker bar was also determined form the high-speed camera records of the striker bar.

The stress and strain analysis of the SHPB are based on the assumption of the stress equilibrium between incident bar-specimen and transmitter bar-specimen interfaces as

$$\varepsilon_I(t) + \varepsilon_R(t) = \varepsilon_T(t)$$

(3.7)

where ε_I, ε_R and ε_T are the incident, reflected and transmitted strain, respectively.

Figure 3.15. The picture of oscilloscope and amplifier

Based on stress equilibrium the strain (ε_s), stress (σ_s) and strain rate ($\dot{\varepsilon}_s$) of the specimen are formulated as,

$$\varepsilon_s(t) = -\frac{2C_b}{L_s} \int_0^t \varepsilon_R(t)dt$$

(3.8)

$$\sigma_s(t) = \frac{A_b}{A_s} E_b \varepsilon_T(t)$$

(3.9)

$$\dot{\varepsilon}_s(t) = -\frac{2C_b}{L_s}\varepsilon_R(t)$$

<div align="right">(3.10)</div>

where L_s, A_b, A_s and E_b is the initial length of the sample, the cross-sectional area of the bar and specimen and elastic modulus of the bar.

In the SHPB test of brittle materials, the sample fractures at an earlier time before the establishment of stress equilibrium. The stress equilibrium is established after 3-4 wave reflections in the sample [44]. Therefore, the fracture time should be higher than 3 times of the transit time of the sample (sample length/sample elastic wave velocity). Pulse shaping technique is usually used to obtain a more gradually rising incident wave. In this technique, a complaint material is placed to the end of the incident bar, so that striker bar impinges the complaint material rather than the end of the incident bar. In present study, an aluminum sheet in 10x10x2 mm size was used as pulse shaper.

3.7. Direct Impact Tests

In the direct impact test, the test specimen is placed to the front of incident bar and a striker bar with an initial velocity (v) impinges the specimen directly. The schematic of SHPB direct impact test is shown in Figure 3.16(a). The test specimen is attached to the incident bar by applying a thin layer of lubricant which holds the specimen in place during the striker bar impact. Considering Figure 3.16(b), the strain on the specimen is

$$\varepsilon_s(t) = \frac{u_2(t) - u_1(t)}{L_s}$$

<div align="right">(3.11)</div>

where u_1 and u_2 are the displacement of the incident and striker bar, respectively. The displacements of the incident and the striker bar are

$$u_1(t) = c_b \int_0^t \varepsilon_1 dt$$

<div align="right">(3.12)</div>

$$u_2(t) = vt - c_b \int_0^t \varepsilon_2 dt$$

<div align="right">(3.13)</div>

where ε_1 and ε_2 are the strain on the incident and striker bar, respectively. Considering the stress equilibrium, the specimen strain is

$$\varepsilon_s(t) = \frac{vt - 2c \int_0^t \varepsilon_1 dt}{L_s}$$

<div align="right">(3.14)</div>

Therefore, the stress of the specimen becomes

$$\sigma_s(t) = \frac{A_b E_b \varepsilon_t}{A_s}$$

<div align="right">(3.15)</div>

(a)

(b)
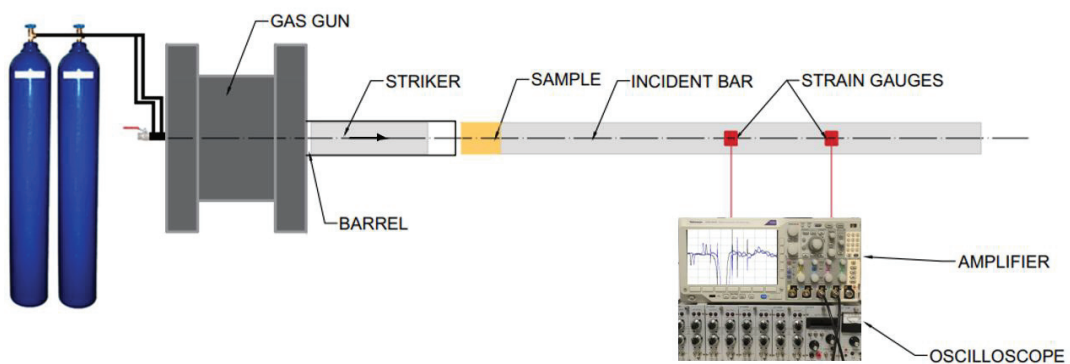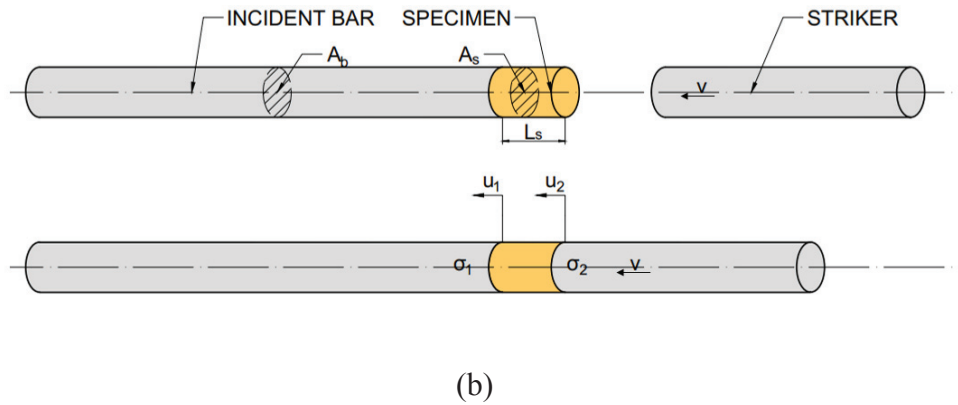
Figure 3.16. The schematic of SHPB direct impact test (a) set-up and (b) scheme

3.8. Quasi-static and High Strain Rate Confined Compression Tests

A steel confinement tube was used to perform the constrained uniaxial compression tests at quasi-static and high strain rates. The inner diameter of the steel tube was 19.7 mm, the same with the compression test sample. The quasi-static tests were performed at 5×10^{-4} m s^{-1} and the dynamic test at 8 m s^{-1}. Total 10 confined compression tests were performed at both velocities. Before the tests, the samples were inserted inside the steel tube with applying a pressure as shown in Figure 3.17.

The schematics of the confined compression tests at static and dynamic velocities are shown in Figures 3.18(a-b), respectively. In the quasi-static confined compression test, the sample was compressed by a 100 mm-length Inconel bar which was just located under the loading plate. In dynamic confinement test, the AAC sample was placed between the flat-ends of the incident and transmitted bar in the steel tube. Since the strength of the steel tube is much higher than that of AAC, the steel tube is assumed rigid. The confinement prevented the lateral expansion and allowed the specimen to deform until full densification.
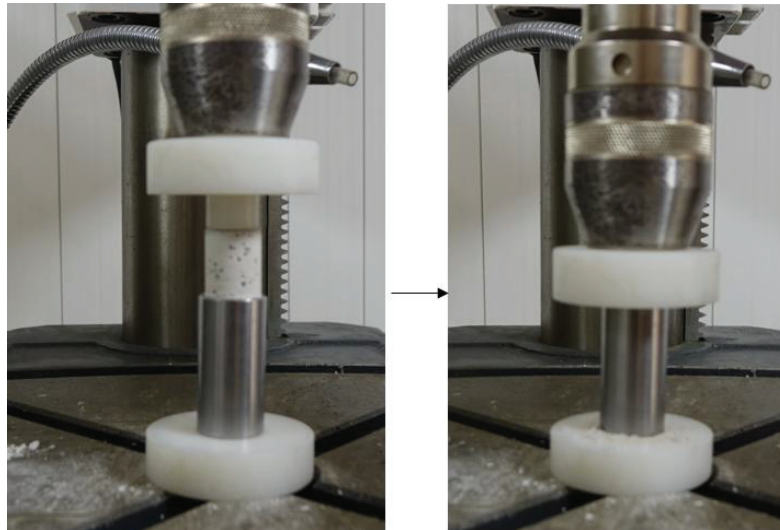
Figure 3.17. Inserting scheme of the AAC to steel tube

(a)

(b)
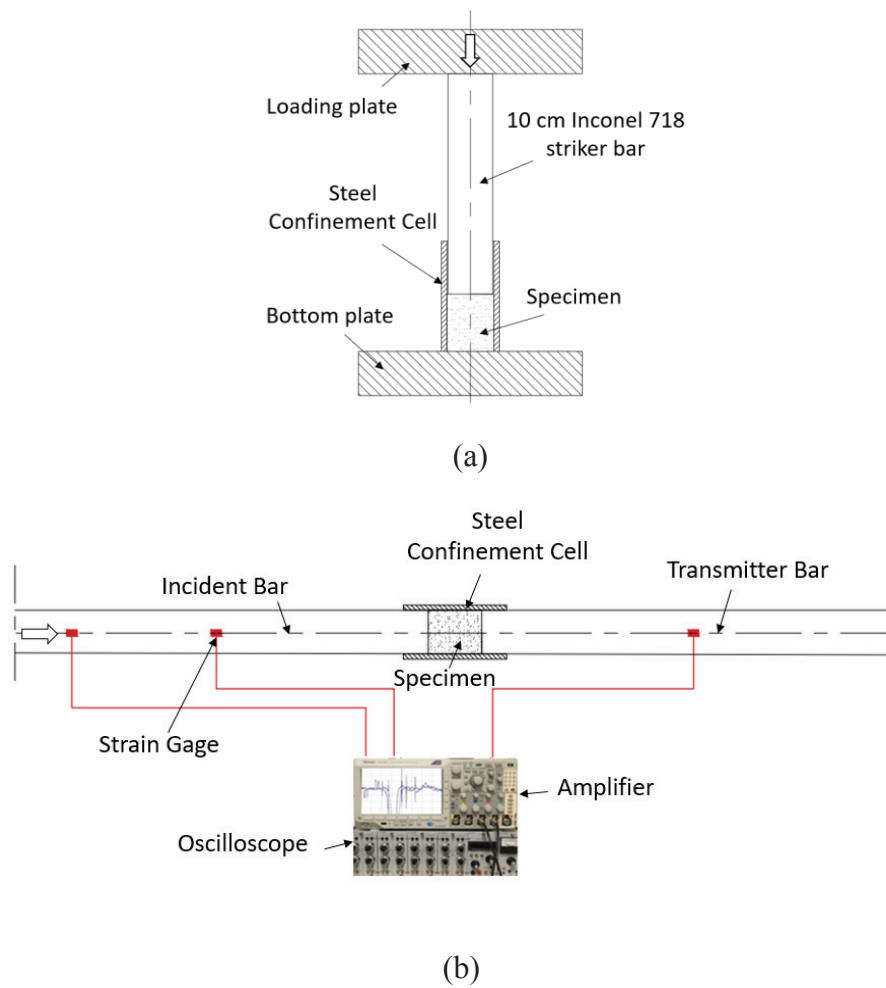
Figure 3.18. (a) Quasi-static and (b) dynamic confined compression tests

3.9. Brazilian Tests

The tensile behavior of AAC sample was determined by the Brazilian test. The method is also called indirect tensile test. The cylindrical compression test sample, 20 mm diameter and 26 mm length, were used at both quasi-static and dynamic strain rate tests. The Brazilian tests at quasi-static and dynamic strain rates were conducted using Shimadzu AG-X Universal Test Machine and SHPB, respectively. The schematic of the quasi-static and dynamic indirect tensile tests are shown in Figures 3.19(a-b), respectively.

(a)

(b)
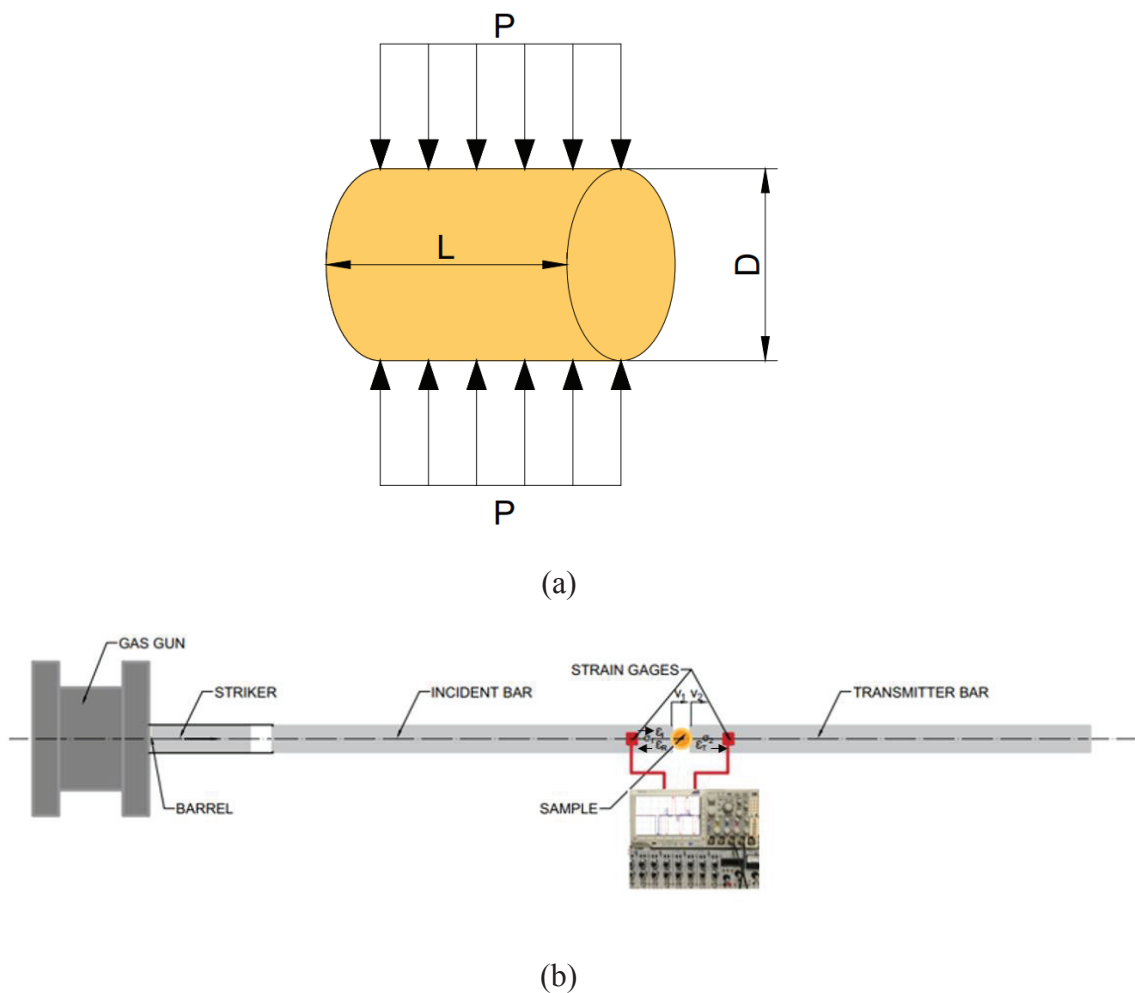
Figure 3.19. Schematic of the Brazilian (a) quasi-static and (b) dynamic test

The splitting tensile theory formulates the tensile strength (σ_t) indirectly as

$$\sigma_t(t) = \frac{2P}{\pi DL}$$

(3.16)

where P, D and L are sequentially the load and the diameter and thickness of the specimen. The crack propagation occurs along two-dimensional surface and has a certain relationship between the stress and crack area of the specimen [45]. The dynamic indirect tensile stress in the SHPB test was formulated as

$$\sigma_t(t) = \frac{Ed^2}{2LD}\big(\varepsilon_t(t)\big)$$

(3.17)

The lateral inertia confinement and it influences the dynamic tensile strength directly [46]. The fracture mechanics of the cylindrical AAC samples indicate the Griffith failure strength which groves in tensile strength and it may be observed effectively while the SHPB impact has been performed [45, 47].

3.10. Fracture

The deformation of AAC samples in quasi-static and SHPB bar compression tests were recorded using a Sony RX10 and Fastcam Photron high speed camera, respectively. The powder accumulation in the front of indenter in the indentation tests was analyzed after cutting the tested blocks. The fracture strength was fitted with the Weibull distribution. The Weibull survival probability, $P(V)_s$ is

$$P(V)_s = \exp\left[-\left(\frac{\sigma}{\sigma_o}\right)^m\right]$$

(3.18)

where m is the Weibull modulus, σ is the stress and σ_o is the characteristic strength [48]. The Weibull modulus represents how rapidly the strength falls as the stress approaches σ_o. When $\sigma = 0$, $P(V)_s = 1$, $\sigma = \sigma_o$ and $P(V)_s = 0.37$. In general, the m parameter varies between 1 and 15 for brittle materials [49]. In indentation tests, the fracture strength of the tested samples was analyzed with average values.

3.11. Numerical Modelling

The compression tests at quasi-static and high strain rates were simulated in the non-linear explicit finite element code of LS-DYNA. The cylindrical AAC samples were simulated using MAT_096 material model. The models of plates, bars and samples were drawn in CATIA V5 and saved as .IGS file and then transferred into the HyperMesh meshing software. The parts of the test set-up and sample were meshed with quad elements. The meshed structures were exported as a .k file to the LS-PrePost software. In the LS-PrePost, the material properties, contacts and boundary conditions were defined. The LS-PrePost file was solved by LS-DYNA SOLVER.

Figures 3.20 (a-b) represent the front and 3D view of the numerical model of the quasi-static compression test set-up, respectively. The model was composed of the top and bottom compression test platen and sample. Each compression platen had 19200 constant stress solid elements. Both the top and bottom compression platens were modelled using 6 mm-long and 2 mm–wide elements. The steel platens were modeled with MAT020_RIGID material model (E=210 GPa and v=0.3). The rotations and the movement of the compression steel platens were restricted in the x and y-direction, except the axial motion of the top platen in the z-direction. The axial velocity of the top platen in z-direction was kept constant by PRESCRIBED_MOTION_RIGID card (5×10^{-3} m s^{-1}) the same as the experiments. The termination time of the model was determined by the experimental test result. The contact between compression test platens and specimen were defined by AUTOMATIC_SURFACE_TO_SURFACE contact. Besides, ERODING_SINGLE_ SURFACE was used to erode the failed particles during the simulation. The mass scaling was implemented in the quasi-static simulation by CONTROL_TIMESTEP card. Mass scaling enabled the addition of mass to just a few small elements in the quasi-static model as the kinetic energy was lower

than the peak internal energy. The time step of the elements was the same since the mass control was achieved by adding or removing elements. To obtain the mass scaling factor, the model was simulated initially without mass scaling and the determined time step was multiplied by 1000 as the kinetic energy was smaller than the internal energy when the mass scaling factor was selected as 1000.

The SHPB test model and specimen-bar interfaces are shown in Figures 3.21(a-b), respectively. The striker velocities in the SHPB model were 1 and 8 m s^{-1}, the same as the experimental velocities. The length of striker, incident and transmitter bar was 500 mm, 3110 mm and 2050 mm, respectively and all were made of Inconel 718. The striker, incident and transmitter bars were modelled with 15 mm-size elements. The striker, incident and transmitter bar were modelled using 7000, 28980 and 19180 constant stress solid elements, respectively.
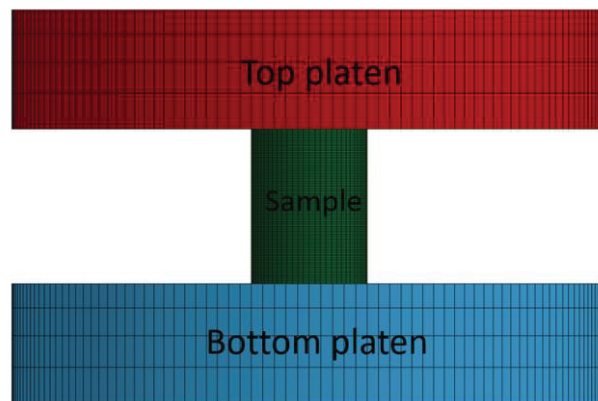
(a)
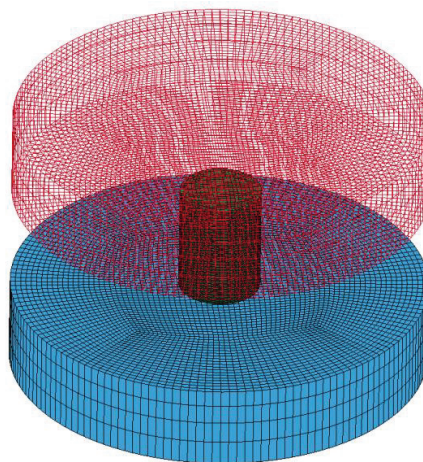
(b)

Figure 3.20. Quasi-static model (a) test and (b) specimen-platen interfaces

The numerical model of the SHPB direct impact test and specimen-bar interfaces are shown in Figures 3.22(a-b), respectively. The Inconel 718 incident bar (3110 mm long) was modeled using 15 mm size elements and 200 mm-long aluminum striker bar was modeled using 5 mm size elements. The 200 mm-long aluminum striker bar consisted of 10080 constant stress solid elements. The impact velocities in the SHPB and direct impact simulations were 1,8, 10, 20, 30, 60 and 108 m s^{-1}. The models at 1, 8, 10 and 20 m s^{-1} were implemented with Inconel 718 striker bar, while the tests at 30, 60 and 108 m s^{-1} with Aluminum striker bar.

(a)

(b)
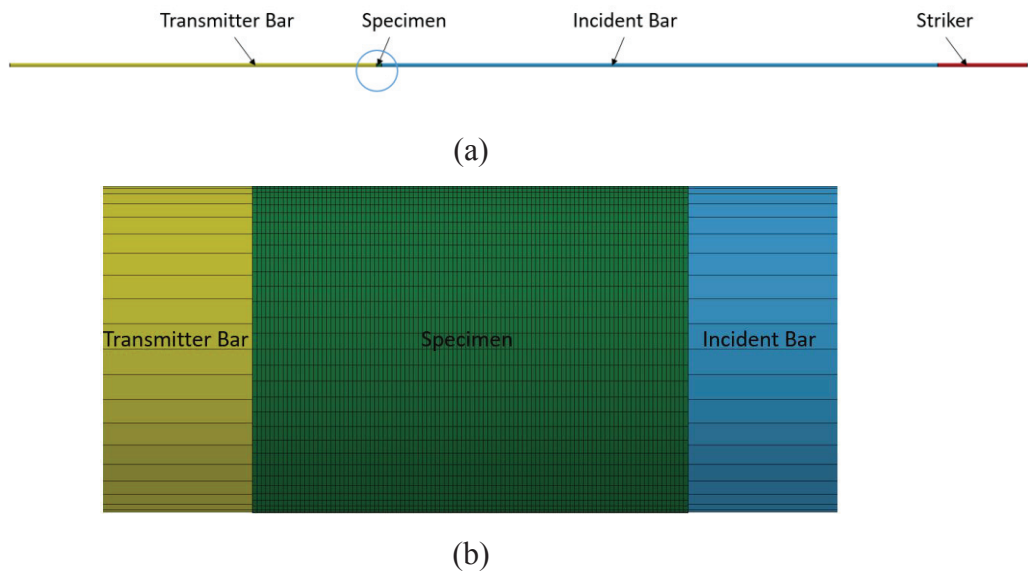
Figure 3.21. (a) SHPB test model and (b) specimen bar interfaces

MAT_096 material model was previously used to simulate the failure of concrete [50]. The model represented the failure of concrete for an anisotropic brittle damage which is also applicable to AAC. The Young's modulus, Poisson's ratio, the initial principal tensile strength (f_n), the initial shear traction (f_s), the fracture toughness of the material (g_c), shear retention factor (β), the viscosity of the material (η) and uniaxial compressive yield stress (σ_y) were the model parameters [51]. The material properties of AAC were determined experimentally in present study. The material model allowed to admit progressive degradation of tensile and shear strengths across smeared cracks initiated under tensile loads [52]. Besides, the compressive failure was governed a simplistic J2 flow correction [53]. The damage occurred in the simulation

was handled by treating the rank 4 elastic stiffness tensor as an evolving internal variable. The 26 mm-long and 19.50 mm-diameter AAC sample in the model consisted of 38400 constant stress solid elements.

(a)

(b)
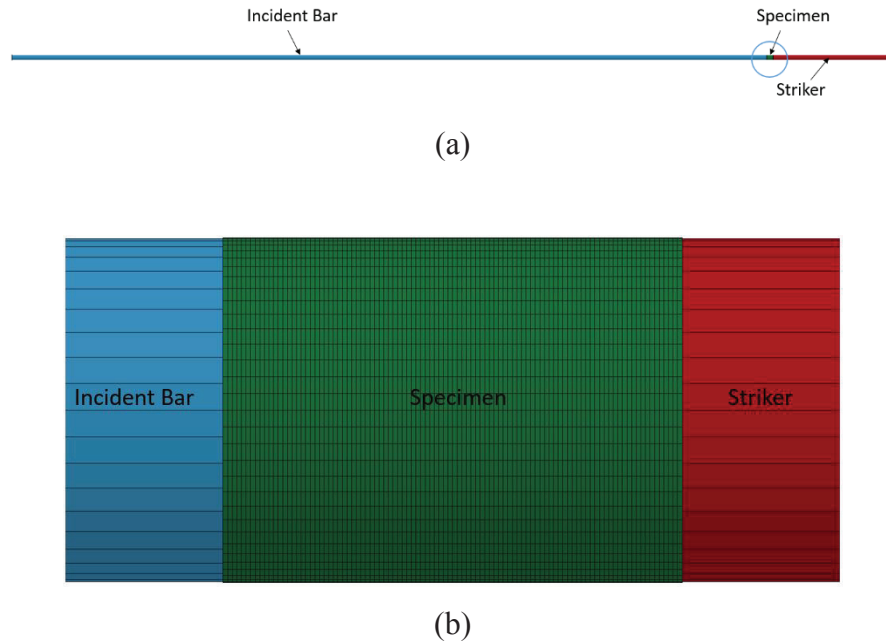
Figure 3.22. (a) SHPB direct impact test model and (b) specimen bar interfaces

The striker velocity was defined by the VELOCITY_GENERATION card in LS-DYNA. In all models, the contacts between the bars and bars/specimen was defined by AUTOMATIC_SURFACE_TO_SURFACE contact. Additionally, ERODING_SINGLE_SURFACE was applied to the AAC sample by the MAT000_ADD_EROSION parameter in both SHPB and direct impact test models.

The Inconel 718 striker, incident and transmitter bar were modelled using MAT001_ELASTIC material model with E=207 GPa, v=0.33 and ρ=7850 kg m^{-3}. The aluminum striker bar was modeled using MAT001_ELASTIC material model with E=71.7 GPa, v=0.33 and ρ=2810 kg m^{-3}. The static and dynamic friction coefficients were taken 0.2 and 0.1, respectively.

AAC sample was modelled using MAT096_BRITTLE_DAMAGE model. The parameters of the model are tabulated in Table 3.1. All material properties were determined by the quasi-static tests at 0.002 s^{-1}. The quasi-static strain rate volumetric strain of 0.0117 at fracture was used with MAT_ADD_EROSION. The volumetric strain at fracture is

$$\Delta = \varepsilon_x + \varepsilon_y + \varepsilon_z$$

<div align="right">(3.17)</div>

where ε_x, ε_y and ε_z are the strains in x, y and z-axis. In the models, the stresses were determined at the distal-end and impact-end contact area, the center and surface elements on the contact area and on the bars at the locations the same as the location of the strain gages in the tests.

Table 3.1. Material model parameters of AAC

Material	Density, ρ [kg m^{-3}]	Young's Modulus, E_B [kN mm^{-2}]	Poisson's Ratio, ν	Tensile Limit [N mm^{-2}]	Shear Limit [N mm^{-2}]	Compressive Yield Stress [N mm^{-2}]	Fracture Toughness [N m^{-1}]	Shear Retention Factor
AAC	600	0.32	0.20	1.0	2.559	5.118	3.475	0.03

CHAPTER 4

RESULTS

4.1. Experimental Results

4.1.1. Compression Tests

The compression stress-strain curves of MP samples tested at $5x10^{-5}$, $5x10^{-4}$ and $5x10^{-3}$ m s^{-1} are shown in Figures 4.1(a-c), respectively. As seen in the same figures the stress increases linearly with strain at low strains until about 0.01-0.02 strain. This region is the linear elastic region and the sample deforms elastically. The maximum stress is defined as the compressive strength. Thereafter, the stress decreases as the sample deforms by a progressive crushing starting from one of ends of the sample . Progressive crushing leads to stress fluctuations until about large strains. This region is termed as the plateau region as shown in Figure 4.1(a). Similar stress-strain behavior composing of a linear elastic and a plateau region, is seen at all quasi-static velocities (Figures 4.1(a-c)). The Weibull survival probability-compressive strength curves of the quasi-statically tested MP samples are shown in Figure 4.1(d). As noted in the same figure, characteristic compressive strength (σ_o when P_s=0.37) shown in the inset of Figure 4.1(d) is 0.305, 0.318 and 0.37 MPa for $5x10^{-5}$, $5x10^{-4}$ and $5x10^{-3}$ m s^{-1}, respectively. The characteristic compressive strength increases with increasing quasi-static velocity. The Weibull modulus (m) is 7.4, 7.3 and 5.4 for $5x10^{-5}$, $5x10^{-4}$ and $5x10^{-3}$ m s^{-1}, respectively. The compression stress-strain curves of G406 samples at $5x10^{-3}$, $5x10^{-4}$ and $5x10^{-5}$ m s^{-1} are shown in Figures 4.2(a-c), respectively. Again, the stress increases linearly with strain until about a maximum; thereafter, sharply decreases to lower values. Although the sample fails by forming a single crack, the compression test platen reloads the fractured pieces of the sample. The maximum stress corresponds to

the strains of 0.01-0.02. The Weibull survival probability-stress curves of quasi-static tests are shown in Figure 4.2(d). The characteristic stress (σ_o when P_s=0.37) shown in the inset of Figure 4.3(d) is 5.11, 5.57 and 5.93 MPa for $5x10^{-5}$, $5x10^{-4}$ and $5x10^{-3}$ m s^{-1}, respectively. The characteristic stress again increases with increasing strain rate. The Weibull modulus (m) is 21.5, 10.6 and 14.8 for $5x10^{-5}$, $5x10^{-4}$ and $5x10^{-3}$ m s^{-1}, respectively. These samples have higher m values than MP samples.
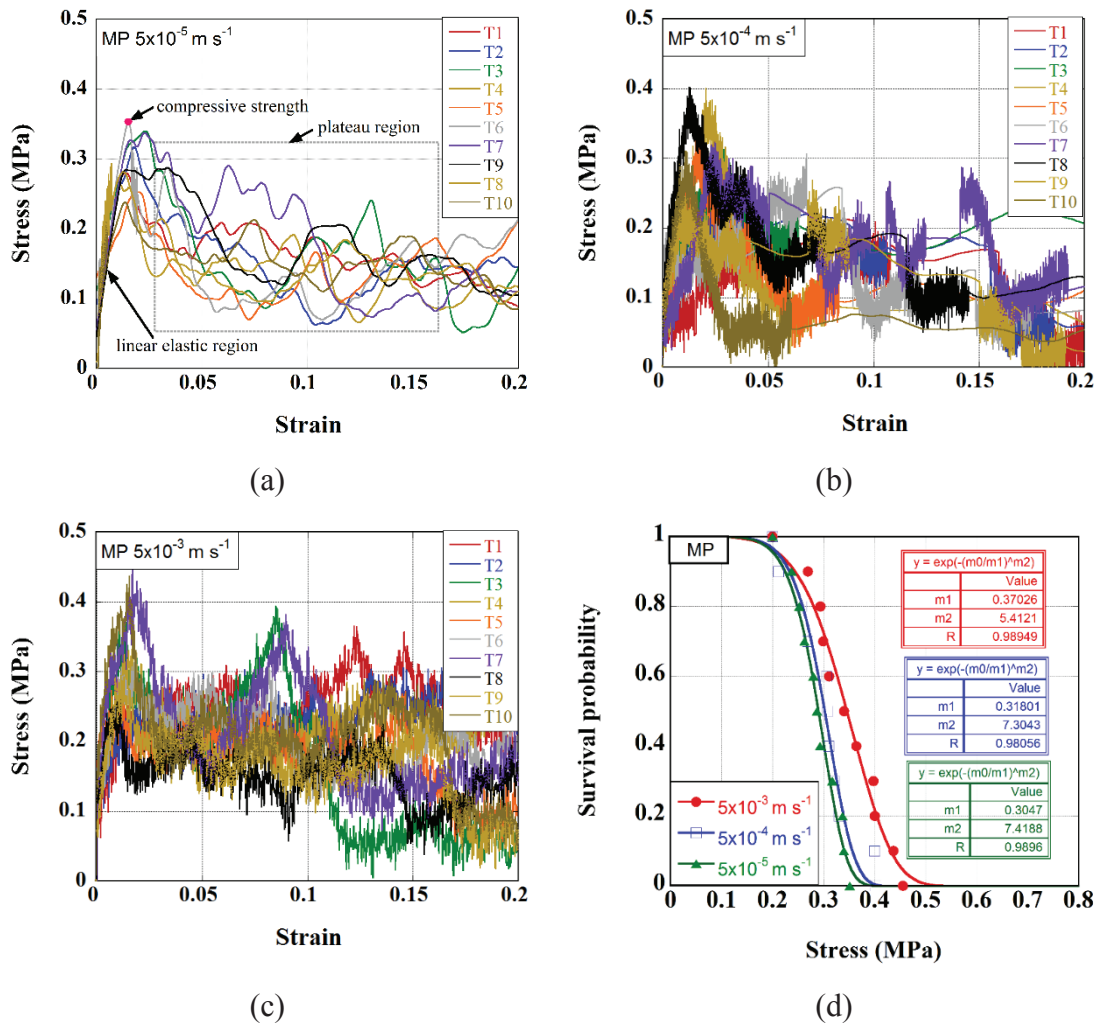
Figure 4.1. The quasi-static compression stress-strain curve of MP samples at (a) $5x10^{-5}$, (b) $5x10^{-4}$ m s^{-1} and (c) $5x10^{-3}$ m s^{-1} and (d) Weibull survival probability–compressive strength curves

(a)

(b)

(c)

(d)
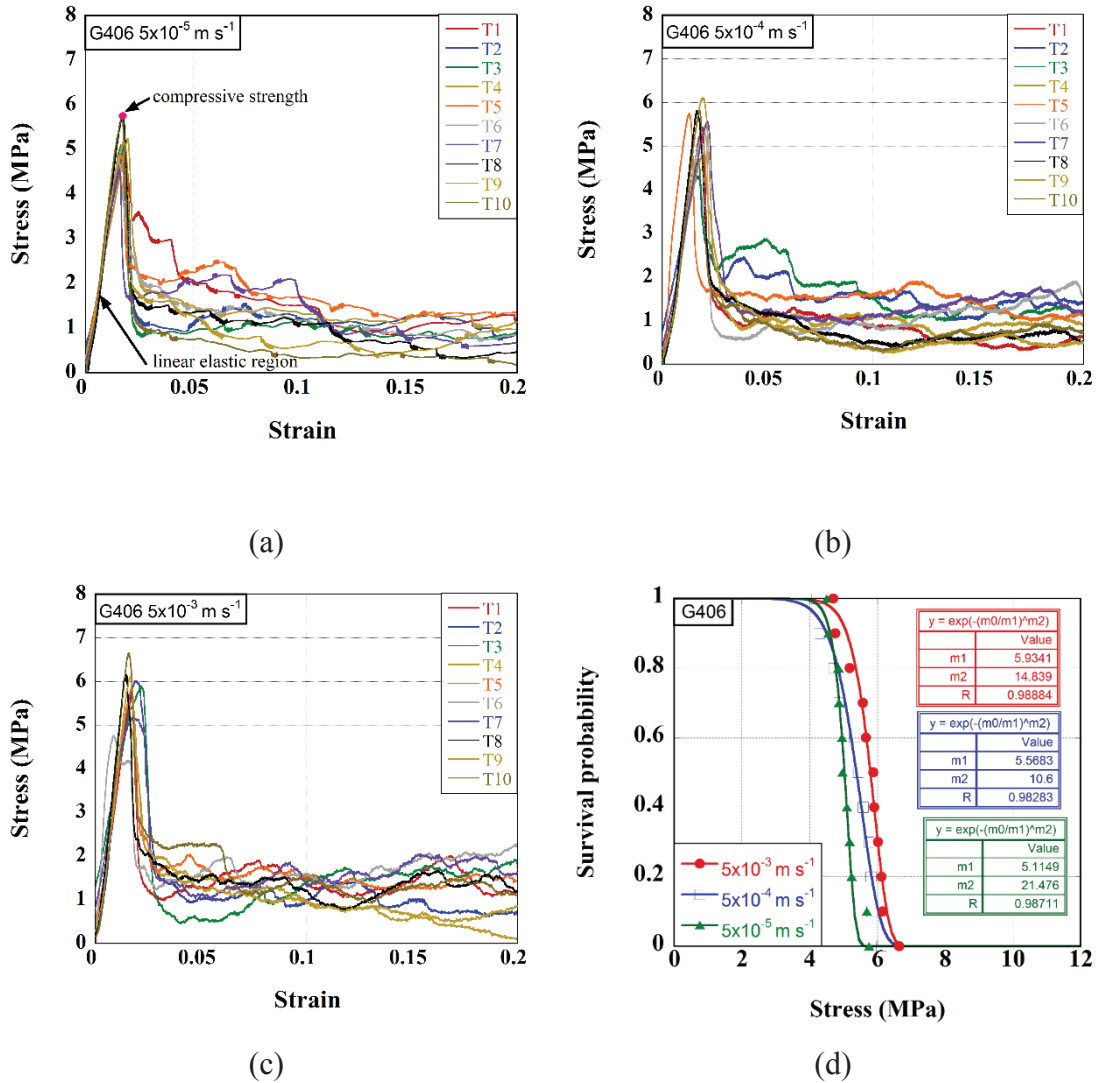
Figure 4.2. The quasi-static compression stress-strain curve of G406 sample at (a) $5x10^{-5}$, (b) $5x10^{-4}$ m s^{-1} and (c) $5x10^{-3}$ m s^{-1} and (d) Weibull survival probability–compressive strength curves

The typical stress-strain curve and the deformation pictures of MP and G406 sample $5x10^{-5}$ m s^{-1} corresponding to the strain rate of $1.92x10^{-3}$ s^{-1} is shown in Figures 4.3(a-b), respectively. Here, the main characteristics of the compression deformation of MP and G406 samples are explained in detail. The numbers on the pictures show the corresponding compression strain values. In the stress-strain curve of MP sample (Figure 4.3(a)) there are 4 distinct deformation regions as marked with the numbers in the circles. In the first region, the sample deforms linear elastically. The linear elastic region continues until about a maximum stress after cracks initiate, marked as 2 in

Figure 4.3(a). In the post compressive strength region, the sample crushes progressively starting at the lower end of the sample as shown by an arrow and a letter A in Figure 4.3(a). This region is marked as 3 and progressive sample end crushing region (plateau region). The progressive sample end crushing continues until 0.14 strain marked as B in Figure 4.3(a). With the increase of strain to 0.23, an axial crack forms (C in Figure 4.3(a)). At later stage of deformation, 0.3 strain, the sample disintegrates into several pieces. The region starting from the axial cracking is marked as 4 in Figure 4.3(a)). This deformation characteristic was also found in the samples tested at 5×10^{-4} and 5×10^{-3} m s^{-1}. The deformation characteristic of G406 samples is however different (Figure 4.3(b)). These samples fail by axial cracking starting at the maximum stress following the linear elastic region, as shown by letter A in Figure 4.3(b). The axial cracking starts at the lower or stationary end of the sample and progresses to the upper end of the sample. After the axial cracking, the sample is fragmented in two pieces; thereafter into more pieces as the strain increases. The fragments of the fractured sample stay in contact with the compression test plate. The fractured pieces are hence continuously compressed by the plates. The quasi-static deformation characteristic of G406 samples is the axial cracking followed by both cracking and fragmentation.

(a)
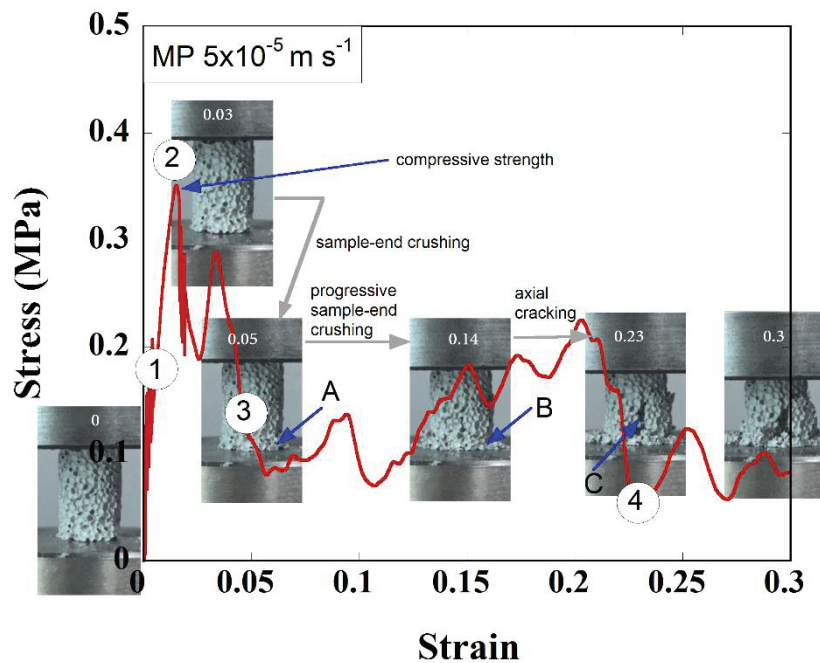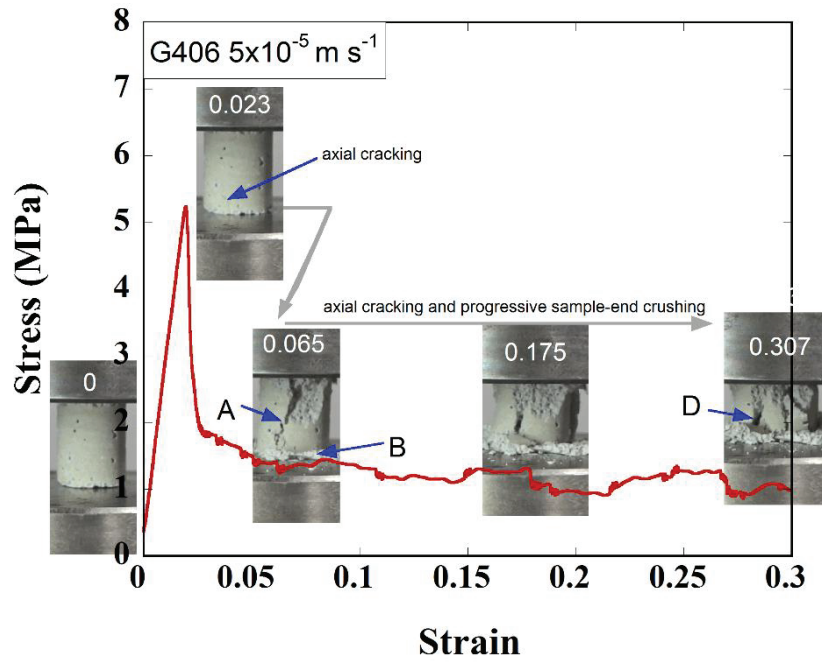
Figure 4.3. The stress-strain curve of (a) MP sample and (b) G406 sample together with the pictures of the deformed sample at various strains at $5x10^{-5}$ m s^{-1}

The low velocity compression test (1 m s^{-1}) stress-strain curves of G406 are shown in Figure 4.4. There are 7 tests in this figure and the average strain rate is 38 s^{-1}. The deformation behavior at low velocity is much similar with that of quasi-static velocity, except the maximum stress increases to 8.22 MPa.

The strain readings of MP samples in the SHPB tests could not be achieved precisely as these samples exhibited very small stresses, which were interfered with the noise of the strain gage amplifier. Typical SHPB incident and transmitter bar strain readings of G406 sample with and without pulse shaper as function of time are shown in Figure 4.5(a). As noted in the same figure, there is a time difference between the starting points of the reflected and transmitted waves for both with and without pulse shaper tests. This is the sample transit time and nearly 27 μs for both with and without pulse shaper tests (Figure 4.5(a)). The use of pulse shaper as seen in Figure 4.5(a) imposes a gradually increasing incident stress wave. The maximum strain reading on the transmitted wave corresponds to the fracture of the sample and allows to calculate the time to fracture. As seen in Figure 4.5(a), the sample tested without pulse shaper fractures at 45.5 μs. With the use of an aluminum pulse shaper the time to fracture

increases to 100 μs. The elastic modulus of G406 sample was determined ~0.75 GPa from the stress-strain curve at the same impact velocity. This correspond to an elastic wave velocity of 1118 m s^{-1} and a transit time of 23 μs which is very similar with the measured transit time of 27 μs. The ratio of the time to fracture to transit time (t_t/t_f) is calculated 1.68 and 3.7 for with and without pulse shaper tests shown in Figure 4.5(a). Since the stress equilibrium was established by using pulse shaper ($t_f \geq \pi t_t$), the SHPB tests were continued with the use of aluminum pulse shaper. It is noted in Figure 4.5(a) that the front and back strain gages mounted on the incident bar read almost the same strain and the time-shifted reflected strain reading of the front gage is very much similar to that of the back strain gage.   Figure 4.5(b) shows the variation of stress and strain rate with strain in a typical SHPB test using pulse shaper. As noted in the same figure, the strain rate varies with time during the test. The strain rate of the test was determined as the strain rate corresponding to the maximum or fracture stress. For the particular test shown in Figure 4.5(b); therefore, the strain rate at fracture is 165 s^{-1} and the compressive strength is 9.75 MPa.   Note that after the fracture, the strain rate increases since the sample becomes more compliant due to fracture.
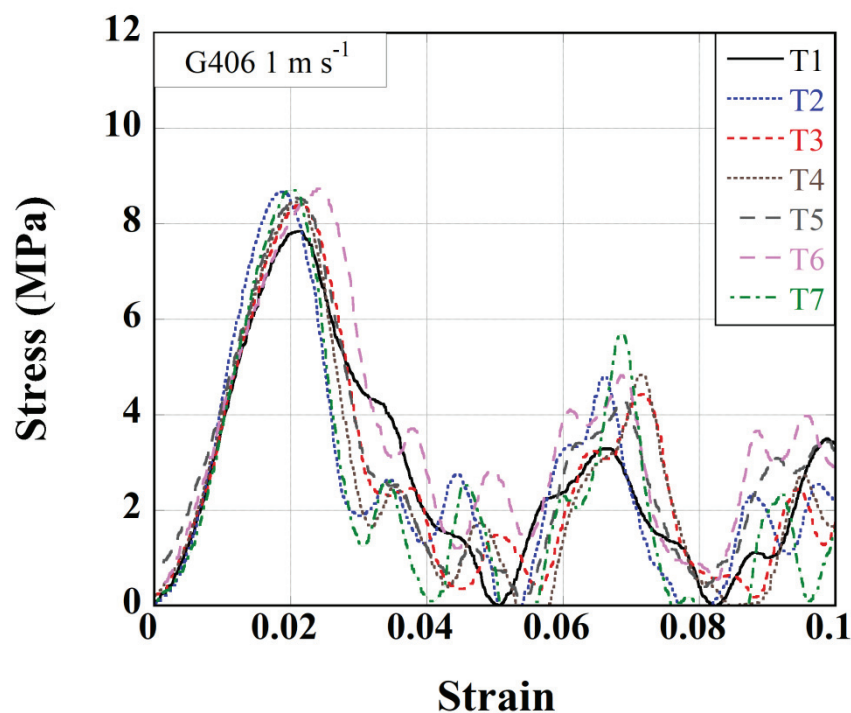
Figure 4.4. Low velocity compression stress-strain curves of G406
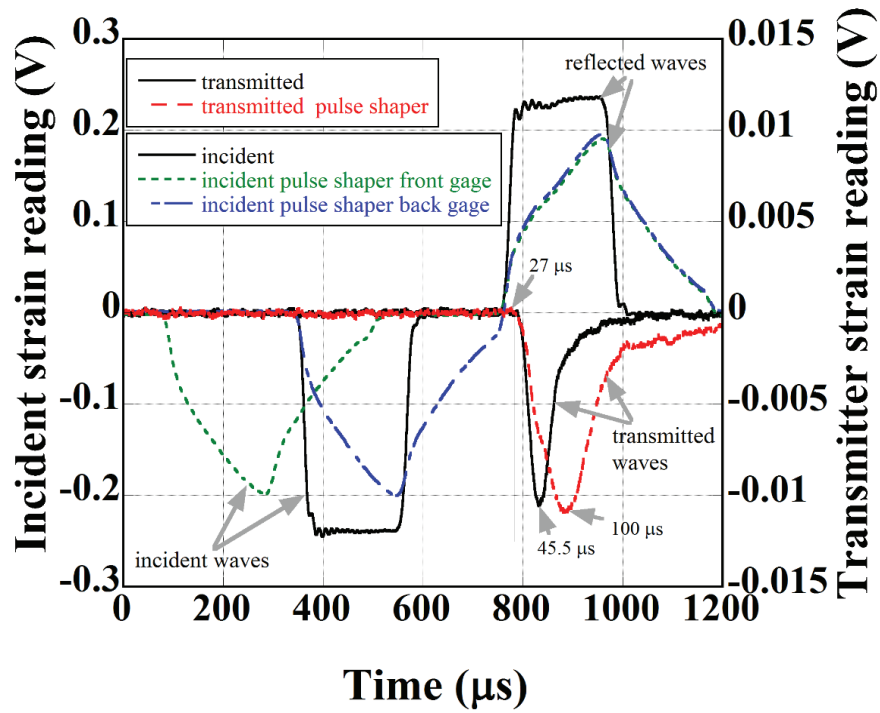
(a)
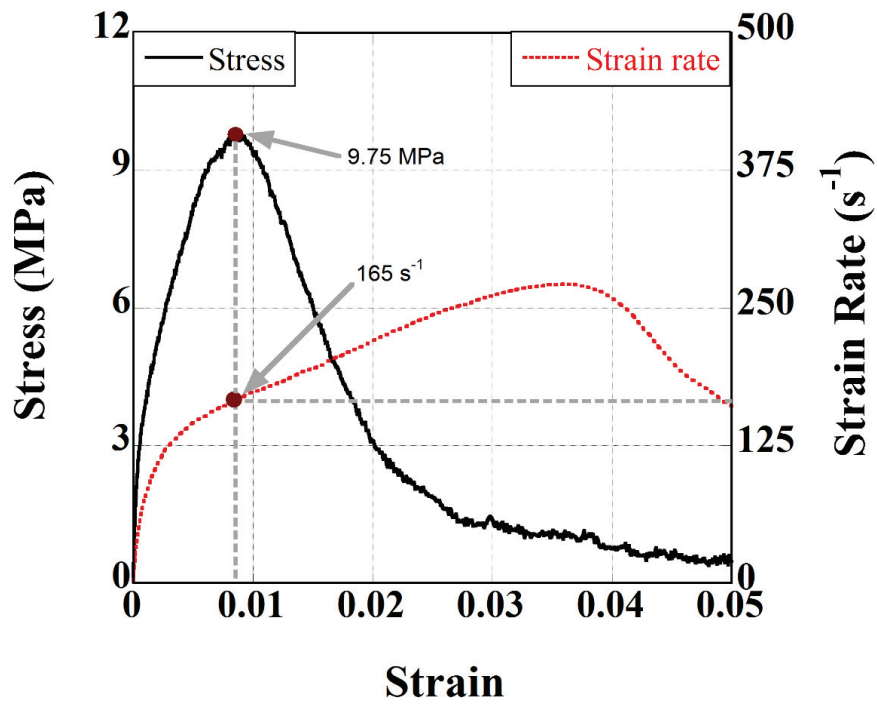
(b)

Figure 4.5. (a) SHPB incident and transmitter strain reading of the tests with and without pulse shaper and (b) typical stress-strain and strain rate-strain curve of SHPB test with pulse shaper

Figure 4.6(a) shows typical strain gage readings of the direct impact tests performed at 10 and 30 m s⁻¹. In these tests, the front and back strain gages were used to record the incoming wave after the impact of striker bar. As shown in Figure 4.6(a), the front and back gage readings at 10 m s⁻¹ impact (using 50 mm long Inconel bar) are almost the same, proving an insignificant wave dispersion on the used Inconel bars. The time to fracture at 10 m s⁻¹ is 49 μs, while it decreases to 34 μs at 30 m s⁻¹. These are non-equilibrium tests including axial inertia effects which will be elaborated in discussion section of the thesis. The corresponding stress-strain and strain rate-strain curves of the tests in Figure 4.6(a) are shown in Figure 4.6(b). The strain rate is sequentially 385 and 1150 s⁻¹ for the tests at 10 and 30 m s⁻¹. A constant strain rate is assumed in the direct impact test since the test sample is very compliant, absorbing only small portion of the kinetic energy of striker bar.

(a)
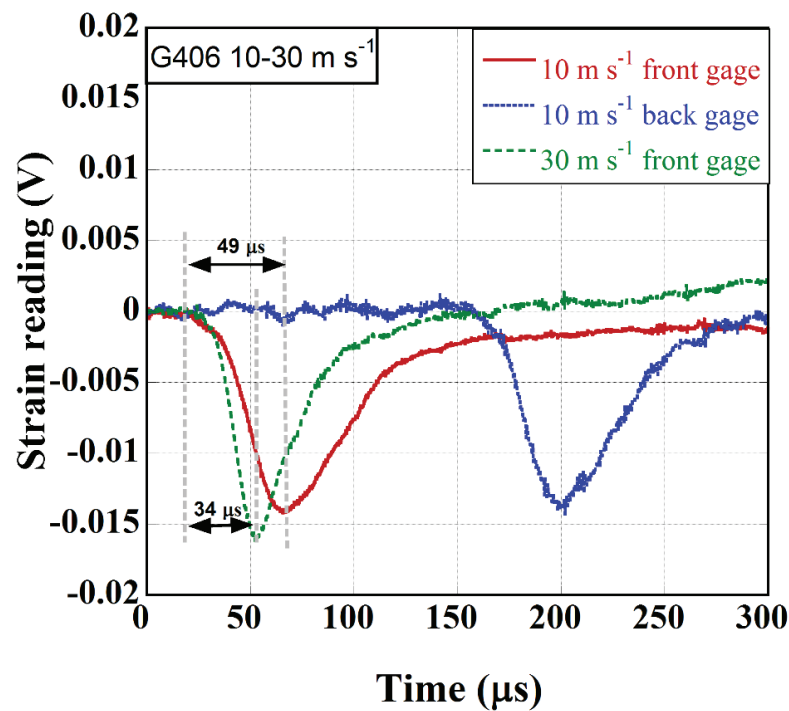
(cont. on next page)
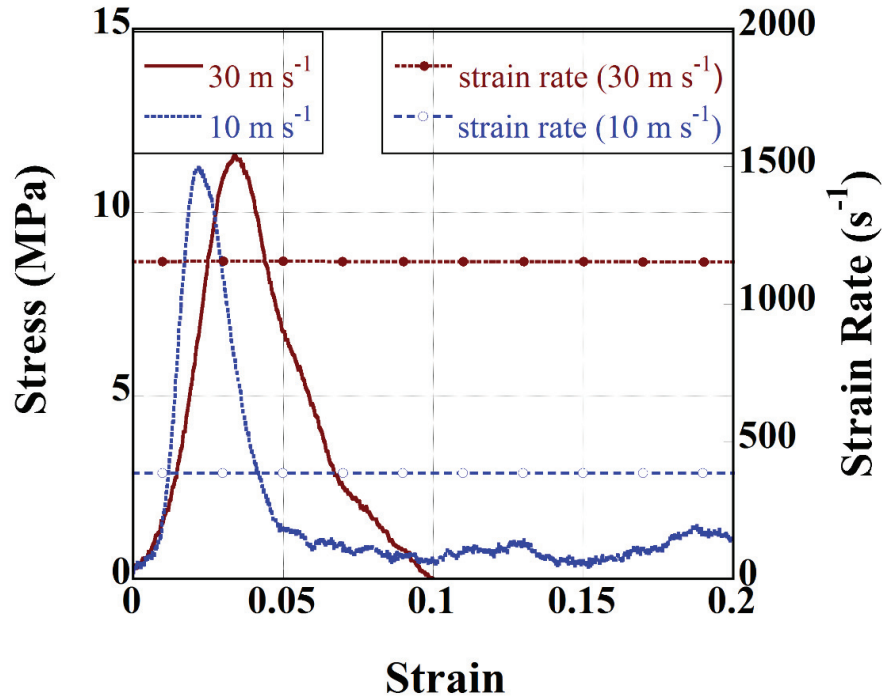
(b)

Figure 4.6. Direct impact tests (a) strain readings from the front and back gages and (b) stress-strain and strain rate-strain curves at 10 and 30 m s^{-1}

Figures 4.7(a), (b), (c) and (d) show sequentially the stress-strain curves of the G406 samples tested at 8, 10, 30 and 108 m s^{-1}. The stress-strain curves of the SHPB test at 8 m s^{-1} and the direct impact test at 10 m s^{-1} are similar as the test velocities are near to each other (Figures 4.7(a-b)), while the compressive strength slightly increases when the velocity increases to 30 m s^{-1}. The direct impact 108 m s^{-1} results in very large fracture strain values (Figure 4.7(d)), which will be discussed in discussion section. The Weibull survival probability-stress curves of dynamically tested samples are shown in Figure 4.7(e). The characteristic stress (σ_o when P_s=0.37) as seen in the inset of Figure 4.7(e) is 10.1, 10.3, 11.99 and 11.78 MPa at 8, 10, 30 and 108 m s^{-1}, respectively. These values are comparatively higher than those at quasi-static velocities; 5.11, 5.57 and 5.93 MPa for 5x10^{-5}, 5x10^{-4} and 5x10^{-3} m s^{-1}, respectively. The characteristic stress significantly increases with increasing the strain rate from quasi-static to dynamic. The Weibull modulus of dynamic tests are however comparable with those at quasi-static velocities and are 12.6, 18.2, 15.3 and 19 for 8, 10, 30 and 108 m s^{-1} tests, respectively.

(a)

(b)

(cont. on next page)

(c)

(d)

(cont. on next page)

G406

y = exp(-(m0/m1)^m2)	
	Value
m1	10.071
m2	12.576
R	0.98881

y = exp(-(m0/m1)^m2)	
	Value
m1	10.298
m2	18.171
R	0.97809

y = exp(-(m0/m1)^m2)	
	Value
m1	11.981
m2	14.474
R	0.94119

y = exp(-(m0/m1)^m2)	
	Value
m1	11.782
m2	19.084
R	0.97356

Legend: 8 m s^{-1}, 10 m s^{-1}, 30 m s^{-1}, 108 m s^{-1}
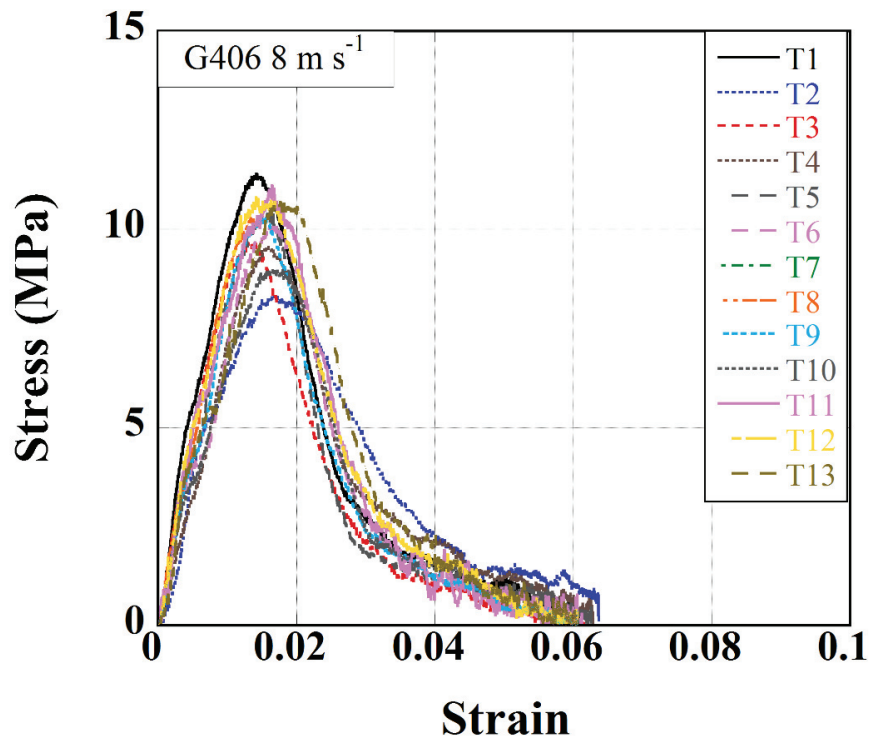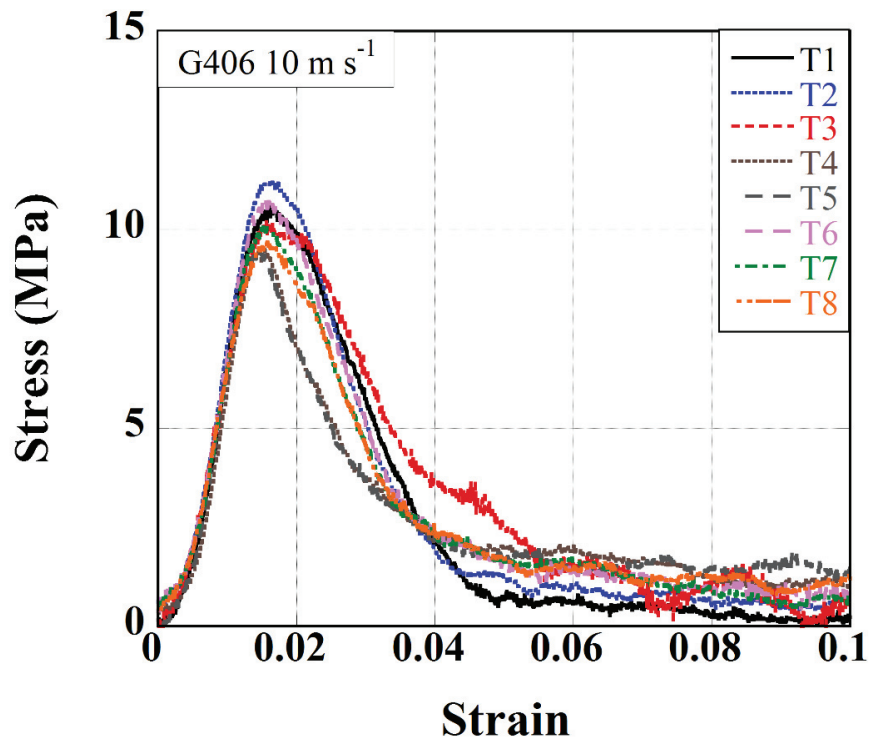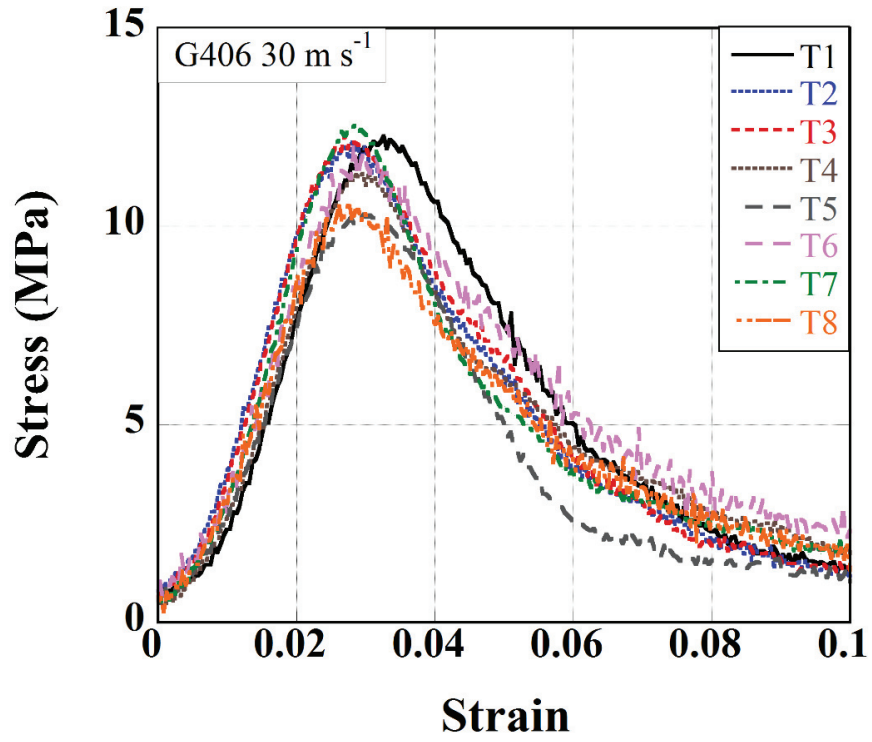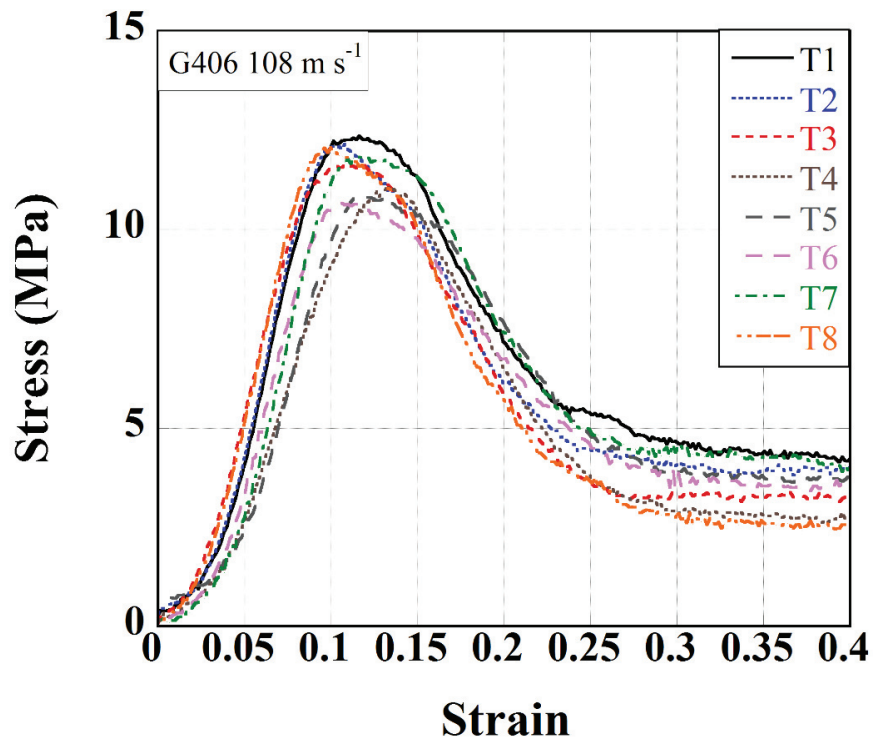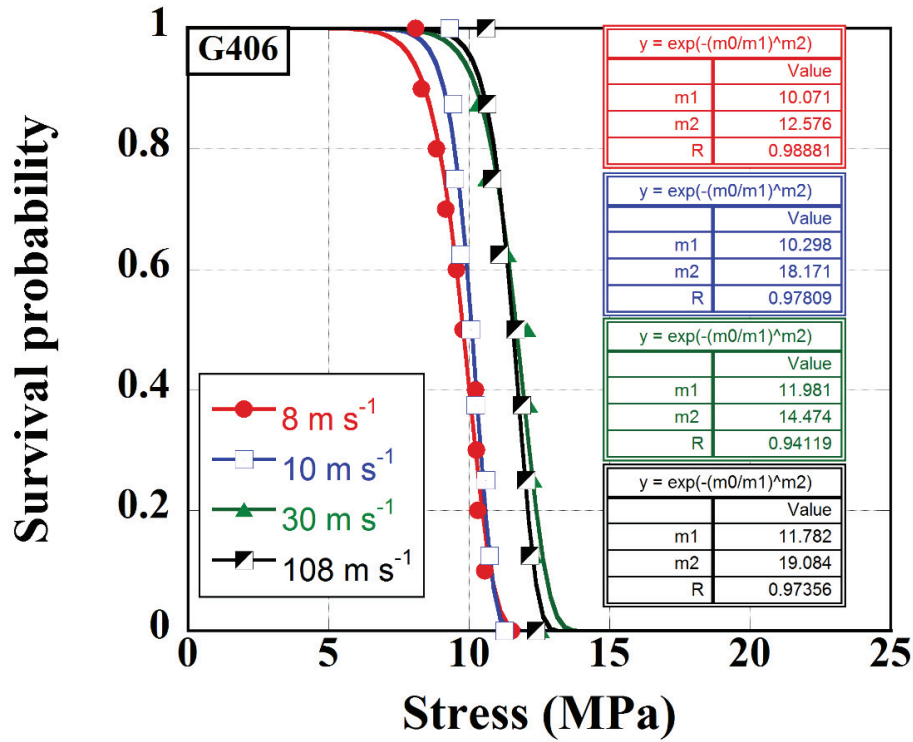
(e)

Figure 4.7. Dynamic compression stress-strain curves of G406 sample at (a) 8, (b) 10, (c) 30 and (d) 108 m s^{-1} and (e) Weibull survival probability–stress curves

Figures 4.8(a-c) show the pictures of MP samples tested at 5×10^{-5}, 5×10^{-4} and 5×10^{-3} m s^{-1} at increasing displacements. As stated earlier, MP samples tested at quasi-static velocities fail by progressive crushing at one of the sample/test platen contact region (marked by arrows in Figures 4.8(a-c)). The progressive crushing is followed by a single axial crack at increasing displacements. Almost the same failure mode is observed at all quasi-static velocities.

Figures 4.9(a-c) show the pictures of G406 samples tested at 5×10^{-5}, 5×10^{-4} and 5×10^{-3} m s^{-1} at increasing displacements. The failure of G406 samples starts with the appearance of a single axial crack at the bottom compression test platen as marked with arrows in Figures 4.9(a-c). Additional axial cracks are then formed as the pressure applied by the upper platen continues until about large displacements. Note that no progressive crushing is observed in these samples as apposite to MP samples and post failure stresses arise due to loading of the pieces of the fractured sample. Almost the same failure mode is observed at all quasi-static velocities.
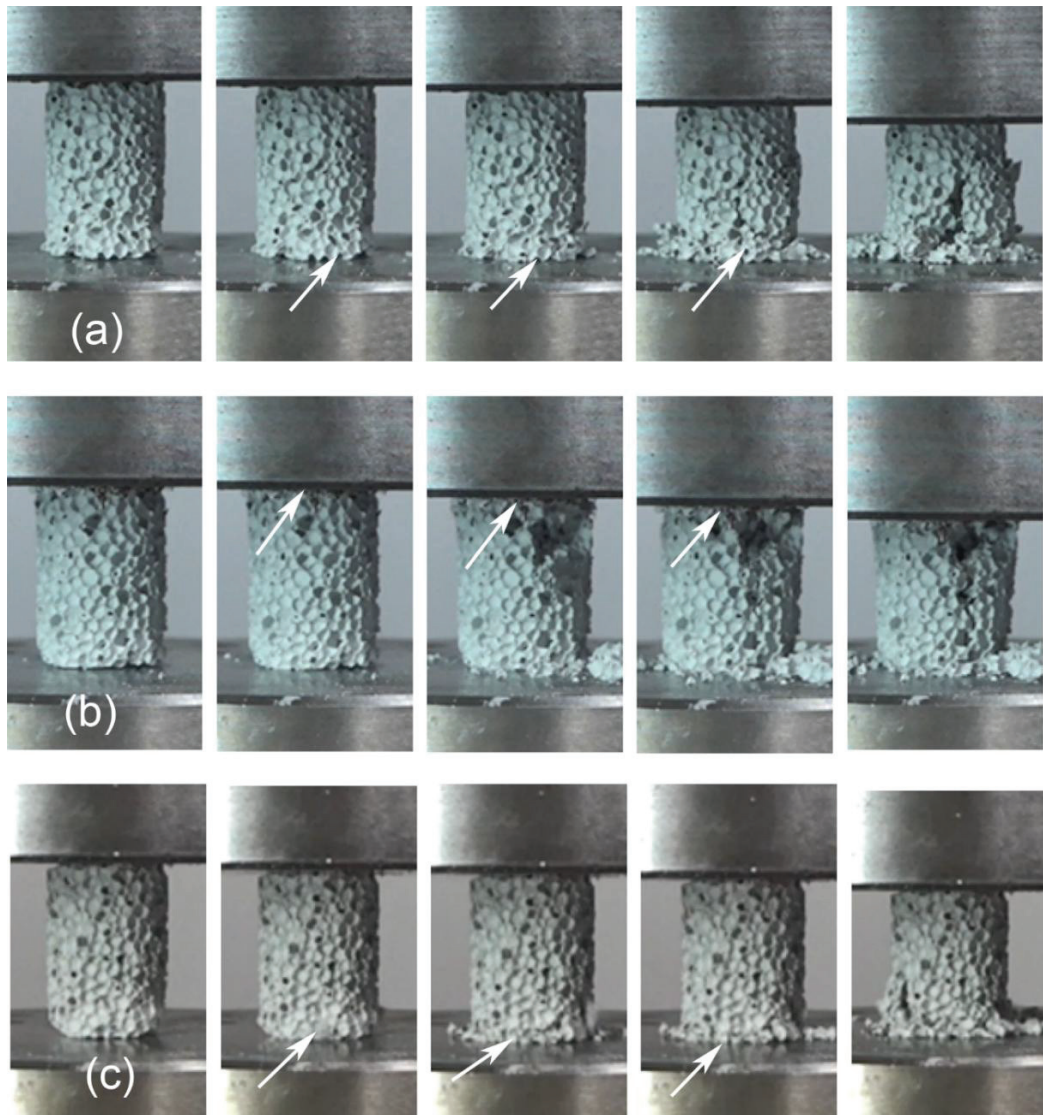
Figure 4.8.The deformation pictures of MP samples at (a) 5×10^{-5} , (b)5×10^{-4} and (c) 5×10^{-3} m s^{-1} at the displacements of 0, 0.761,1.50 3.66 and 6.16 mm (5×10^{-5} m s^{-1}); 0, 0.583, 1.65, 3.022 and 4.42 mm (5×10^{-4} m s^{-1}) and 0, 0.458, 1.472, 2.44 and 3.35 mm (5×10^{-3} m s^{-1})

The deformation pictures of G406 sample tested at 1 m s^{-1} are shown in Figure 4.10 at increasing strains. The failure occurs by the axial cracking and progressive crushing especially in the contact area of the impactor which are marked in Figure 4.9. The axial cracking behavior of G406 at low velocity impact is similar to that at quasi-static velocities.
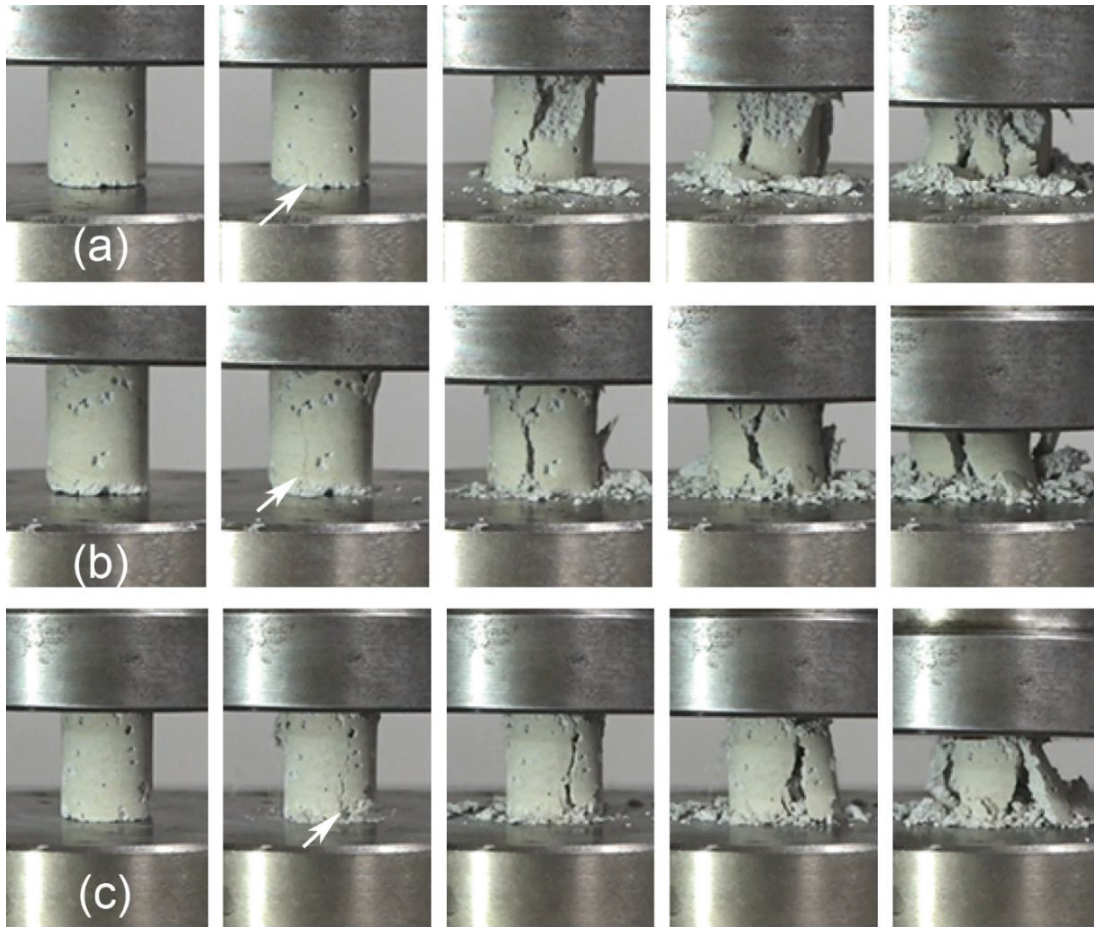
Figure 4.9. The deformation pictures of G406 samples at (a) 5×10^{-5}, (b)5×10^{-4} and (c) 5×10^{-3} m s^{-1} at the displacements of 0, 0.587, 1.681, 4.557 and 8 mm (5×10^{-5} m s^{-1}); 0, 0.546 2.2511, 4.551 and 8 mm (5×10^{-4} m s^{-1}) and 0, 0.497, 1.127, 3.049 and 8 mm (5×10^{-3} m s^{-1})
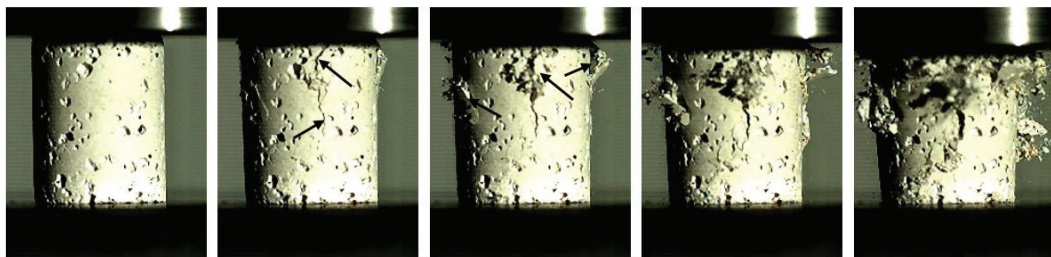
Figure 4.10. The pictures of the low velocity compression tested G406 sample at increasing displacements

Figures 4.11(a-d) show the pictures of G406 samples tested at 8, 10, 30 and 108 m s^{-1}. At 8 m s^{-1}, axial cracking starting from the sample/incident contact area is seen in Figure 4.11(a). These axial cracks proceed to the transmitter bar/sample interface. Similar axial cracking formation is also seen at 10 m s^{-1} direct impact test as shown by an arrow in Figure 4.11(b). However, at 30 and 108 m s^{-1} tests, the extensive cracking initially occurs near the sample/striker bar contact region before the cracking occurs at sample/incident bar contact region. The number of cracks also increases and both axial and radial cracks form at these velocities.

4.1.2. Indentation Tests

Figures 4.12(a) and (b) show the indentation force-displacement curves (at least 5 tests) of MP and G406 samples using 5 and 10 mm-diameter indenters at 5x10^{-5} m s^{-1}. A mean force of at least 5 tests was calculated for each indenter and sample type. The determined mean force-displacement curves of each indenter are also shown in Figures 4.12(a) and (b). As seen in these figures, the force values increase initially with increasing displacement, almost linearly, until the sample is indented by the indenter. Thereafter; the force becomes non-linear. Following the indenter penetration, the force values almost remain constant in MP samples (Figure 4.12(a)) with increasing displacement, while they increase with increasing displacement in G406 sample (Figure 4.12(b)).

Figures 4.13(a-c) show the indentation average stress-displacement curves of MP samples at 5x10^{-5}, 5x10^{-4} and 5x10^{-3} m s^{-1}, respectively. The stress was calculated by dividing the mean force to the indentation area. At each velocity, the effect of indenter diameter is clearly seen in these figures. As the size of the indenter increases, the indentation stress decreases, while a tendency of indentation stress saturation is seen at larger indenter diameters, 25 and 30 mm. A comparison graph of the effect of indenter size is shown in Figure 4.13(d) where the stress of 5 and 30 mm indenter at three different velocities are drawn. Again as the indenter diameter increases, the indentation stress decreases. The effect of velocity is also seen in Figure 4.13(d); increasing indenter velocity from 5x10^{-5} to 5x10^{-4} and 5x10^{-3} m s^{-1}, the indentation stress increases.

Figure 4.11. Dynamic deformation pictures of G406 sample at (a) 8, (b) 10, (c) 30 and (d) 108 m s^{-1} (50 micro second interval)

Figures 4.14(a-c) show the indentation average stress-displacement curves of G406 samples at 5×10^{-5}, 5×10^{-4} and 5×10^{-3} m s^{-1}, respectively. At each velocity, the effect of indenter diameter is also clearly seen; as the size of the indenter increases, the indentation stress decreases, while a tendency for stress saturation is seen at larger indenter diameters, 25 and 30 mm. The indentation stress is also noted to increase with increasing the indentation velocity. A comparison graph of the effect of indenter size is shown in Figure 4.14(d) in which 5, 15 and 30 mm indenter stresses at three different velocities are drawn. The effect of velocity is also seen in Figure 4.14(d); increasing indenter velocity from 5×10^{-5} to 5×10^{-4} and 5×10^{-3} m s^{-1}, the indentation stress also increases, while the effect of velocity is more pronounce on the post indentation stress values.
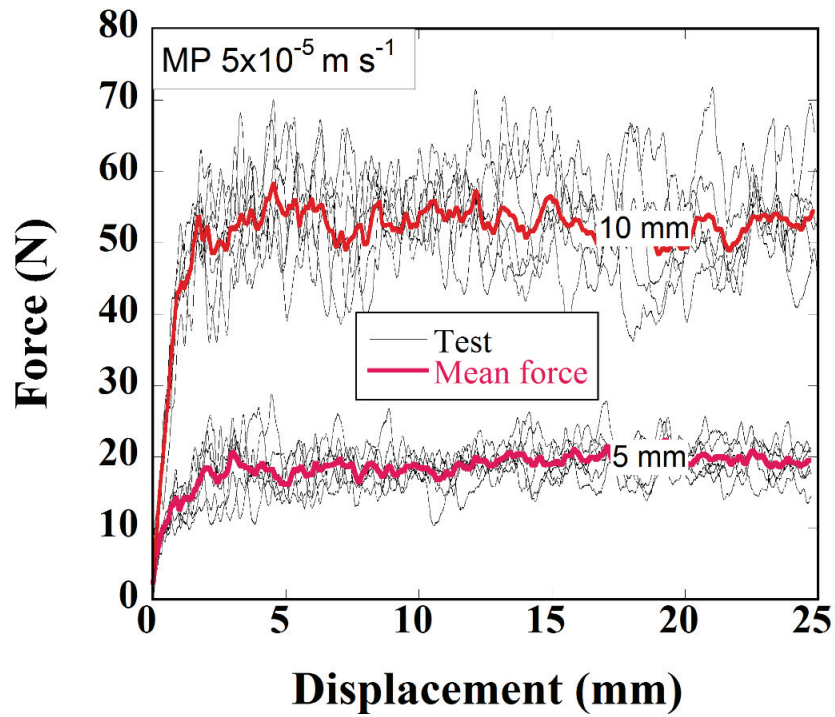
(a)
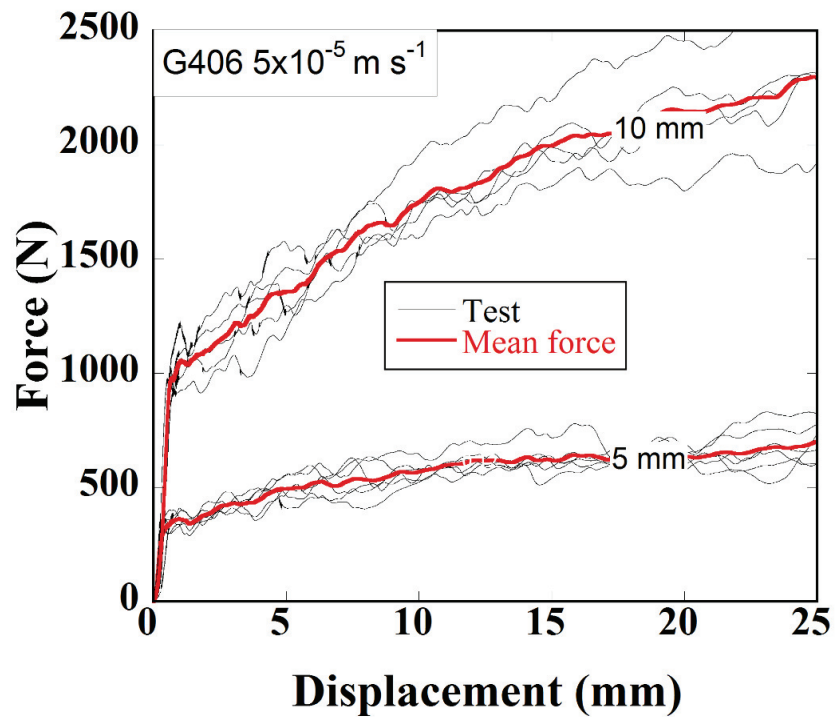
(b)

Figure 4.12. Indentation force-displacement curves of 5 and 10 mm-diameter indenter and mean force-displacement curves at 5×10^{-5} m s^{-1} (a) MP and (b) G406

(a)

(b)
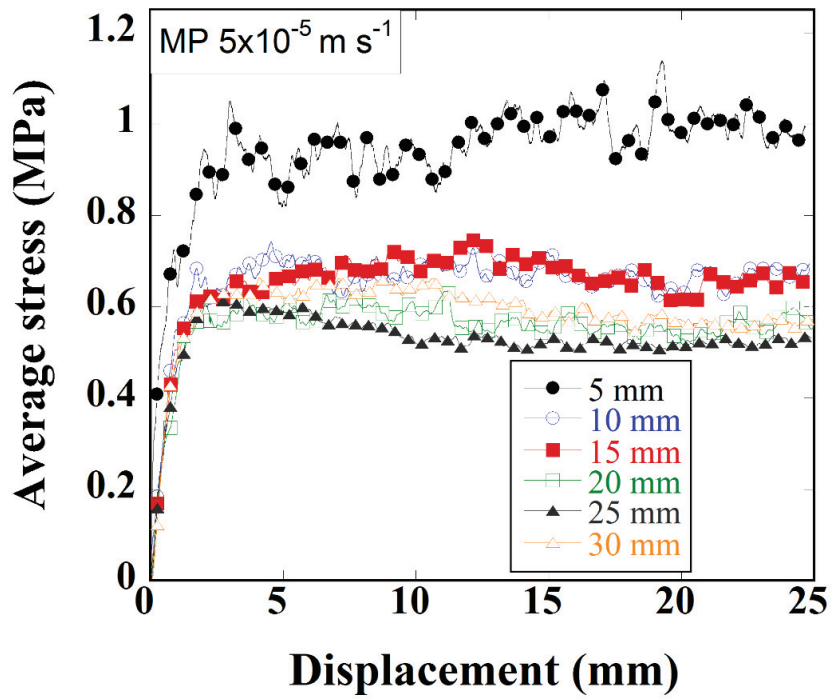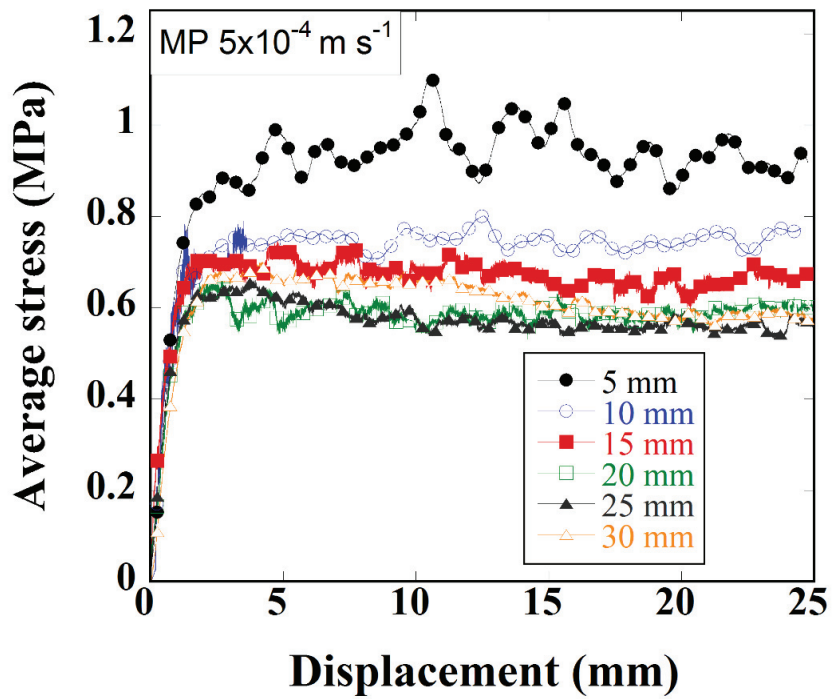
(cont. on next page)
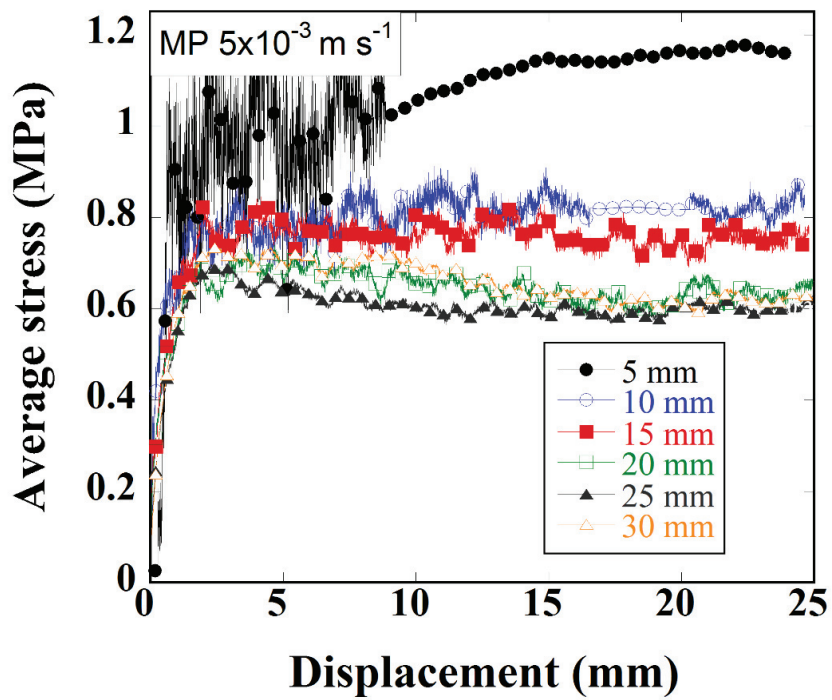
(c)
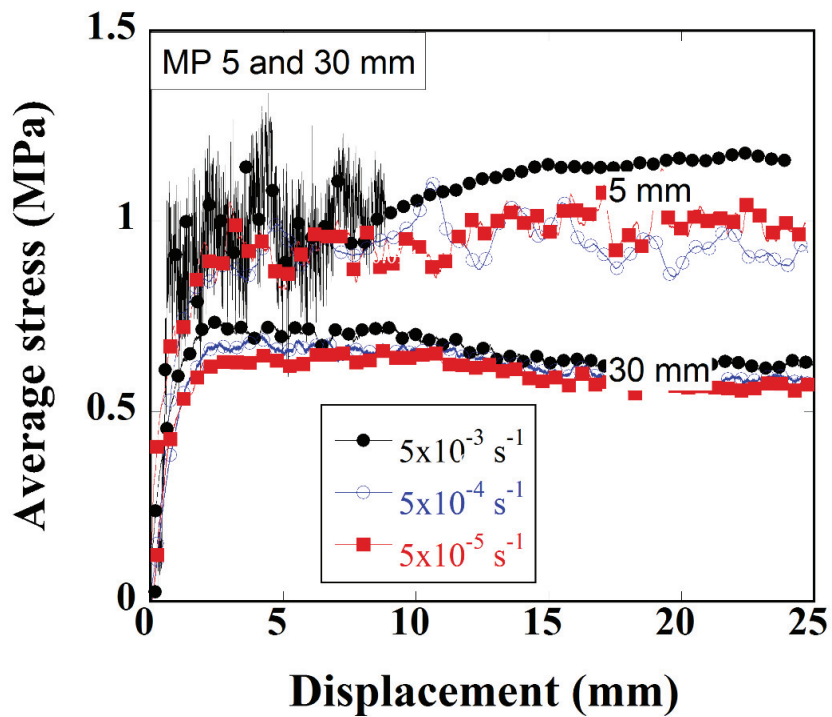
(d)

Figure 4.13. Indentation average stress-displacement curves of MP at (a) 5x10⁻⁵, (b) 5x10⁻⁴ and (c) 5x10⁻³ m s⁻¹ and (d) average stress-displacement curves using 5 and 30 mm indenters at 5x10⁻⁵, 5x10⁻⁴ and 5x10⁻³ m s⁻¹

(a)

(b)

(cont. on next page)
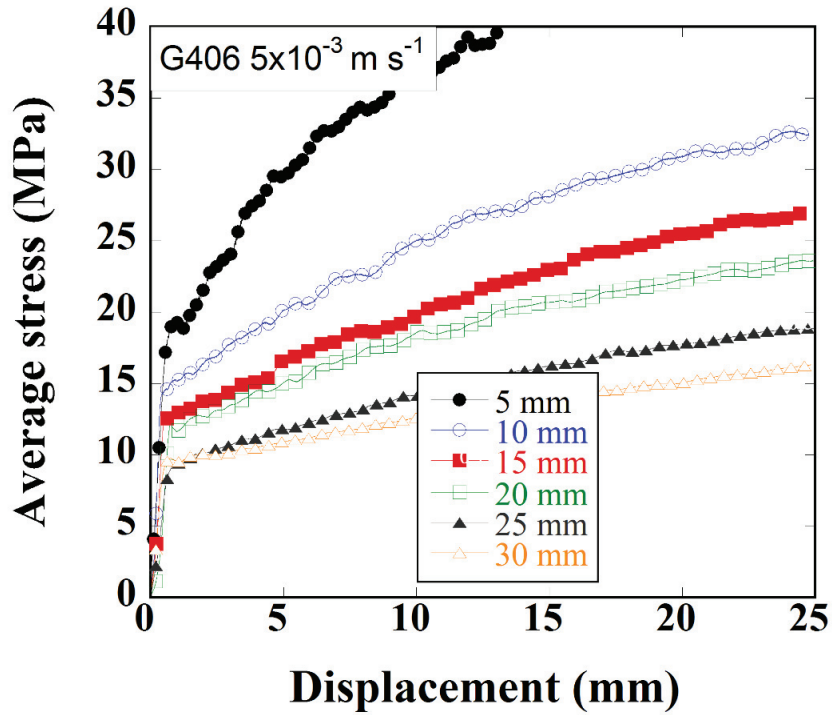
(c)
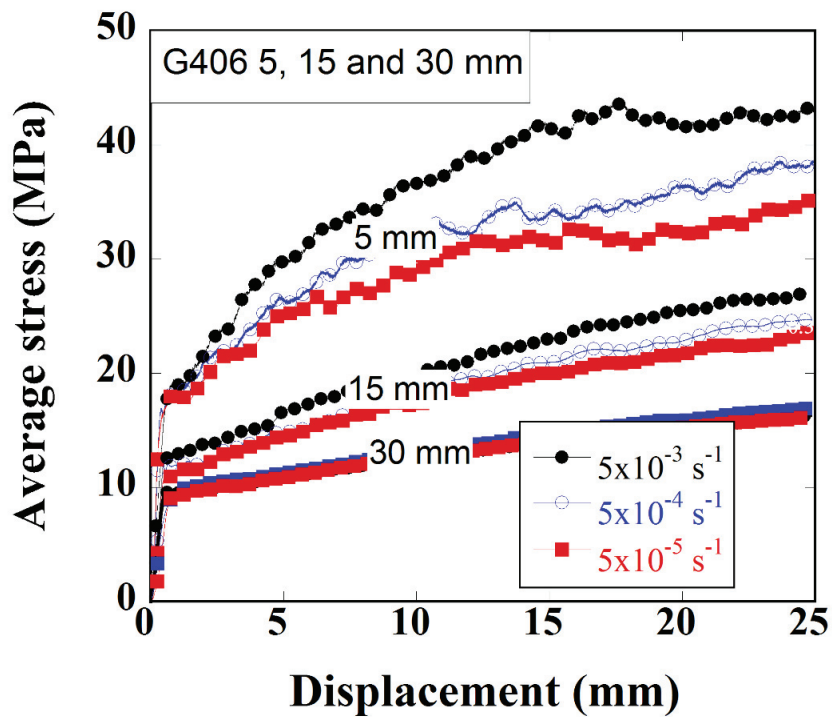
(d)

Figure 4.14. Average indentation stress-displacement curves of G406 at (a) 5×10^{-5} , (b) 5×10^{-4} and (c) 5×10^{-3} m s^{-1} and (d) average stress-displacement curves using 5, 15 and 30 mm indenters at 5×10^{-5}, 5×10^{-4} and 5×10^{-3} m s^{-1}

Figures 4.15(a-b) show the indentation stress-displacement curves of MP and G406 samples using 20 mm-diameter indenter at 5×10^{-5}, 5×10^{-4} and 5×10^{-3} m s^{-1}, respectively. In order to calculate the average indentation stress (corresponding to the point at which the indenter penetrates the sample), a linear line is drawn in the plateau region of the curves as shown in Figures 4.15(a) and (b). The intercept of this line with the tangent line drawn in the linear elastic region is taken as the indentation stress. As seen in Figures 4.13(a) and (b), both MP and G406 samples exhibit velocity dependent indentation stress; the indentation stress increases with increasing indentation velocity.

(a)
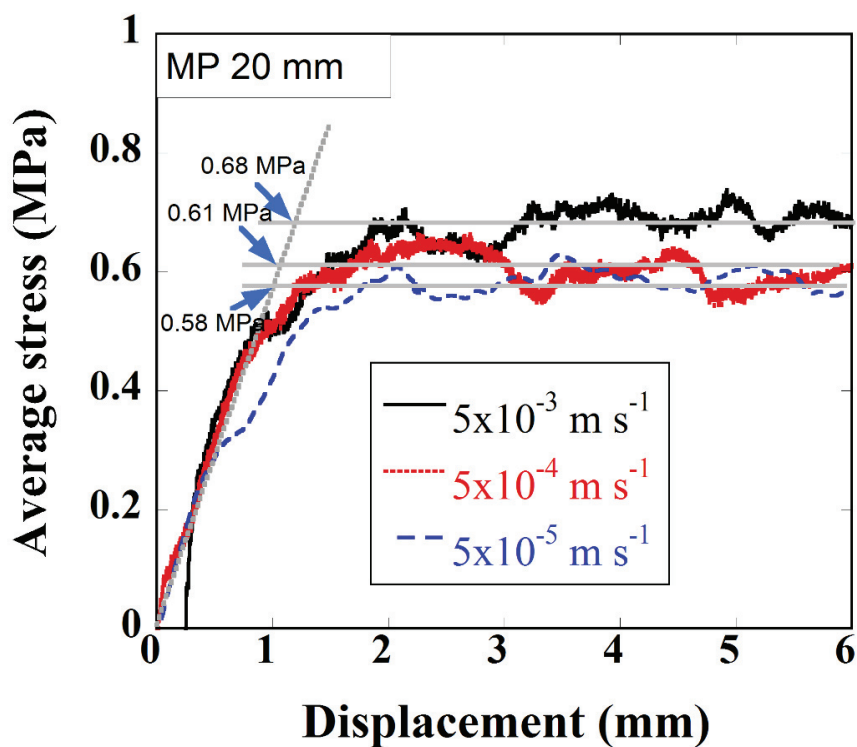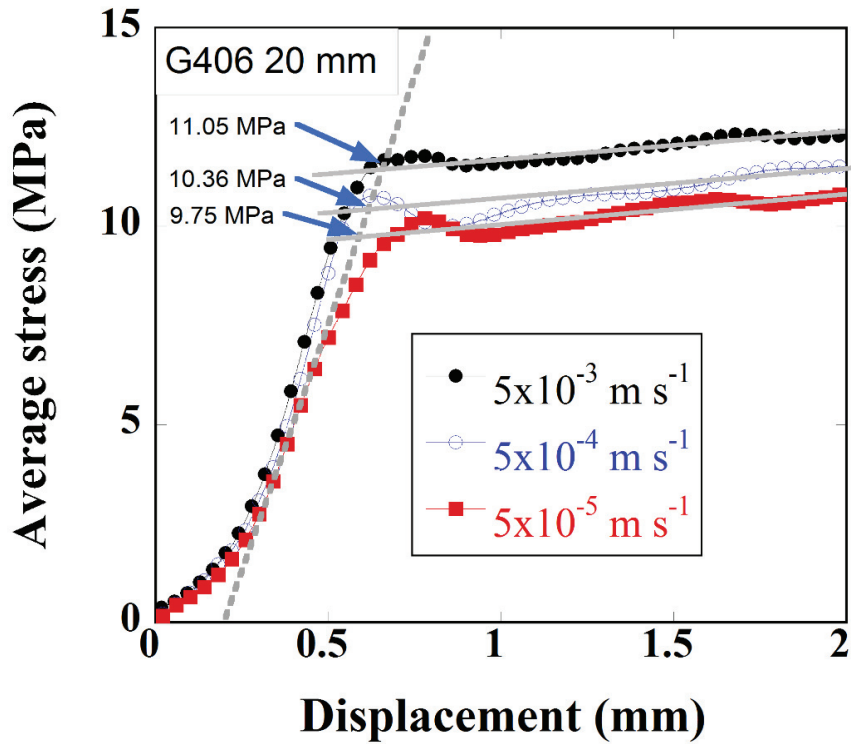
(b)

Figure 4.15. Indentation stress-displacement curves using 20 mm indenter at different
velocities (a) MP and (b) G406

Figure 4.16 shows the pictures of the cross-section of indented MP samples as function indenter diameter (5-30 mm) and velocity (5×10^{-5} 5×10^{-4} and 5×10^{-3} m s^{-1}) at a final displacement of 25 mm. As the indenter penetrates, the crushed AAC powder accumulates at the tip of the indenter as seen in Figure 4.16. The length of the powder accumulated region is less than the total displacement and the diameter of that region is the same as the diameter of the indenter, as marked with white border line in Figure 4.16. Almost no effect of velocity is found on the powder accumulated region area of MP samples. Figure 4.17 shows the pictures of indentation cross-section of G406 samples as function indenter diameter (5- 30 mm) and velocity (5×10^{-5} 5×10^{-4} and 5×10^{-3} m s^{-1}) at a final displacement of 25 mm. The length of the powder accumulated region is comparable with the total displacement and the diameter of the powder accumulated zone gets bigger than the indenter size away from the indenter tip, as marked with white border line in Figure 4.17. Similar with MP samples, G406 samples also show almost no effect of velocity on the powder accumulated region area.
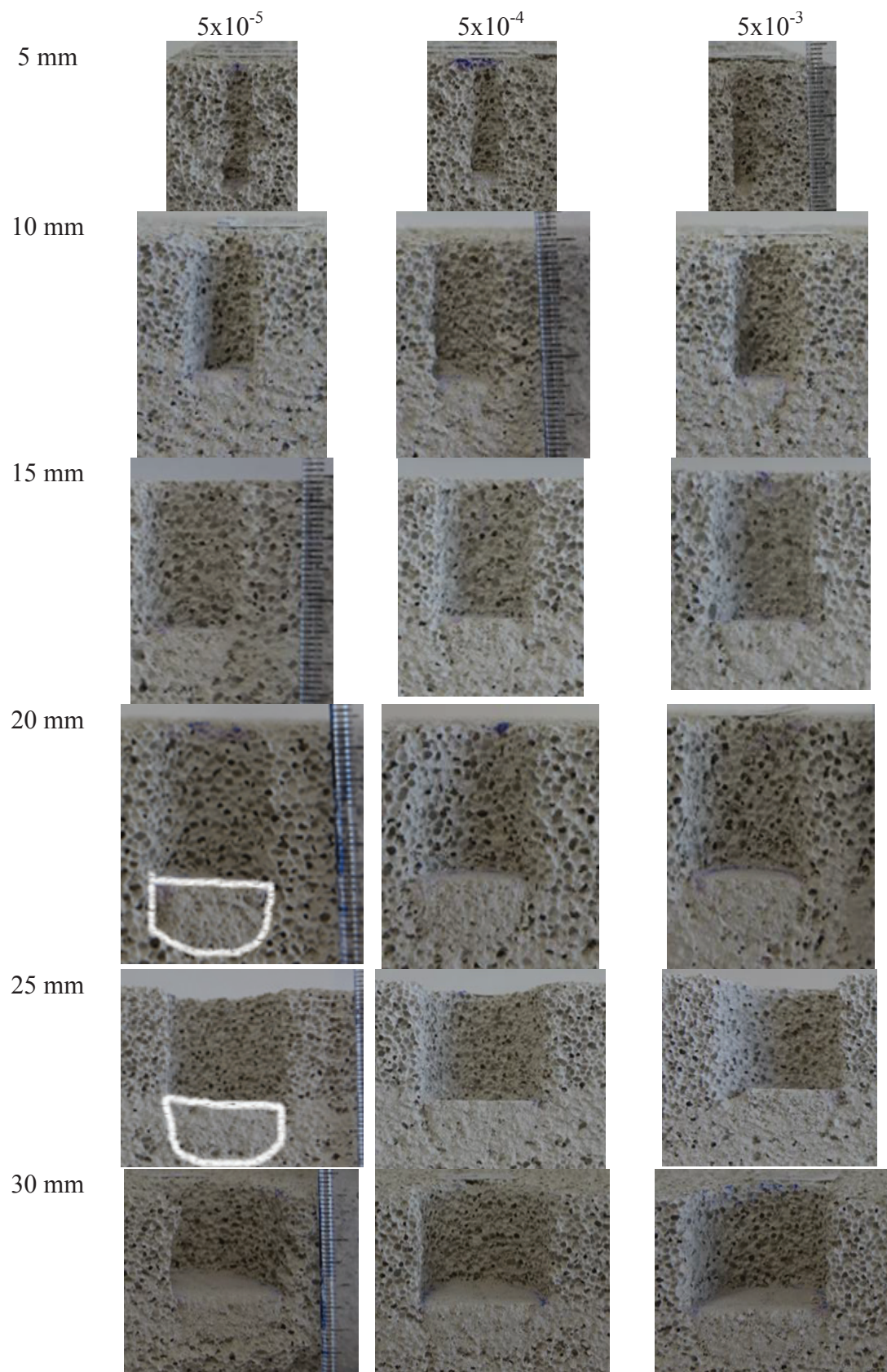
Figure 4.16. The powder accumulation of MP projected by the indenters at 5×10^{-5}, 5×10^{-4} and 5×10^{-3} m s^{-1}
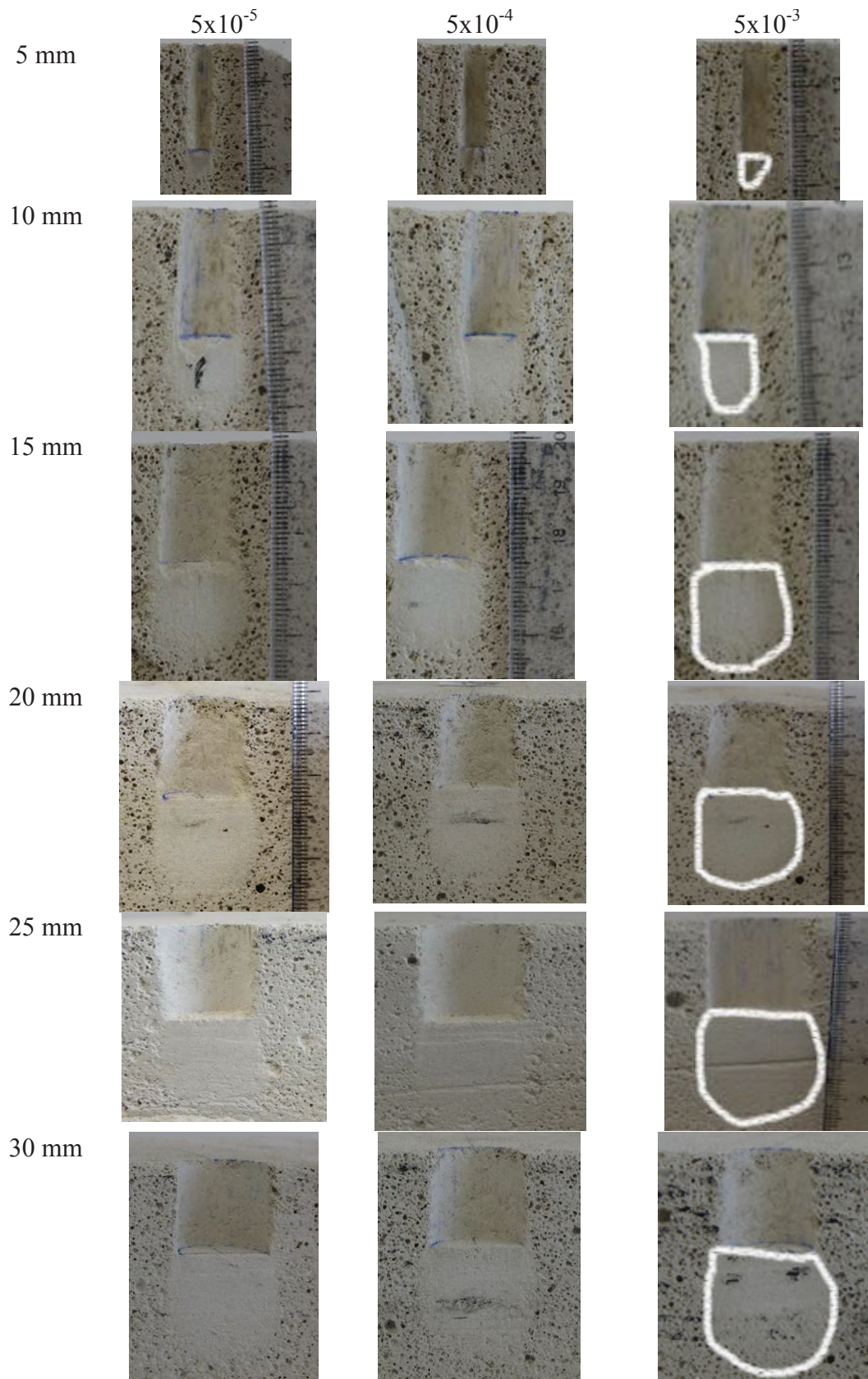
Figure 4.17. The powder accumulation of G406 projected by the indenters at 5x10^{-5}, 5x10^{-4} and 5x10^{-3} m s^{-1}

4.1.3. Confined Compression Tests

Figures 4.18(a) and (b) show the quasi-static stress-strain curves of confined G406 samples at 5×10^{-4} m s^{-1} until about large strain (0.4) and low strain (0.07), respectively. The corresponding quasi-static strain rate is 2×10^{-2} s^{-1}. The sample is compressed (densify) until about large strains without fracture as depicted in Figure 4.18(a). Initially a linear elastic region is seen in Figure 4.18(b) and this is followed by a non-linear increase of the stress values after about a strain of 0.02. The corresponding stress at about 0.02 strain is taken as the confined compressive strength and it varies between 4.76 and 8.51 MPa. The SHPB test incident, reflected and transmitted waves of confined compression test at 8 m s^{-1} are shown in Figure 4.18(c). The corresponding strain rate in this tests is approximately 330 s^{-1}. No pulse shaper was used in these tests. The time difference between starting points of the reflected and transmitted waves is ~27 µs. After the test, the confinement tube is not relaxed quickly, which imposes a residual stress on the transmitter bar as seen in Figure 4.18(c). The resultant confined compression stress-strain curves at 8 m s^{-1} SHPB tests are shown in Figure 4.18(d). The confined compression strength of SHPB tests shown in Figure 4.18(e) are higher than of those of quasi-static velocity and range 6.45-10.5 MPa.

(a)
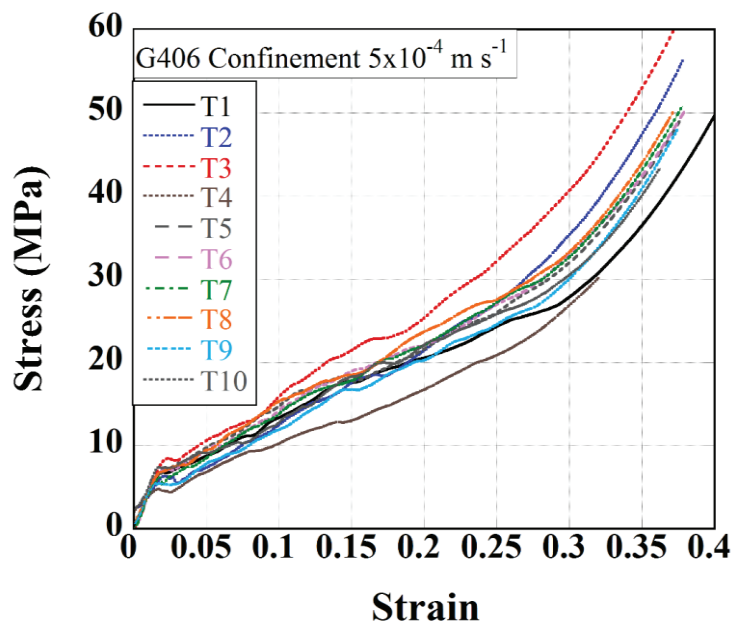
(cont. on next page)
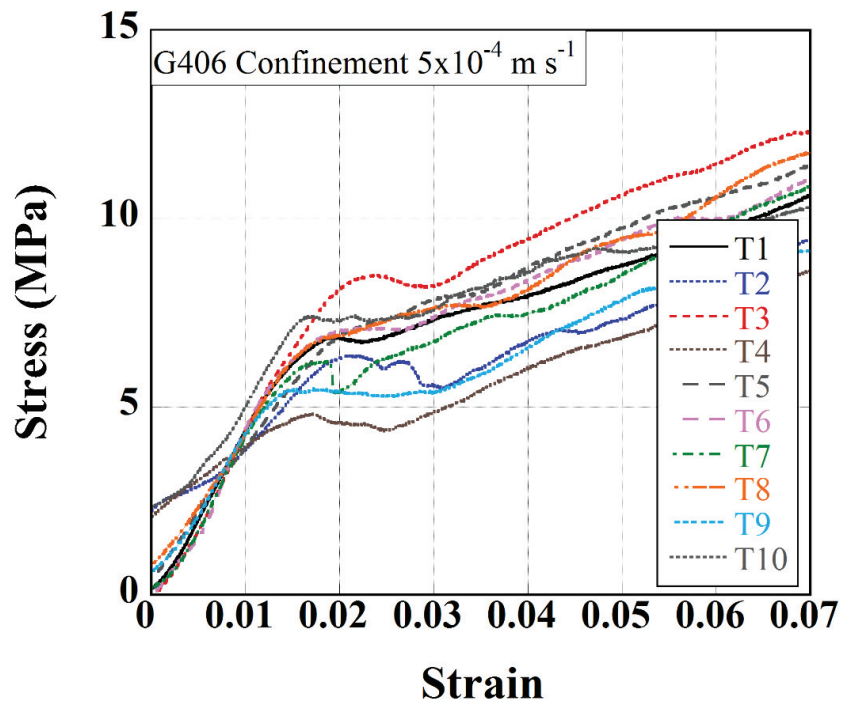
(b)
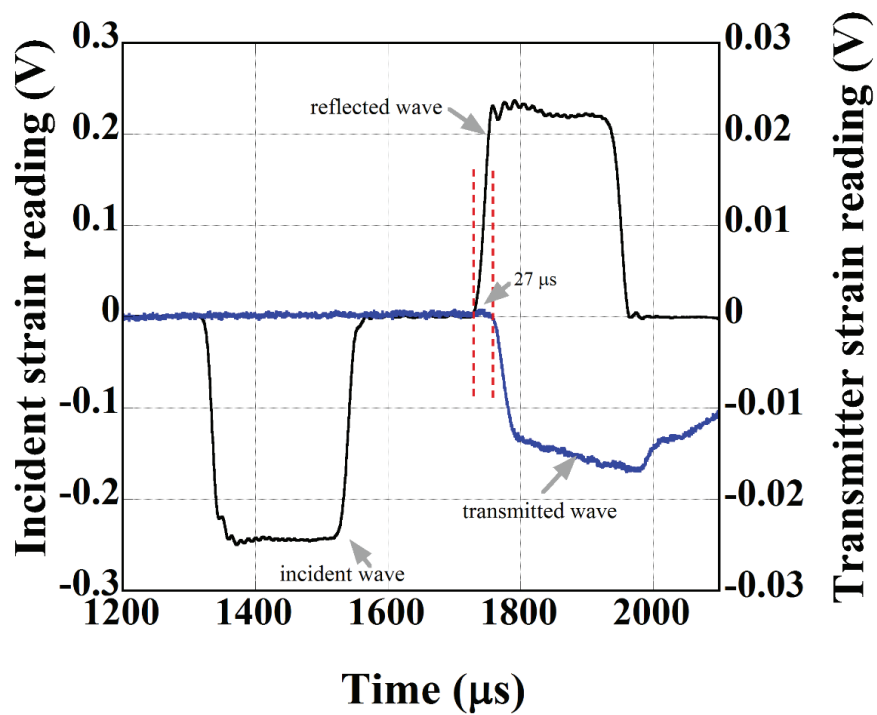
(c)

(cont. on next page)
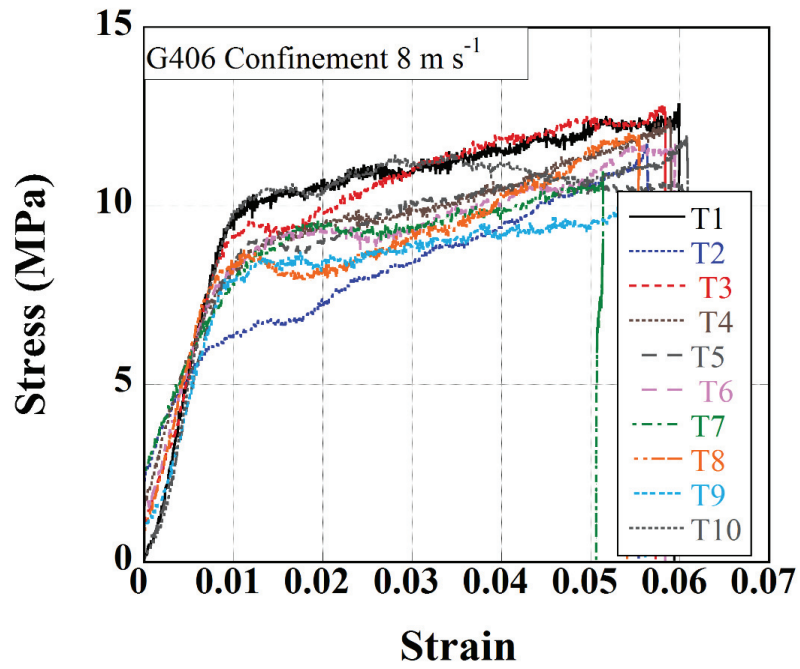
(d)
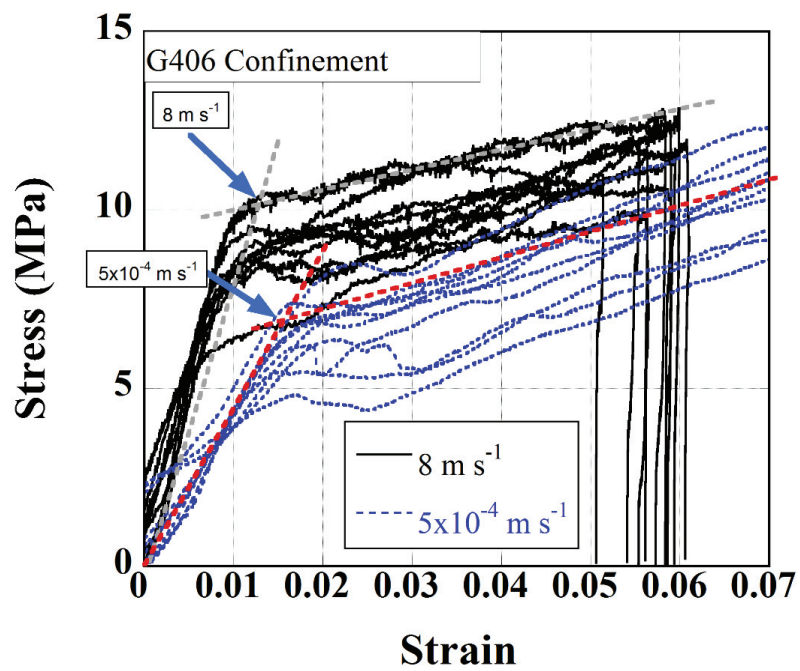
(e)

Figure 4.18. The stress-strain curves of confined G406 samples at (a) and (b) 5×10^{-4}, (c) the incident transmitter waves in SHPB at 8 m s^{-1}, (d) the stress-strain curves of confined G406 samples at 8 m s^{-1} and (e) the stress-strain curves of confined G406 samples at 5×10^{-4} and 8 m s^{-1}

Figure 4.19(a) shows the picture of confined test sample before a test and Figures 4.16(b-c) show after a quasi-static test at 5×10^{-4} m s^{-1} until 0.4 strain and after SHPB test at 8 m s^{-1} until 0.06 strain, respectively. The test samples were densified as the strain increases without fracture.
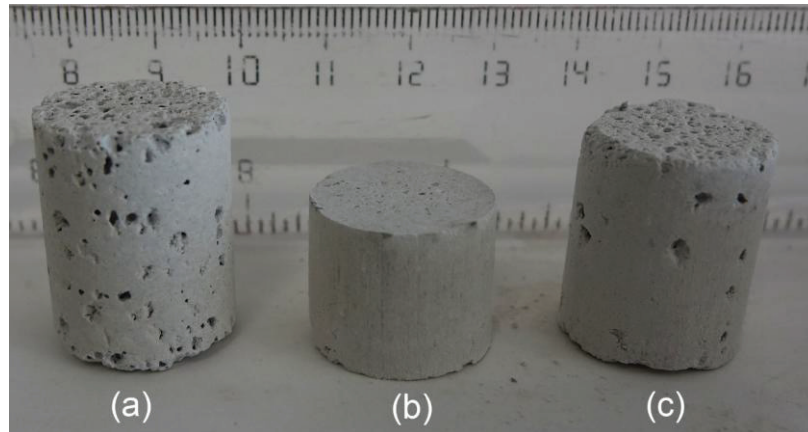
Figure 4.19. The pictures of G406 confined compression test samples (a) before the test and after the test; (b) 5×10^{-4} m s^{-1} until 0.4 strain and (c) 8 m s^{-1} until 0.06 strain

4.1.4. Brazilian Tests

Typical SHPB strain gage readings of the Brazilian test at 8 m s^{-1} are shown in Figure 4.20(a). Figure 4.20 (b) shows three Brazilian test stress-strain curves of G406 sample at 5×10^{-5} and 8 m s^{-1}. The mean Brazilian peak stresses of G406 are 1.05 and 1.5 MPa at 5×10^{-5} and 8 m s^{-1}, respectively. The indirect splitting tensile strength of G406 increases with increasing strain rate. The Brazilian test pictures of G406 samples are shown in Figures 4.21(a-b) at 5×10^{-5} and 8 m s^{-1}, respectively. At both quasi-static and dynamic velocities, a central crack develops and splits the sample in two pieces as seen in the figures.
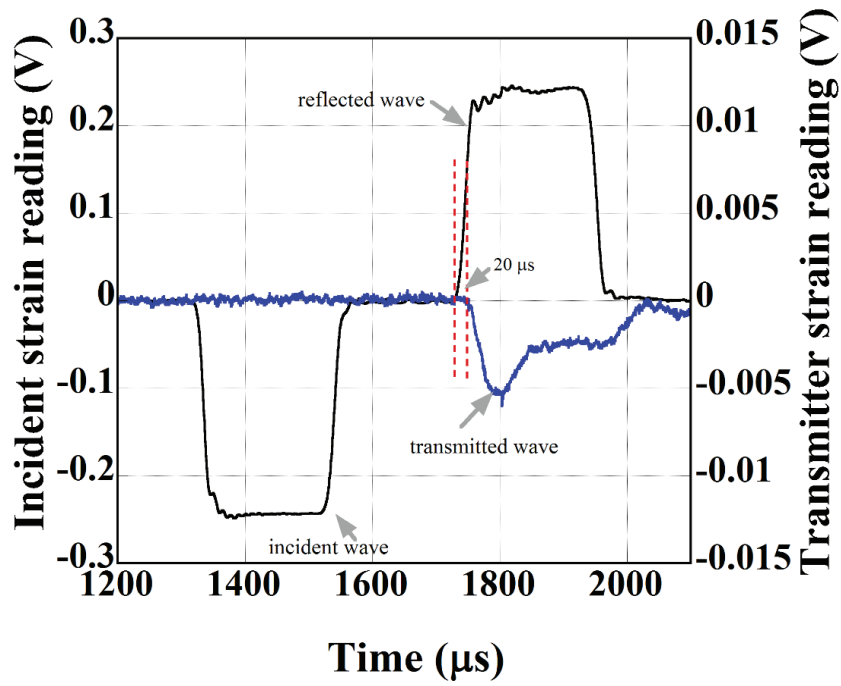
(a)
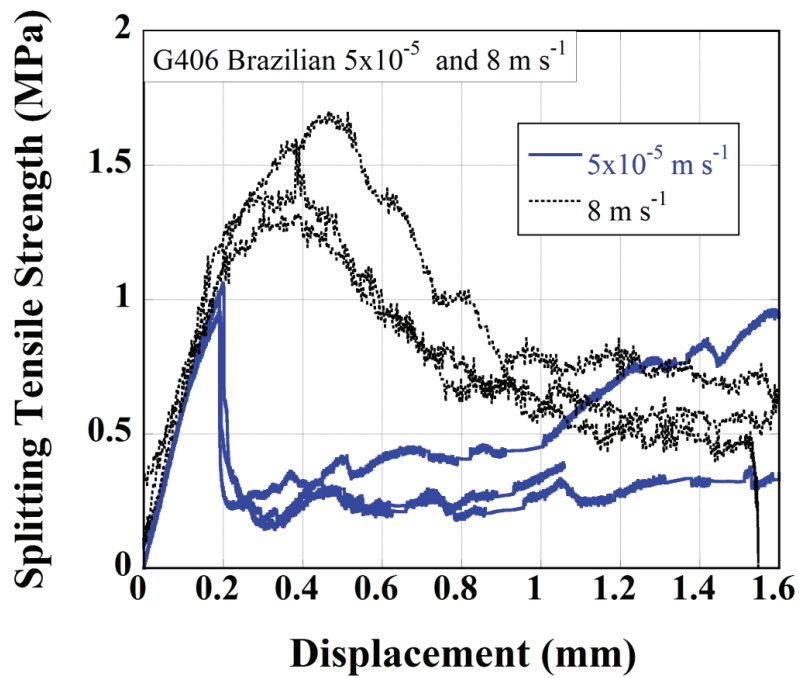
(b)

Figure 4.20. (a) typical SHPB incident and transmitted strain gage readings in the Brazilian test and (b) the Brazilian test stress-displacement curves of G406 sample at 5×10^{-5} and 8 m s^{-1}
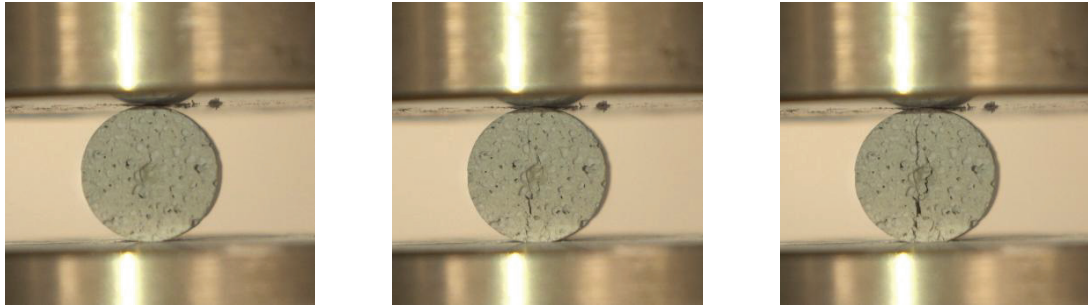
(a)
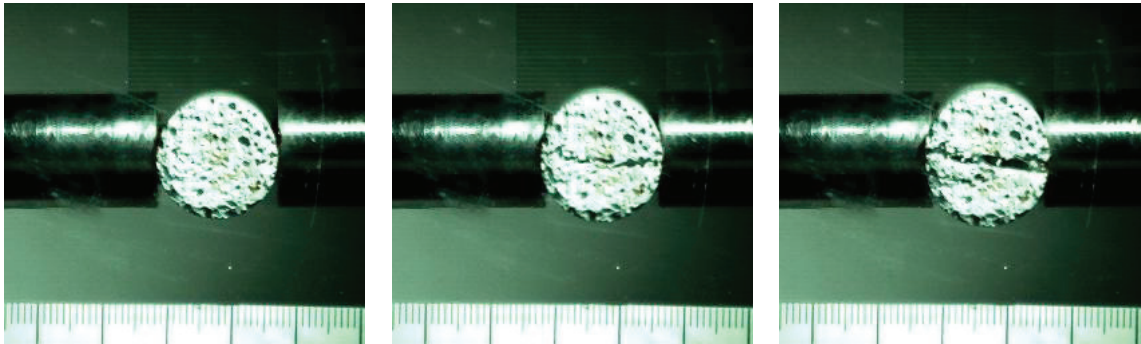
(b)

Figure 4.21. The Brazilian test pictures of G406 samples showing central axial cracks at (a) 5×10^{-5} and (b) 8 m s^{-1}

4.2. Numerical Results

4.2.1. Quasi-static Test Model

The bottom and top contact stresses of 5×10^{-3} m s^{-1} model are shown in Figure 4.22. The numerical top-plate and bottom-plate contact compressive strengths are nearly the same, 5.37 and 5.38 MPa respectively. This shows the stress equilibrium state in the test. Figure 4.23 shows the numerical deformation pictures of numerical quasi-static test at 5×10^{-3} m s^{-1}. Cracks initiate at the top plate at 130 s. These cracks proceed axially in the loading direction. At increasing times between 520 and 780 s, cracks reach the bottom plate causing the separation of the large pieces of the sample.

4.2.2. SHPB Test Models

The SHPB test numerical model stresses taken from incident bar/sample and transmitter bar/sample contact area, transmitter bar/sample contact center and surface element and the transmitter bar strain gage location are shown in Figures 4.24(a) and (b) at 1 and 8 m s^{-1} striker bar velocities without pulse shaper, respectively. At 1 m s^{-1}, the stresses at the incident and transmitter bar/sample contacts are almost the same showing stress equilibrium between incident and transmitter bars. As the transmitter bar/sample contact area center and surface element stresses are similar, both radial and axial inertia effects are insignificant at this velocity. The sample fails by forming axial cracks as will be elaborated later in this section. The maximum numerical compressive strength is nearly 5.1 MPa, which is the same as the quasi-static compressive strength used in the model. At 8 m s^{-1} (Figure 4.24(b)), there is a time lag between the incident and transmitter bar/sample contact stresses, 33 μs, corresponding to the sample transit time. The maximum incident and transmitter bar/sample contact stresses are 5.2 and 5.26 MPa, respectively. The transmitter bar/sample contact area center and surface element stresses are also very similar to each other at this velocity, while the maximum stress, 6 MPa, is higher than at 1 m s^{-1}. The transmitted gage stress is also comparable with the incident and transmitter bar/sample contact stresses.
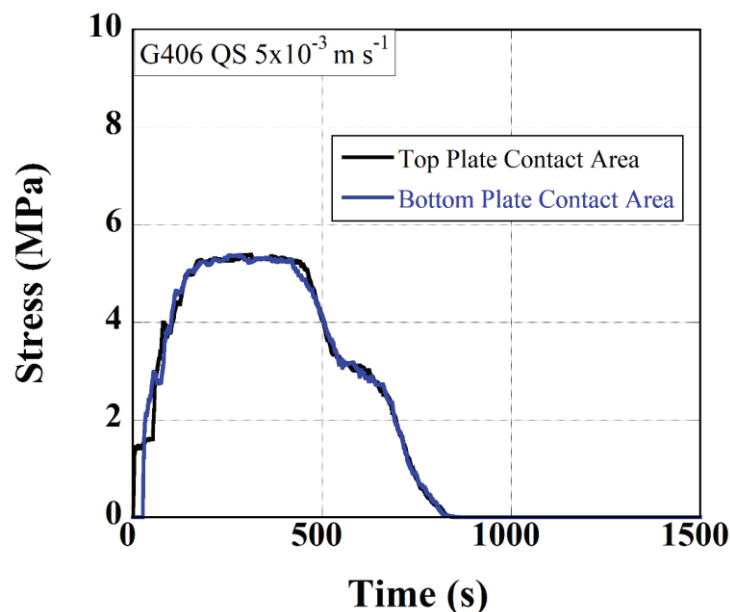
Figure 4.22. The stress-time curves of G406 in quasi-static test model at 5x10^{-3} m s^{-1}
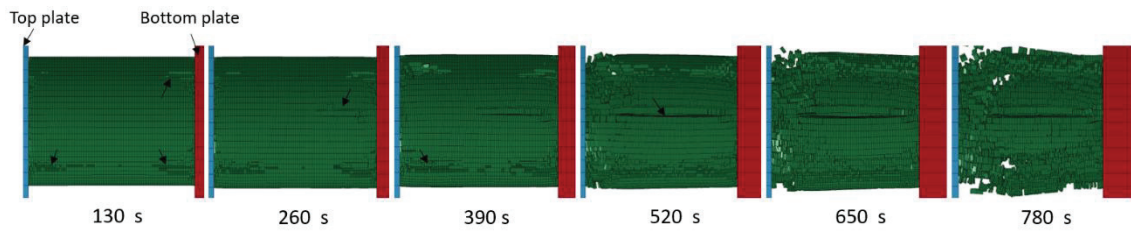
Figure 4.23. The deformation pictures of the quasi-static test numerical model at 5×10^{-3} m s^{-1} at different times

(a)
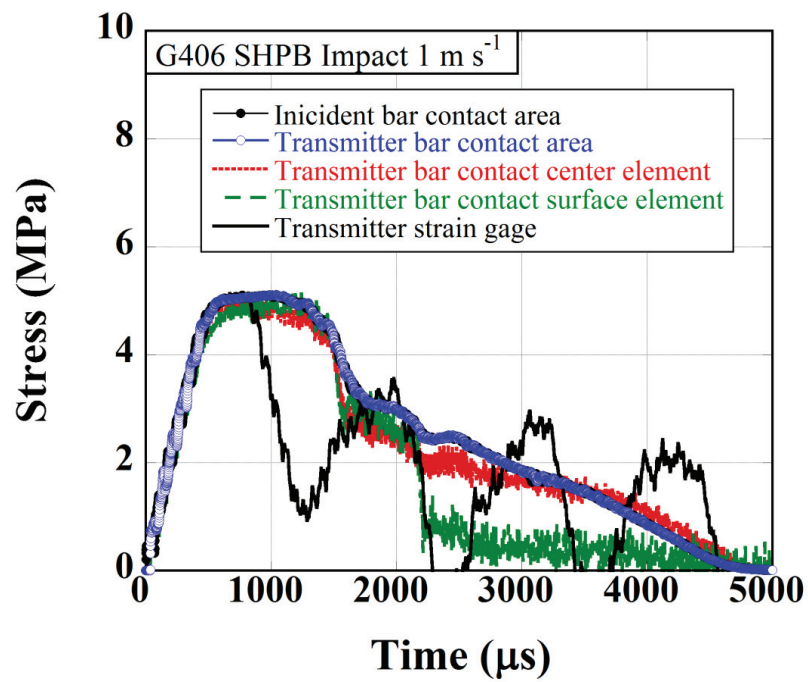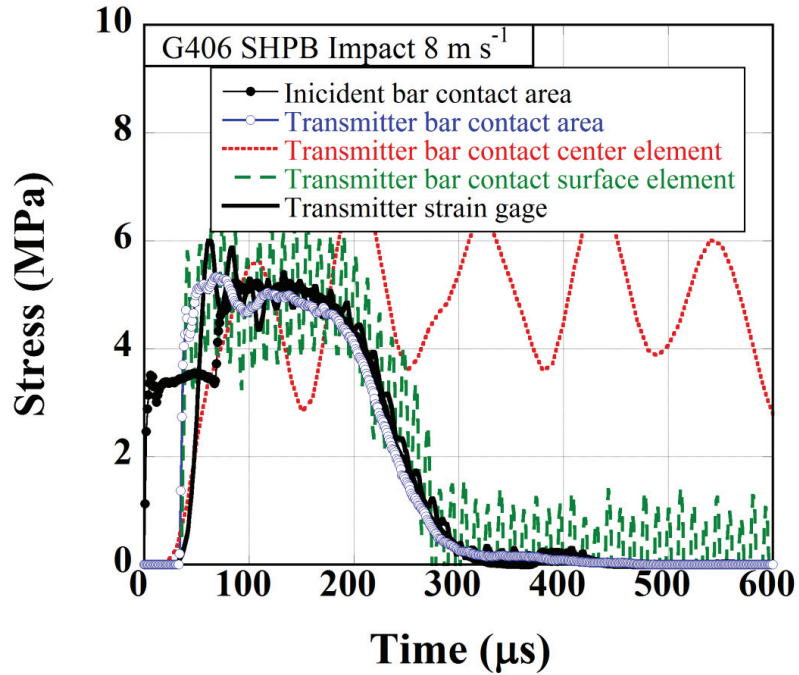
(b)

Figure 4.24. The stress-time curves of G406 sample in SHPB test model at (a) 1 and
(b) 8 m s^{-1}

Figures 4.25(a-b) show the numerical deformation pictures of SHPB tests at 1 and 8 m s^{-1}, respectively. An axial crack initiates at the incident bar contact area at 750 μs at 1 s^{-1} as marked by an arrow in Figure 4.25(a). Additional axial cracks form at the incident contact area at increasing deformation times between 3000 and 4750 μs. These axial cracks reach the transmitted bar resulting in separation of large pieces. At 8 m s^{-1}, axial cracks initiate and progress at both the transmitter and incident bar interfaces and lead to the axial separation of the sample. This numerical fracture mode at 8 m s^{-1} is similar to the experimental fracture mode shown in Figure 4.11(a).

(a)

(cont. on next page)

(b)
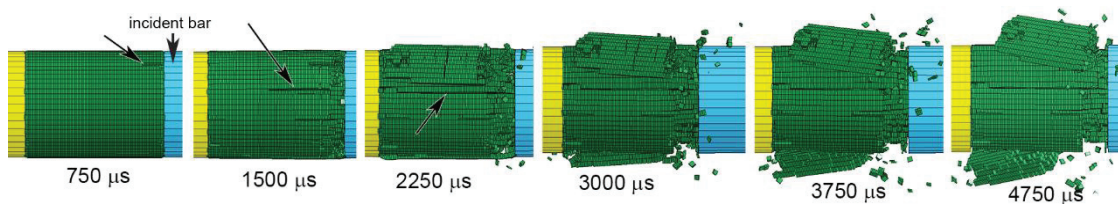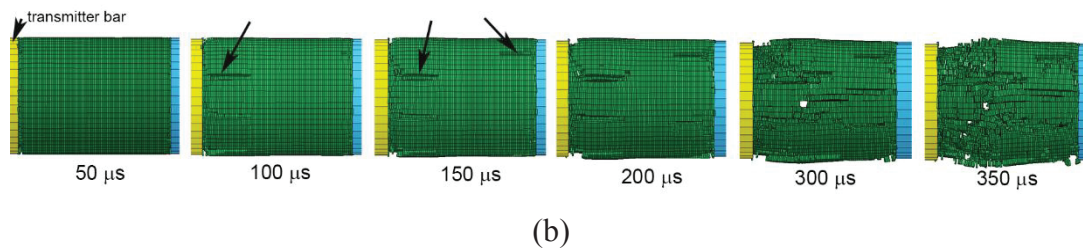
Figure 4.25. The deformation pictures of the SHPB test numerical model at (a) 1 and (b) 8 m s^{-1}

4.2.3. SHPB Direct Impact Test Models

Figures 4.26(a-e) show the direct impact test numerical model stresses at the striker bar/sample contact area, incident bar/sample contact area, incident bar/sample contact area center and surface elements and the incident bar gage location at 10, 20, 30, 60 and 108 m s^{-1}, respectively. As the velocity of striker bar increases, the difference between striker and incident bar/sample contact stresses increase as seen in Figures 4.26(a-e), showing the effect of axial inertia. The maximum striker bar/sample contact stresses are sequentially 5.05, 6.6, 11.11, 20.36 and 35.6 MPa at 10, 20, 30, 60 and 108 m s^{-1}, respectively. The maximum incident bar/sample contact stress is sequentially 5.44, 6.17, 7.35, 7.57 and 7.64 MPa at 10, 20, 30, 60 and 108 m s^{-1}. After 30 m s^{-1}, there is a slight increase in the maximum incident bar/sample contact stress. The maximum incident bar contact center element stress is sequentially 6.63, 7.73, 8.35, 8.75 and 8.94 MPa at 10, 20, 30, 60 and 108 m s^{-1}. These values are 5.55, 6.56, 9.75, 10 and 10.11 MPa for the incident bar contact surface element stresses and 6.11, 7.2, 8.64, 8.82 and 9.05 for incident bar gage stresses sequentially at 10, 20, 30, 60 and 108 m s^{-1}. At and above 30 m s^{-1}, the surface element stress exceeds the center element stress, showing a more stressed region near the surface of the sample. The incident gage stress falls somewhat between center and surface element stresses.

(a)

(b)

(cont. on next page)

(c)
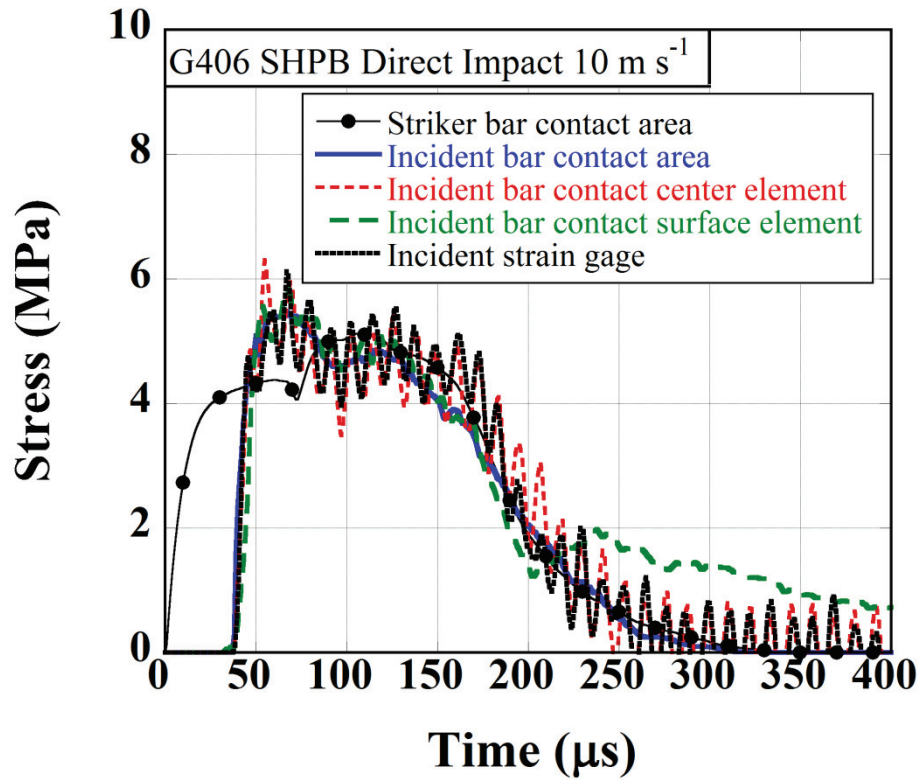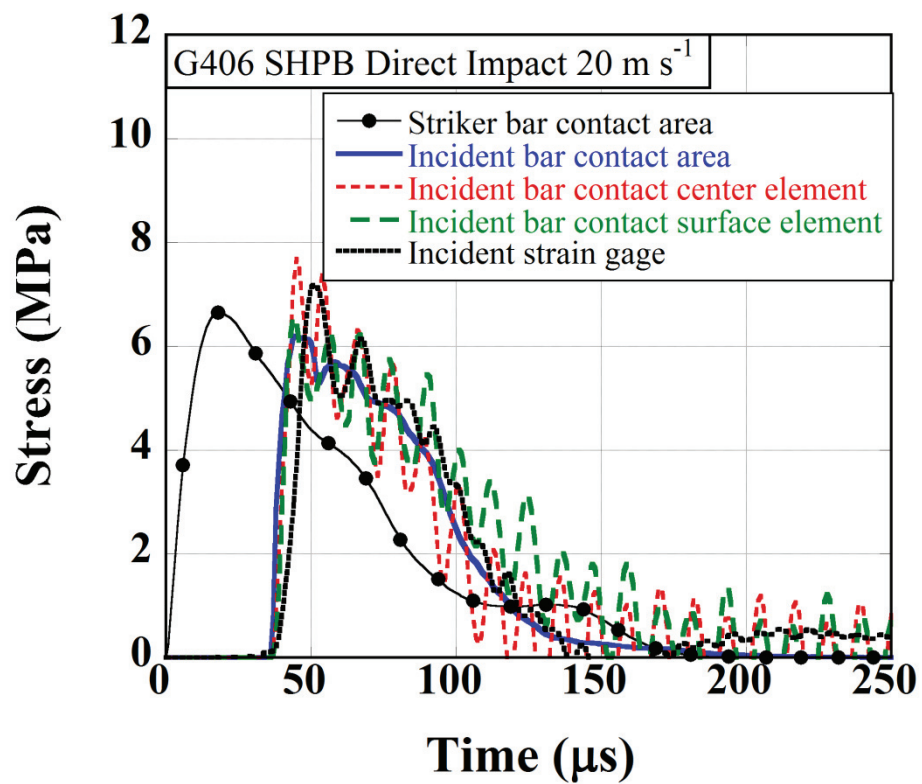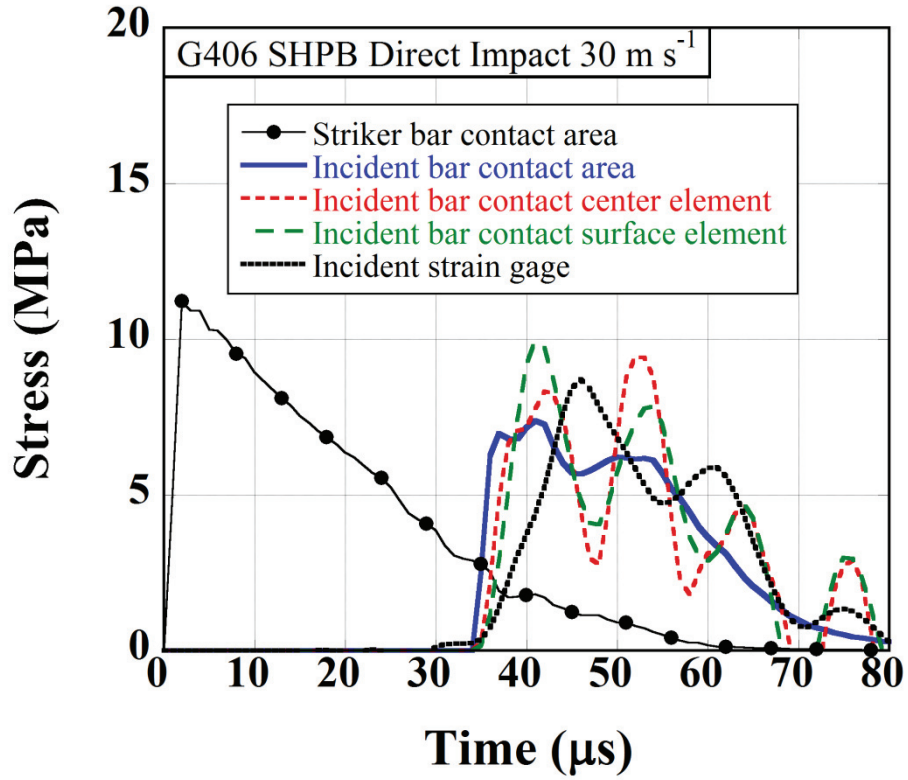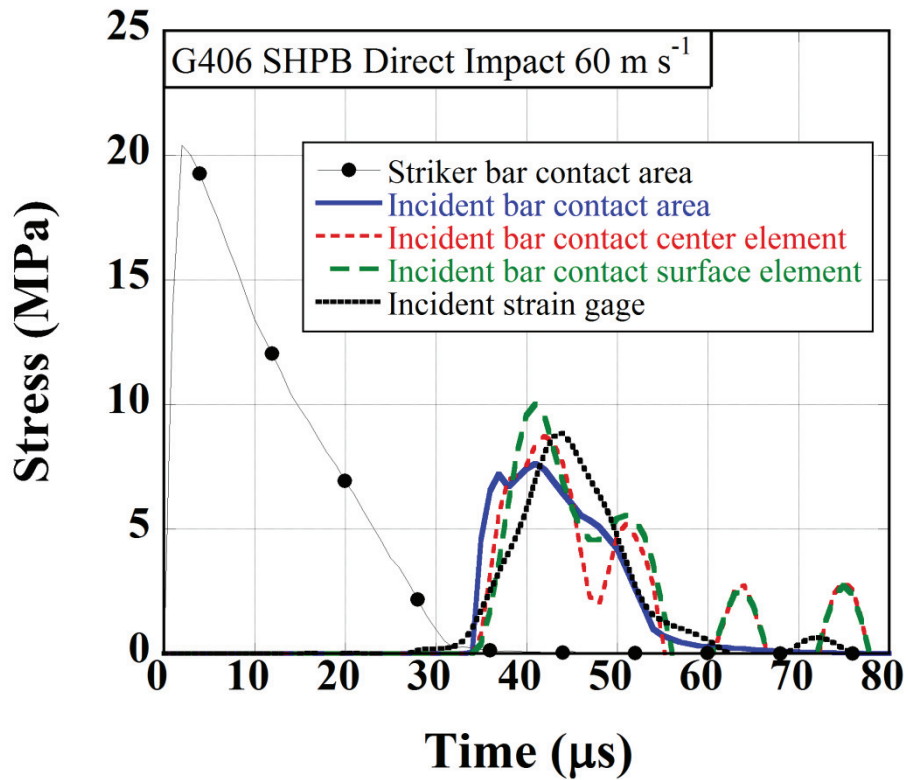
(d)

(cont. on next page)
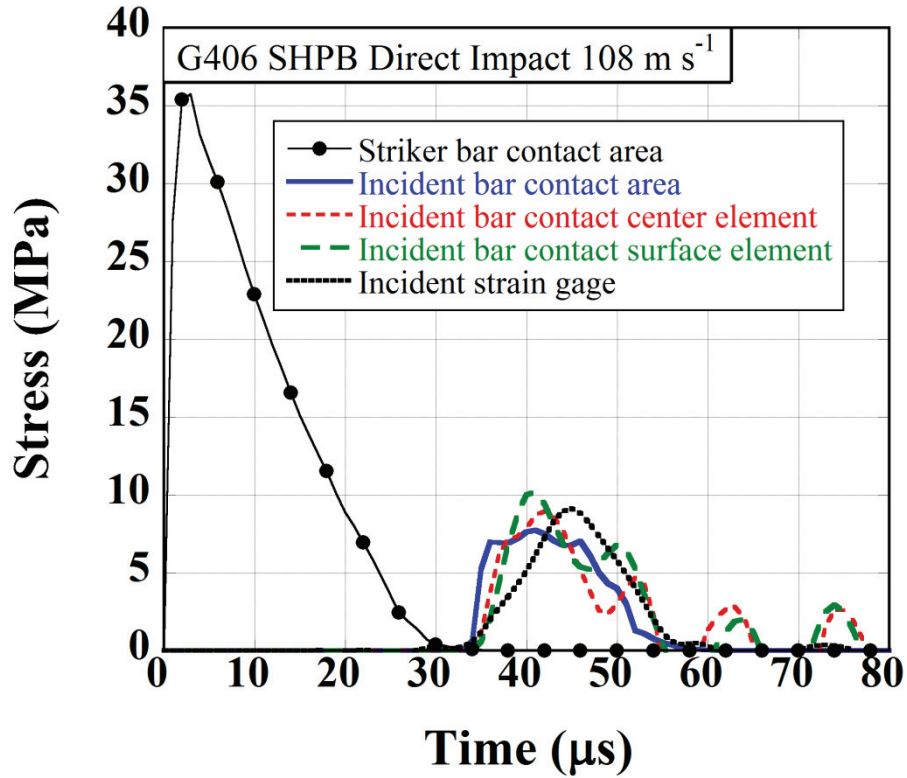
(e)

Figure 4.26. The stress-time curves of G406 in SHPB test model at (a) 10, (b) 20, (c) 30, (d) 60 and (e) 108 m s^{-1}

Figures 4.27(a-e) show the numerical deformation pictures of direct impact tests at 10, 20, 30, 60 and 108 m s^{-1}, respectively. At 10 m s^{-1}, axial cracks form at the incident bar contact area and proceed to the striker bar contact area as seen in Figure 4.27(a). At 240 □s, the sample is almost separated in two parts. A similar fracture behavior is also seen at 20 m s^{-1}, but at this velocity the axial cracks initiate and proceed at both striker and incident bar contact area as seen in Figure 4.27(b). The failure at 30 m s^{-1} and above, however, is different as seen in Figure 4.27(c-e). The sample radially expands at the striker bar contact area at 10 μs as shown by the arrows in Figures 4.27(d-e). The radial expansion results in cracking near the striker bar contact area. Finally, the sample is radially separated into two pieces near the striker bar contact area. The radial expansion and radial separation are also seen experimentally tested samples at 30 and 108 m s^{-1} as shown in Figures 4.11(c-d).
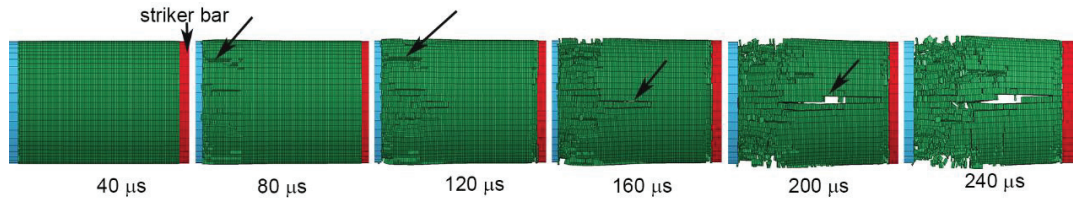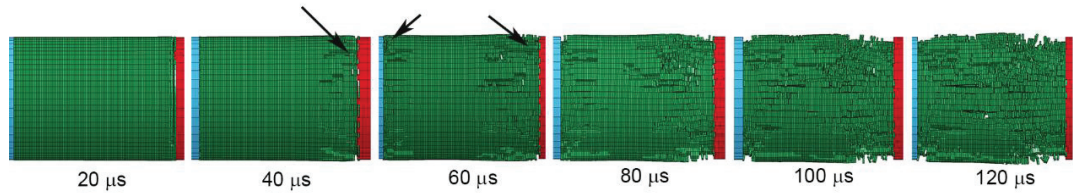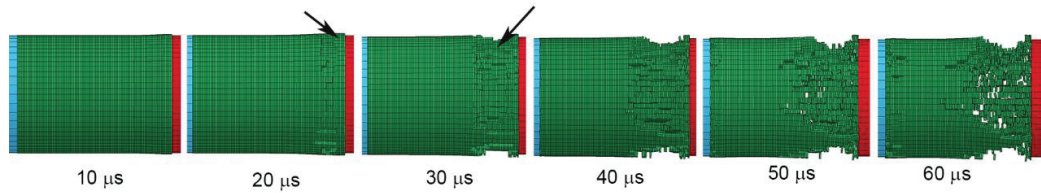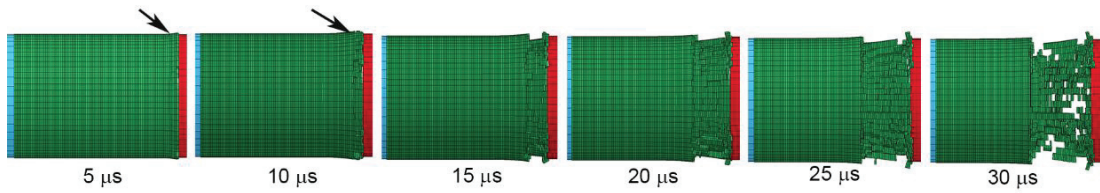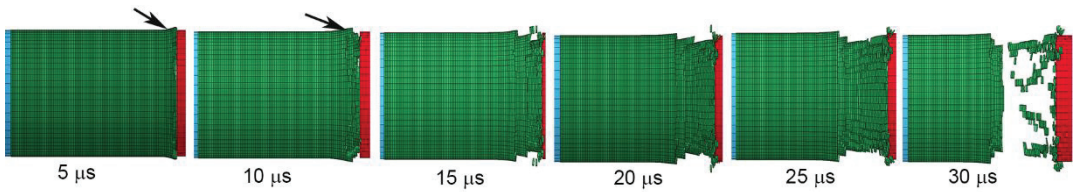
Figure 4.27. The deformation pictures of the SHPB direct impact numerical test at (a) 10, (b) 20, (c) 30, (d) 60 and (e)108 m s^{-1} at different times

CHAPTER 5

DISCUSSION

5.1. Strain Rate Dependent Fracture Strength of Concrete and Rock Like Brittle Materials

The effect of strain rate on the strength of concrete [54] and rock materials [55] is generally expressed by a Dynamic Increase Factor (DIF), which is given as σ_d/σ_s, where σ_d and σ_s are the dynamic and quasi-static static strength, respectively. The dynamic compressive strength and the DIF of compressive strength of concrete and rock materials enhance with increasing strain rate as shown Figures 5.1(a) and (b). As noted in the same figures, a rapid rise of the compression strength occurs after about a critical strain rate, above ~10-100 s^{-1}. The International Federation for Structural Concrete (CEB) recommendation of the critical strain rate, which the DIF values increase rapidly, is ~30 s^{-1}. Two empirical equations were proposed by the CEB to define the DIF values of concrete as [56]

$$DIF = \frac{\sigma_d}{\sigma_s} = \left(\frac{\dot{\varepsilon}_d}{\dot{\varepsilon}_s}\right)^{1.026\alpha} \qquad \dot{\varepsilon}_d \leq 30 \ s^{-1}$$

(5.1)

$$DIF = \frac{\sigma_d}{\sigma_s} = \gamma\dot{\varepsilon}_d^{1/3} \qquad \dot{\varepsilon}_d > 30 \ s^{-1}$$

(5.2)

where, $\dot{\varepsilon}_d$ and $\dot{\varepsilon}_s$ are the dynamic and static strain rates, respectively. The value of $\dot{\varepsilon}_s$ is 3×10^{-5} s^{-1}, $\gamma = 10^{6.156\alpha-2}$ and $\alpha = \frac{1}{(5+\frac{\sigma_s}{10})}$. The fitting of the compressive strength data shown in Figure 5.1(a) with Equations 5.1 and 5.2 resulted in a critical strain rate of 30

s^{-1} as shown in Figure 5.1(c) [54]. A similar increase in the DIF of rock materials is also shown in Figure 5.1(b) between 10 and 100 s^{-1}. The strain rate dependent strength of concrete like materials is ascribed to 1) strain-rate dependent growth of tensile micro cracks (thermally activated mechanism), 2) viscous behavior of bulk material between cracks (Stefan effect) and 3) the inertial effects [54-55, 57]. It was argued that viscous effect is dominant at strain rates below 1 s^{-1}, while inertial effects become predominant at strain rates higher than 10 s^{-1} [58]. The ranges of above three mechanisms are also presented in Figure 5.1(d) taken from the reference [57]. Region 1 of Figure 5.1(d) is the thermally activated mechanism, Region 2 is viscous mechanism and Region 3 is inertial mechanism.

(a)   (b)

(c)   (d)
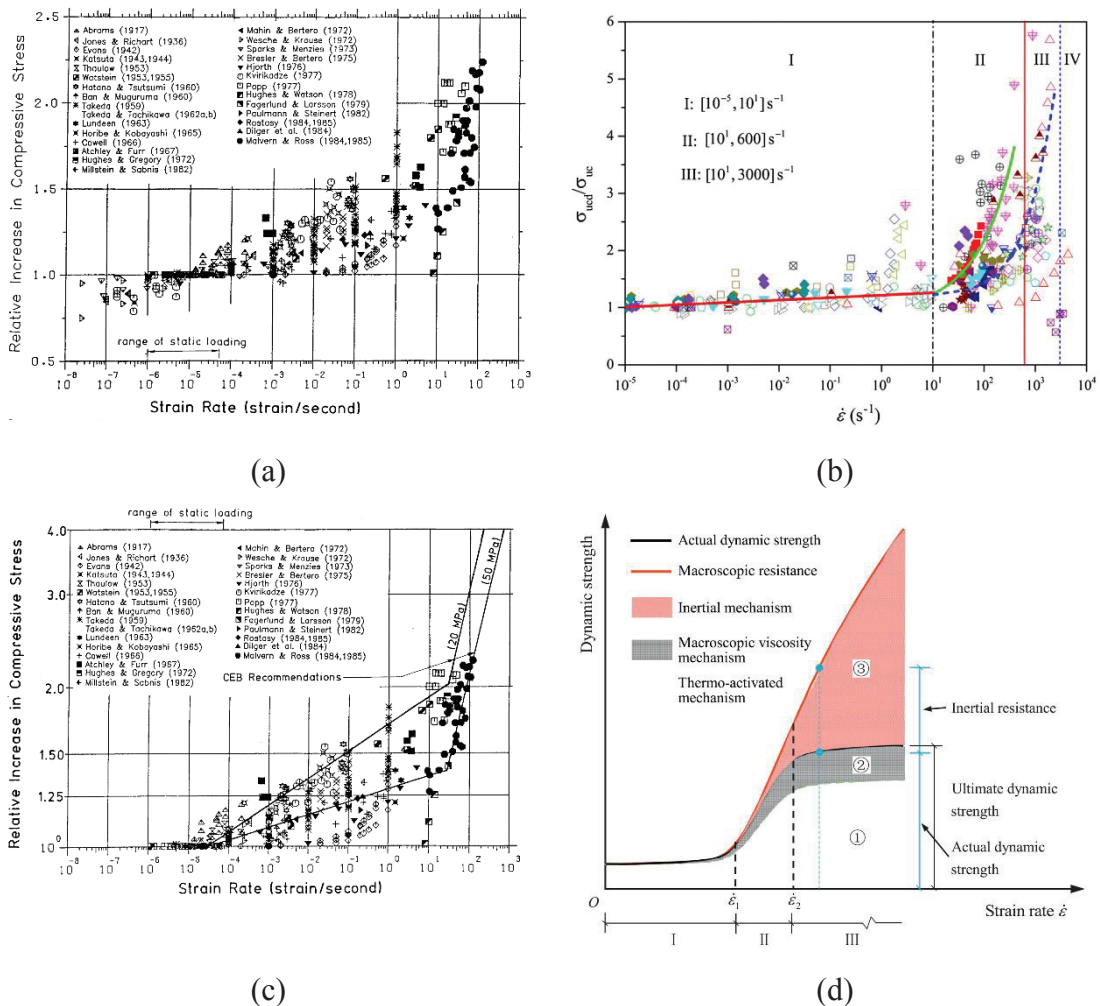
Figure 5.1. The variation of compressive strength of (a) concrete [54] and (b) rocks as function strain rate [55] and (c) the application of the CEB equations to the compressive strength of concrete in (b) [54] and (d) schematic presentation of the dependence of compressive strength on strain rate [57]

The facture of brittle materials proceeds with crack opening and growth. At quasi-static strain rates, the energy needed for crack opening is much higher than the energy needed for crack growth. Therefore, few cracks grow under static loading through the weakest path along axial direction. At increasing strain rates, there is however less time for both crack opening and growth. This causes an increase in the strength and number of micro cracks formed. The micro cracks are also not necessarily oriented through axial direction. Several studies have shown the increased number of cracks of concrete at increasing strain rates under compression [54]. The fracture mechanism considered here is thermally activated, since increasing strain rate and decreasing temperature increase the fracture strength of concrete [55, 57, 59]. The thermally activated stress is given as [59]

$$\sigma_d = \frac{U_o}{v} + \sigma_o + \frac{RT}{v} \ln \left(\frac{\dot{\varepsilon}_d}{\dot{\varepsilon}_s} \right)$$

(5.3)

where $\frac{U_o}{v} + \sigma_o$ is the limiting stress when T=0 K or $\dot{\varepsilon}_d = \dot{\varepsilon}_s$. Equation 5.3 shows that the fracture stress increases linearly with decreasing temperature and increasing logarithm of strain rate.

Viscous mechanism is explained as follows. The thin viscous liquid such as water or oil between two plates exerts a return force (F) when the plates are separated with a velocity. This is known as Stefan effect and the exerted force is given by the following equation

$$F = \frac{3\eta V^2}{2\pi h^5} \dot{h}$$

(5.4)

where η is the viscosity of liquid, V is the volume of liquid, h is the initial distance between plates and $\dot{h}$ is the separation velocity of plates. The separation velocity depends on strain rate; therefore, increasing both strain rate and volume increase the force exerted by liquid. The water content of concrete has shown to increase the strain rate sensitivity in tension [60] and compression [61]. The water content also altered

compression failure mode [61]. The increased strain rate sensitivity of wet concrete was ascribed to the viscous mechanism in several studies [58, 61-62].

Inertial effects, both axial and radial, were reported to be effective after 10 s^{-1} [54]. The inertia-corrected stress of a cylindrical sample under compression is given as [63]

$$\sigma_c = \sigma_A + \left[\left(\frac{h^2}{3}\right) - v^2 \left(\frac{d^2}{8}\right)\right] \rho \, \ddot{\varepsilon} \, (t)$$

(5.5)

where σ_A is the average stress, h and d are sequentially the height and diameter of the cylindrical sample, ρ and v are the density and Poisson's ratio of the test sample, respectively. The second and third term in Equation 5.5 are the axial and radial inertia stress, respectively. Note that at the constant strain rate, the inertial effects become zero. At increasing strain rates, an elastically deforming structure cannot expand in transverse direction (Poisson's expansion) due to the radial inertia restraint. The radial inertia imposes a confinement stress or lateral stress on the deforming structure and transforms the deformation state from uniaxial stress to uniaxial strain. The increase of the strength of concrete after a critical velocity is ascribed to the transformation of deformation from uniaxial stress to uniaxial strain [64]. The lateral confinement was also shown to increase the fracture strength of concrete [65].

Brace and Jones [64] compared the quasi-static compression uniaxial strain and shock fracture strength of a limestone at different strain rates as depicted in Figure 5.2(a). The strength of limestone increases slowly with strain rate up to 10^3 s^{-1}; thereafter the strength increases sharply, approaching the shock fracture strength. Grady [66] proposed a mechanism for the strain rate dependent fracture strength of brittle materials (Figure 5.2(b)). At low strain rates, the strength shows a low dependence to strain rate mainly controlled by thermally activated subcritical crack growth, which is presented as the quasi-static fracture curve. The transition region of Figure 5.2(b) is proposed to be governed by the non-thermal, inertia dominated fracture which results in rapid rise of fracture strength. At very high strain rates the delay of the fracture due to fast deformation prevents the brittle fracture, leading to a lower strain rate dependence of fracture strength. These also imply that the fracture strength will not increase infinitely with increasing strain rate in the inertia dominated region and an "s-type"

dependence on the strain rate was proposed. On an s-type curve, there are two turning points. The first turning point is from a low strain rate dependent to a higher strain rate dependent strength region and the second is from a high strain rate dependent strength region to again a low strain rate dependent strength region. Yu [67] determined 10^2 and 10^4 s^{-1} as the first and second turning points for concrete, respectively. An SHPB model of concrete using a pressure dependent strength model showed that the stress triaxiality ($\eta = \frac{\sigma_H}{\sigma_e}$; where σ_H and σ_e are the hydrostatic and equivalent stress, respectively) was near 1D stress state ($\eta = -0.33$) at low strain rate, 47 s^{-1}, while it reached 1D strain state ($\eta = -0.66$) at ~795 s^{-1} when $v = 0.2$ [68]. Above this strain rate, the sample deformation is completely 1D strain state as seen in Figure 5.2(c). Furthermore, the critical strain rate for the passage to 1D strain state was shown to depend on the diameter of the sample; larger diameter samples showed larger inertial effects hence lower critical strain rate for completely 1D strain state (Figure 5.2(d)). The pseudo strain rate effect that is the increase of fracture strength when the deformation transforms from 1D stress to 1D strain state occurs when the compressive strength of the tested sample is hydrostatic-pressure-sensitive and lateral confinement is developed on the sample. Moreover, the current concrete models adapted a cut-off value of 2.94 to cap DIF when the strain rate is above 300 s^{-1} [68].

(a)

82

(b)

(c)
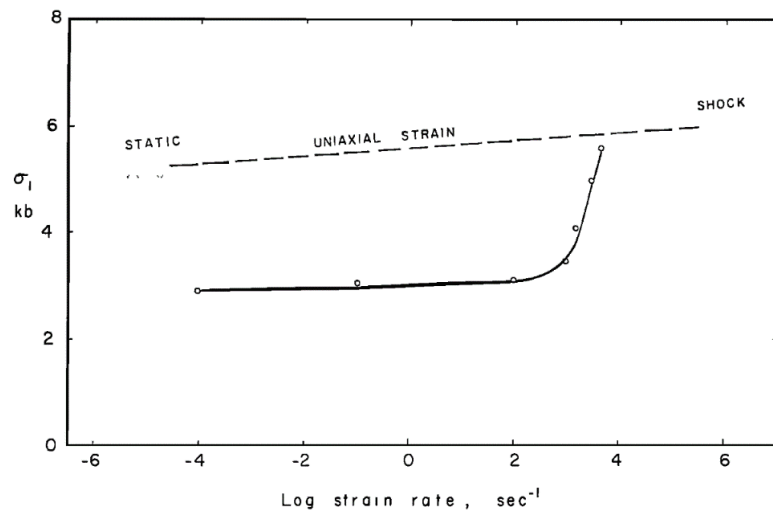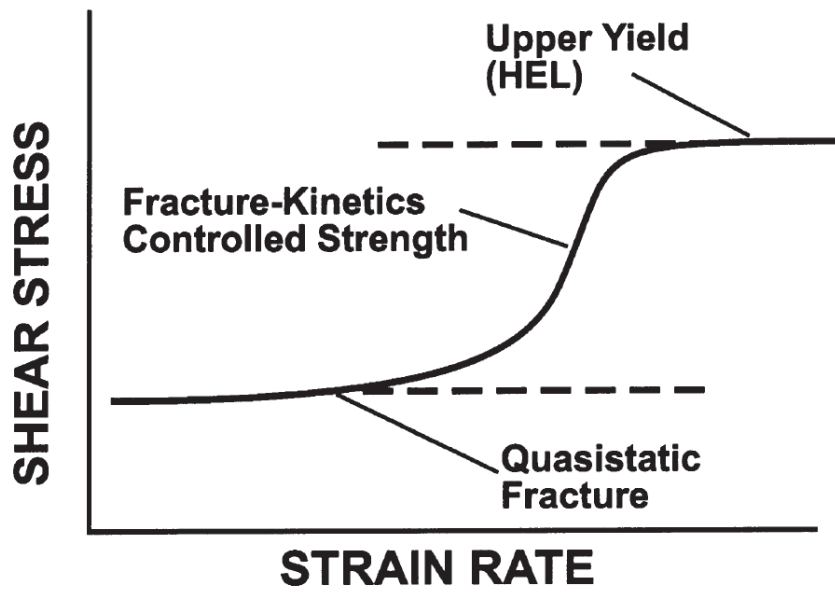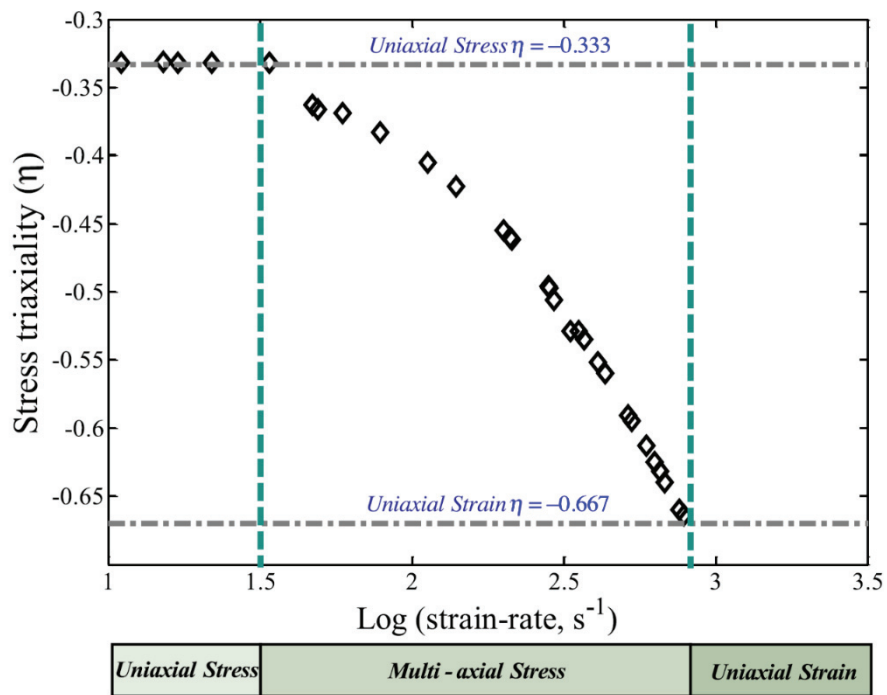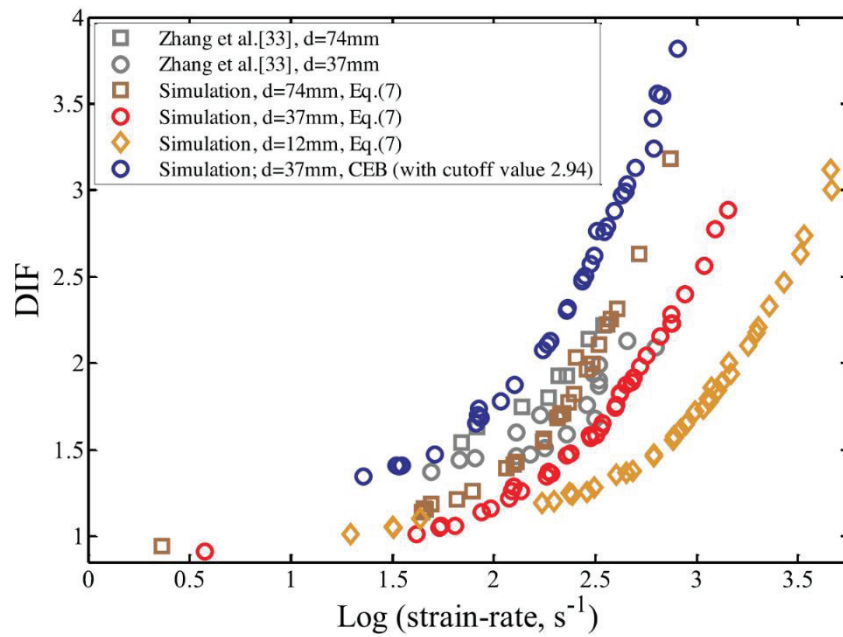
(d)

Figure 5.2. (a) fracture strength versus log strain rate for a limestone for uniaxial strain and uniaxial stress [64], (b) dynamic failure in brittle solids based on fracture-kinetics and mechanism-transition model [66], (c) stress triaxiality versus strain rate and (d) effect of sample diameter on DIF [68]

5.2. Compression Strength Dependence on Strain Rate of Tested AAC Samples

The stress-strain curves of G406 samples from quasi-static to 385 s^{-1} (20 m s^{-1}) are shown in Figure 5.3(a). The fracture strain corresponding to the compressive strength is seen in the same figure almost constant at the strain rates investigated, ~0.015, while the modulus increases with increasing strain rate. At 1158 and 4158 s^{-1}, the slopes of initial linear region are however significantly reduced compared to those of lower strain rates, particularly at 4158 s^{-1}, as seen in Figure 5.3(b). In the direct impact tests, the stress on the sample was measured by the strain gages mounted at a distance on the proximal-end side; therefore, the wave propagation obscured the correct strain measurement of the sample. But, the compressive strength almost remained constant at 4158 s^{-1} (Figure 5.3(b)).

84
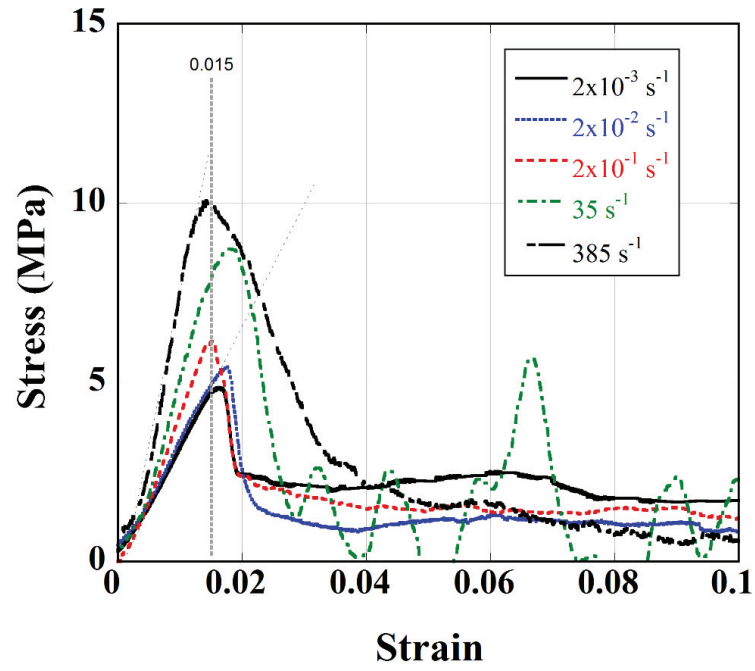
(a)
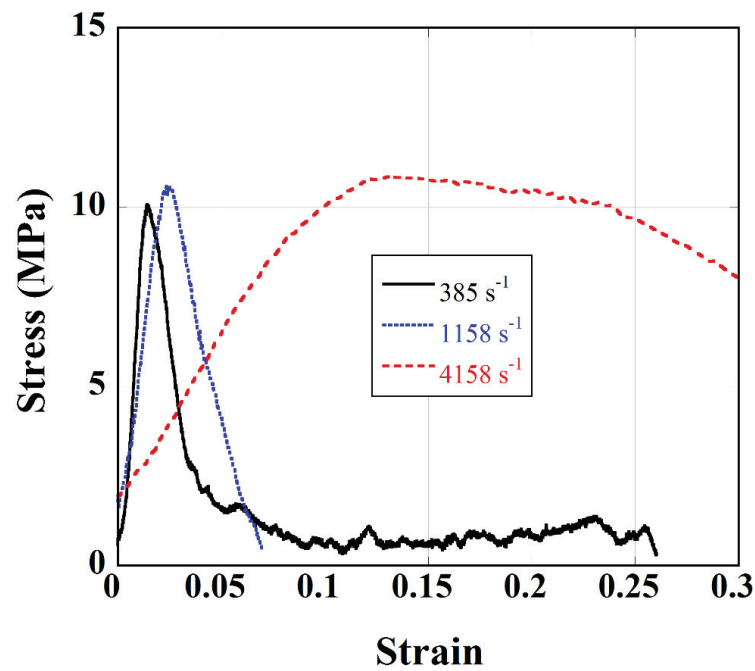
(b)

Figure 5.3. The stress curves of G406 (a) from quasi-static to 385 s^{-1} and (b) from 385 to 4158 s^{-1}

The compressive and mean compressive strengths of G406 samples are shown as function of strain rate in Figure 5.4(a). The compressive strengths between $2x10^{-3}$ and

$2x10^{-1}$ s^{-1} in the same figure are fitted with Equation 5.1, while the compressive strengths between 35 and 1158 s^{-1} with Equation 5.2. The compressive strengths at the highest strain rate, 4158 s^{-1}, are almost the same as the compressive strengths at 1158 s^{-1}; therefore, it was not fitted. Figure 5.4(a) shows the DIF and mean DIF with the fitted parameters of Equations 5.1 and 5.2. The value of α in Equation 5.1 and γ in Equation 5.2 are 0.028 and 0.304 after the fitting, respectively. The critical velocity for the increased compressive strength is 125 s^{-1} as shown by a circle in Figure 5.4(a). The dynamic compressive strength is also fitted with $\frac{\sigma_d}{\sigma_s} = \gamma \dot{\varepsilon}_d{}^n$. The value of is 1.33 and the value of γ is 0.092. The power-law equation results in a critical strain rate of 1 s^{-1}. It is found that the power equation is better fitted with both compressive strength and the DIF than Equation 5.2 proposed by the CEB. A cut-off DIF of 2.55 above ~1000 s^{-1} corresponding to a compressive strength of ~11.5 MPa is shown in Figures 5.4(a) and (b). The determined cut-off DIF is lower than that proposed by the CEB, 2.94, while the strain rate after which the compressive strength is almost constant is agreed well with the CEB, above 300 s^{-1}. It was previously shown numerically that the critical strain rate for the passage from the uniaxial state of stress to the uniaxial state of strain is a function of sample size: at smaller sample sizes, both the transformation strain rate and the strain rate corresponding to cut-off value increase [68]. In the present study relatively small samples have tested, 19 mm in diameter and 26 mm in length. The transformation strain rate from the uniaxial state of stress to the uniaxial state of strain is found in the present study between 1 and 125 s^{-1}.

Figure 5.5 shows the variation of the compressive strain corresponding to the compressive strength together with the mean values of the compressive strain as function of strain rate. A linear-fit to the compressive strain from quasi-static to 385 s^{-1} gives an average compressive strain of 0.017. The compressive strains determined in the drop-weight tests are slightly higher than those in the quasi-static and direct impact tests as shown in the same figure. In the drop weight tests, the displacement was measured by the displacement of the indenter at the impact side.
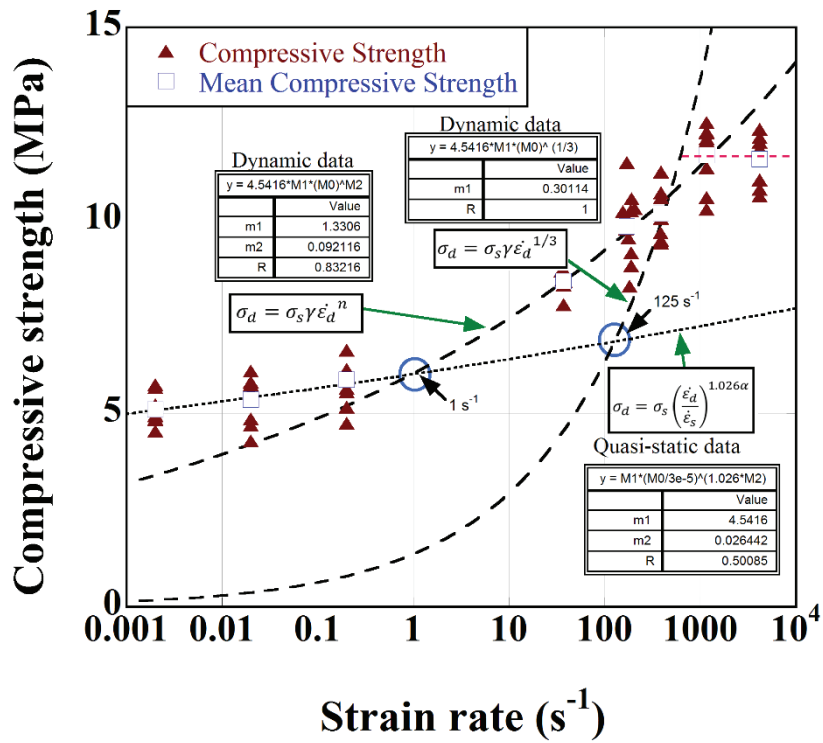
(a)
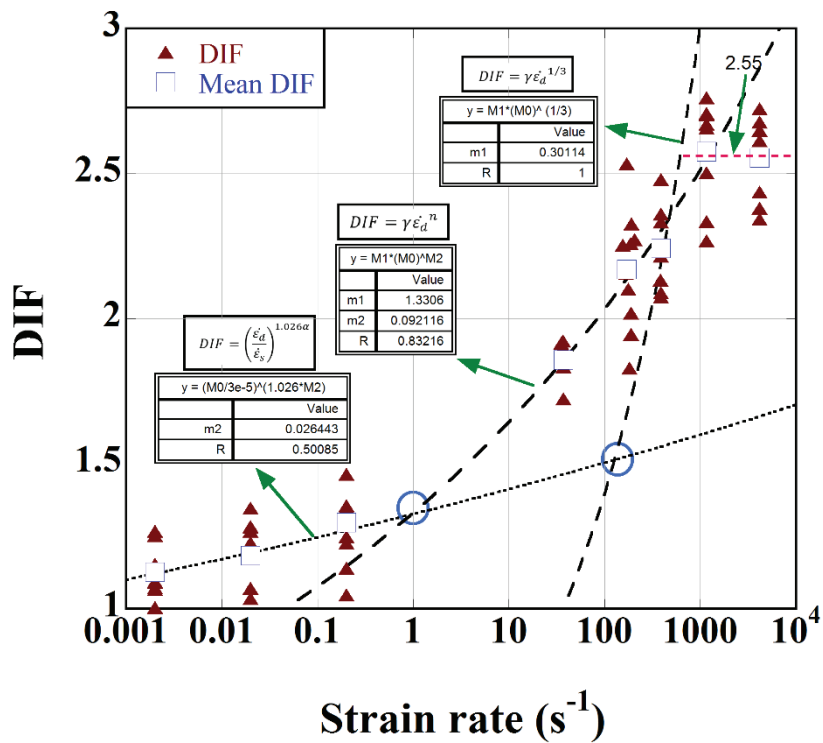
(b)

Figure 5.4. The variation of (a) the compressive strength and (b) DIF with strain rate
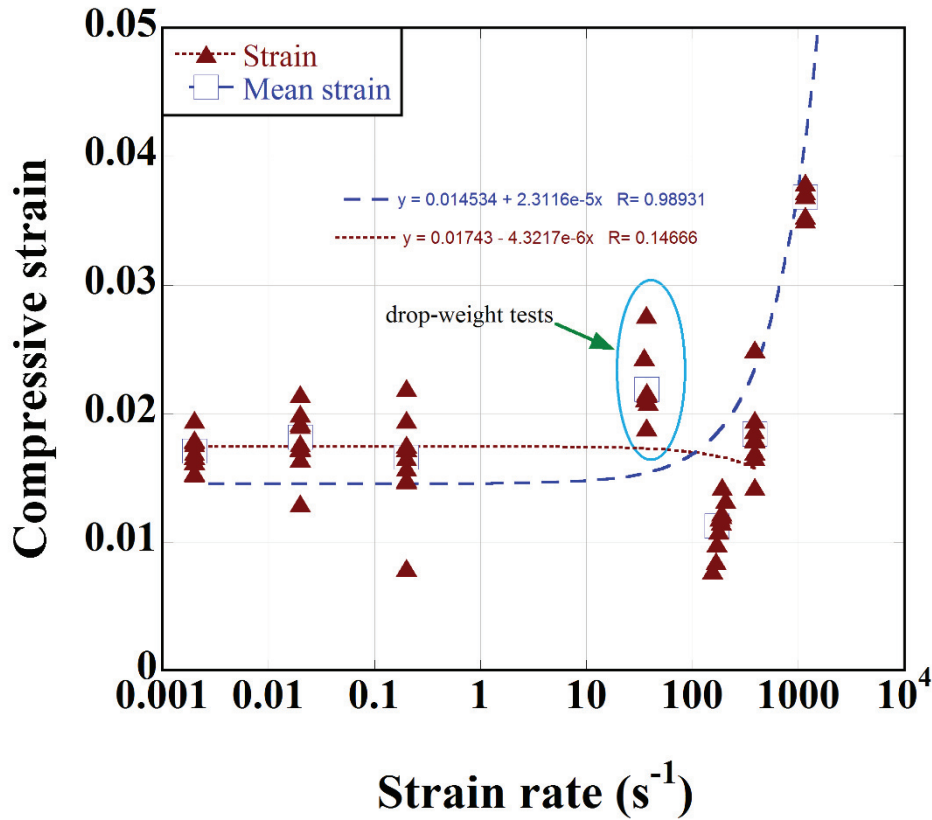
Figure 5.5. The variation of the compressive strain with strain rate

Figure 5.6 shows the compressive strength values together with the confined test compressive strength values as function of strain rate. Fitting Equation 5.1 to the confined tests compressive strength values gives an α value of 0.022 which is very near to the value of α obtained from the unconfined tests compressive strengths at quasi-static strain rates as depicted in Figure 5.6. A large variation in the compressive strengths of the confined tests makes it however difficult to make a solid conclusion. A full confinement would provide a uniaxial state of strain in the sample. However, one of the problems in these tests is the difficulty in establishing a full-confinement state as the material near the confinement-circular-steel-tube may fracture easily, resulting in reduced pressure on the sample and hence invalidating a full-confinement state. Second problem is the prevention of the friction forces between the sample and confinement-circular-steel-tube.
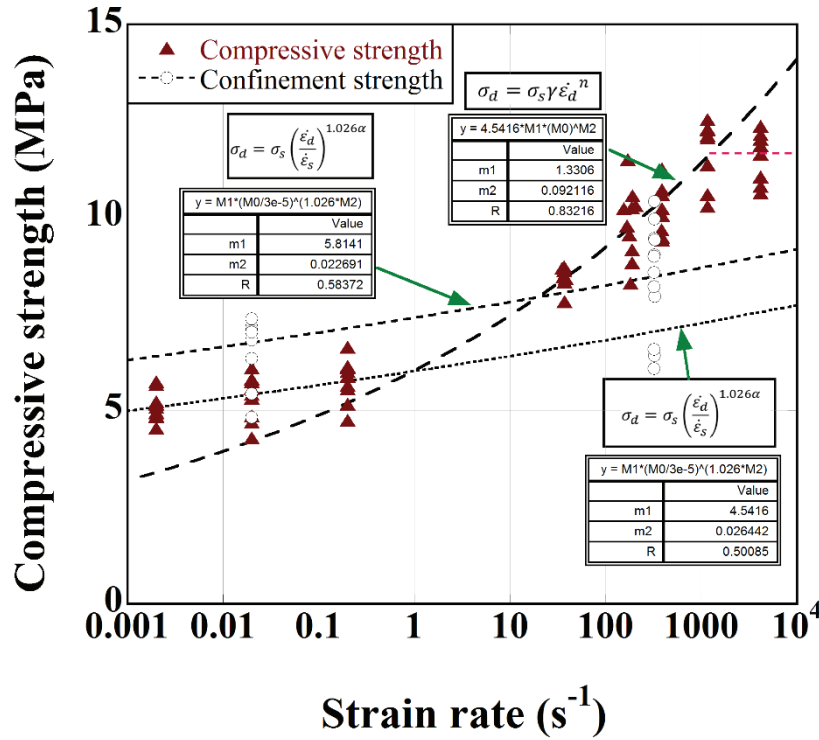
Figure 5.6. The variation of the compressive and confinement test strength with strain rate

Figures 5.7(a-b) show the indentation strength as function of indenter size at the three different quasi-static strain rates, respectively. The indentation strength was calculated by dividing the indentation force by the cross-sectional area of the indenter. Therefore, the shear and frictional forces were not taken into account in the stress calculations. As noted in the same figures, the indentation strength does not change after 25 mm indenter size in G406 samples and after 20 mm indenter size in MP samples. This means that the compression force applied by the indenter is significantly higher than the shear and friction forces. The constant indentation stress is therefore taken as the indentation strength. The indentation strength of G406 and MP samples are sequentially 4 and 0.35 MPa higher than the quasi-static unconfined compressive strength. The indentation strength is nearly twice the compressive strength.
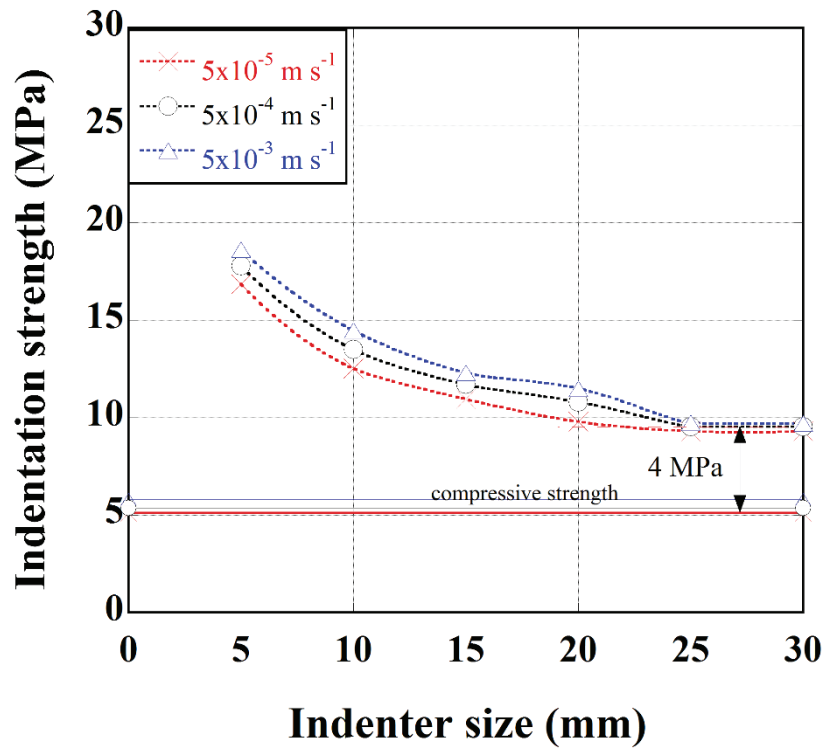
(a)
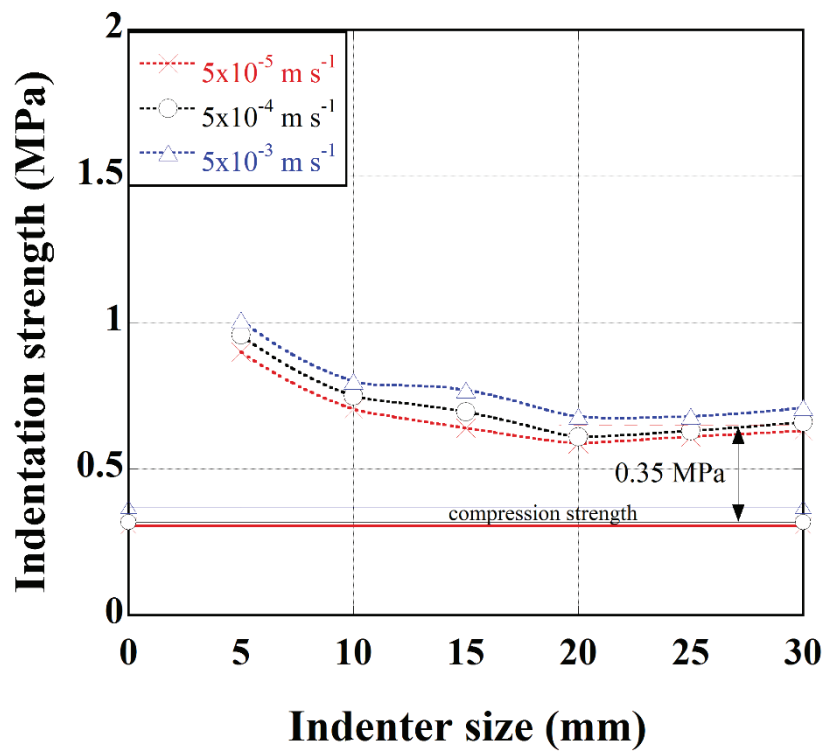
(b)

Figure 5.7. Indentation strength vs indenter size (a) G406 and (b) MP samples

Figures 5.8(a-b) show the variation of indentation strength of G406 and MP samples as function of velocity. In the same figures, the compressive strength values are also shown for comparison. Equation 5.1 is modified by replacing the strain rate with velocity and by taking a reference velocity 1×10^{-5} m s^{-1}. The modified Equation 5.1 is then fitted to the quasi-static indentation strength values of 20 and 30 mm indenter for G406 and 25 and 30 mm indenter of MP samples. The results are shown for G406 in Figure 5.8(a). The fitting results in the indentation compression strengths matching with the unconfined compressive strengths at high strain rates, ~1000 s^{-1}. This result confirms that the indention strength after a critical indentation size forms a full-confinement state corresponding to the state of uniaxial strain. Figure 5.8 shows that the compressive strength predicted by fitting the indentation strength (25 and 30 mm diameter indenters) to modified Equation 5.1 is 0.8 and 0.9 MPa between 10 and 100 m s^{-1}, corresponding to the strain rates of ~400 and 1200 s^{-1}.

(a)
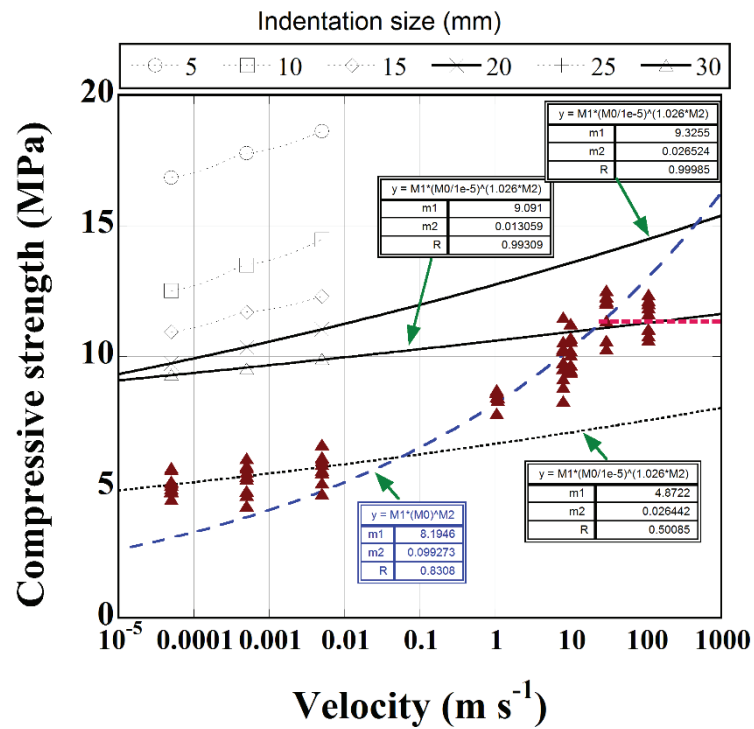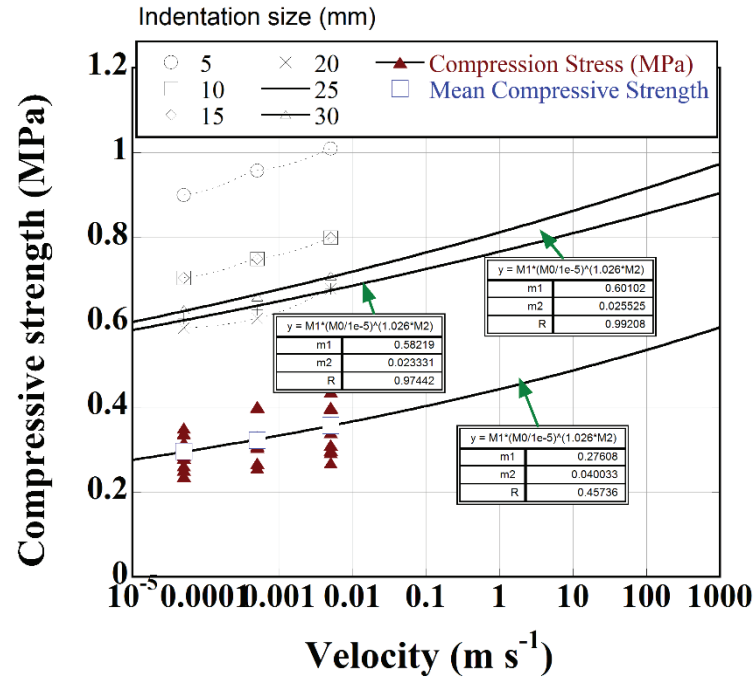
Figure 5.8. Compressive strength and indentation strength vs log velocity (a) G406 and (b) MP

Based on above results, three different deformation mechanisms of the tested light weight concrete are proposed and shown in Figure 5.9. The first region in which the first equation of the CEB (Equation 5.1) applicable is a low-strain-rate-dependent DIF region, the second region in which a power-law strain rate hardening is applicable is the high-strain-rate-dependent DIF region and the last region is the cut-off.

The model distal-end and impact-end contact stress-strain curves are shown as function of velocity in Figures 5.10(a) and (b), respectively. The sample strain in the graphs of Figures 5.10(a) and (b) was determined numerically by the difference in the displacement of the distal and impact end. The distal-end contact compressive strengths are almost constant between static velocity and 10 m s^{-1}; increase when the velocity increases to 20 and 30 m s^{-1} and remains almost constant at 30, 60 and 108 m s^{-1}. This is in accord with the experimental compressive strength values. The impact-end contact stresses are again almost constant until about 10 m s^{-1}; thereafter increases with increasing strain rate. Both the model radial and axial inertia therefore start at about 10 m s^{-1} and the stress increases with increasing velocity, while the sample fails at a constant strength after about 30 m s^{-1} corresponding to a stress of ~7.55 MPa.
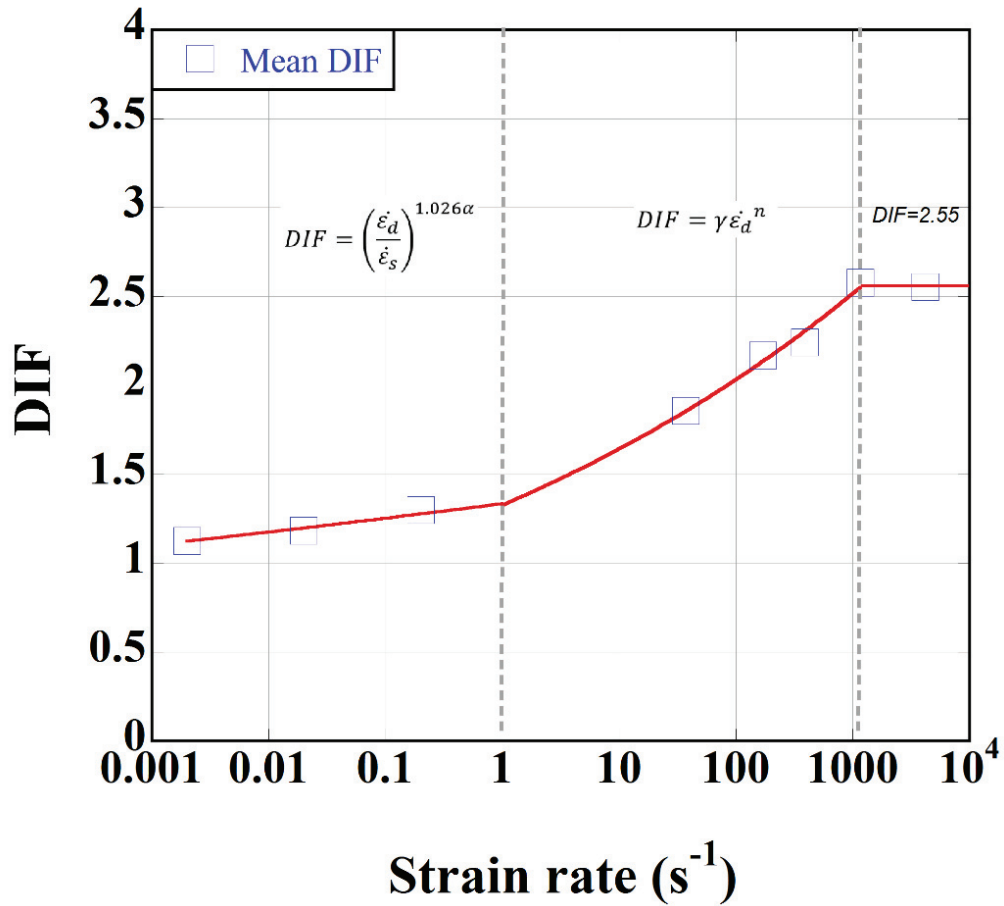
Figure 5.9. Mean DIF vs strain rate and three distinct region of deformation mechanisms

The distal-end center and surface element and gage element stress-strain curves are shown sequentially in Figures 5.11(a-c). Because of higher pressure development at the surface, the surface element failure occurs at a higher stress (~10MPa) than the center element (~8.8 MPa) as depicted in the same figures. Note that again the failure strengths are the same for both center and surface elements at 30, 60 and 108 m s^{-1}. The compressive strengths obtained from the gage element are also the same for these three velocities, while the magnitudes are similar with those of contact center element.
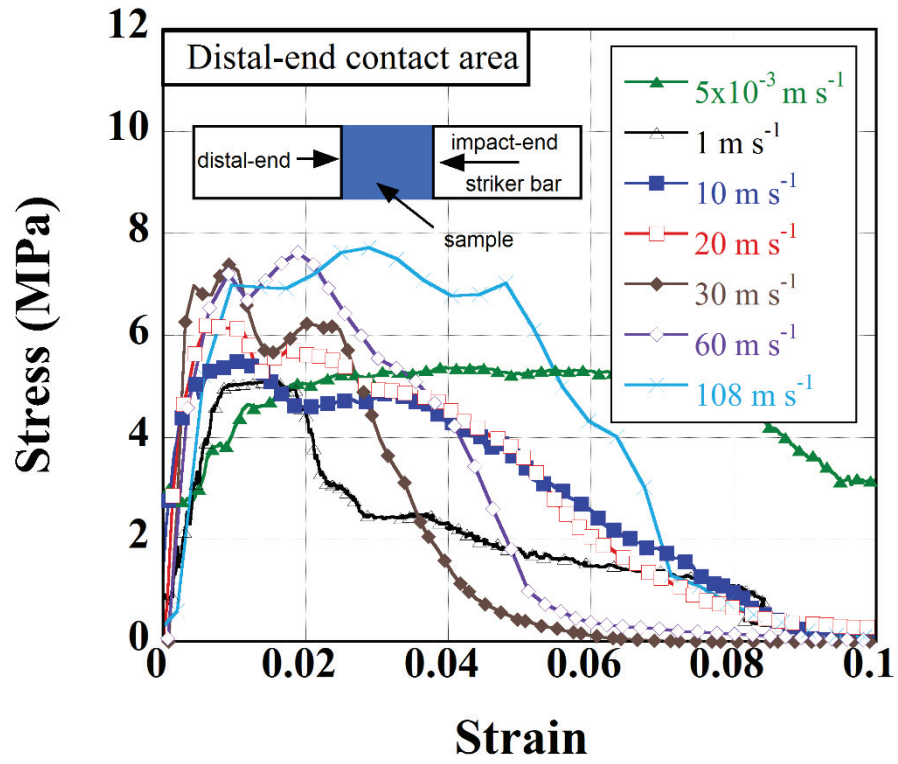
(a)
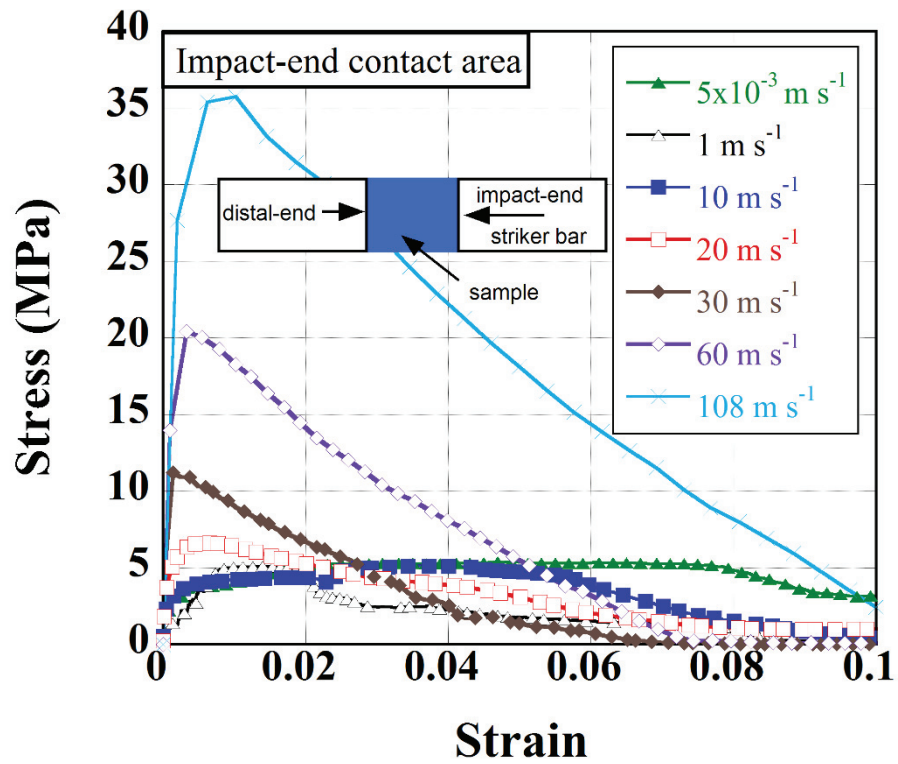
(b)

Figure 5.10. The stress-strain (nominal) curves of the models at different velocities (a) distal-end bar contact area and (b) impact-end bar contact area

(a)

(b)
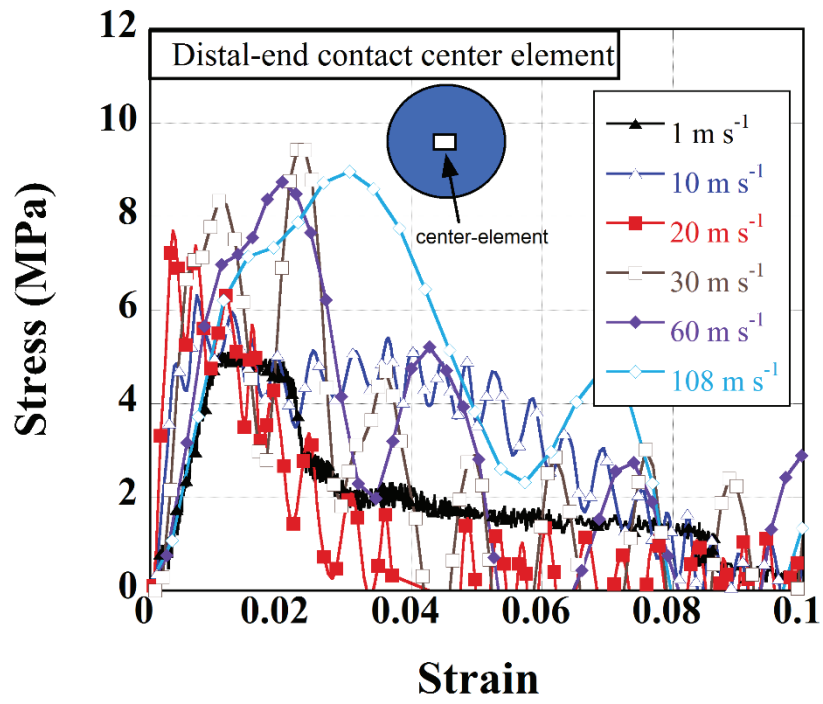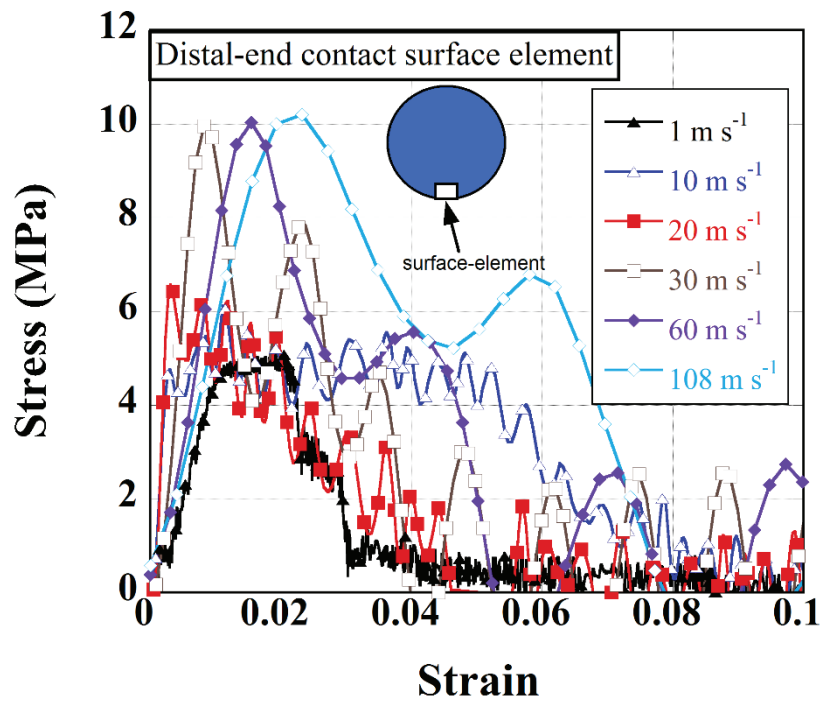
(cont. on next page)
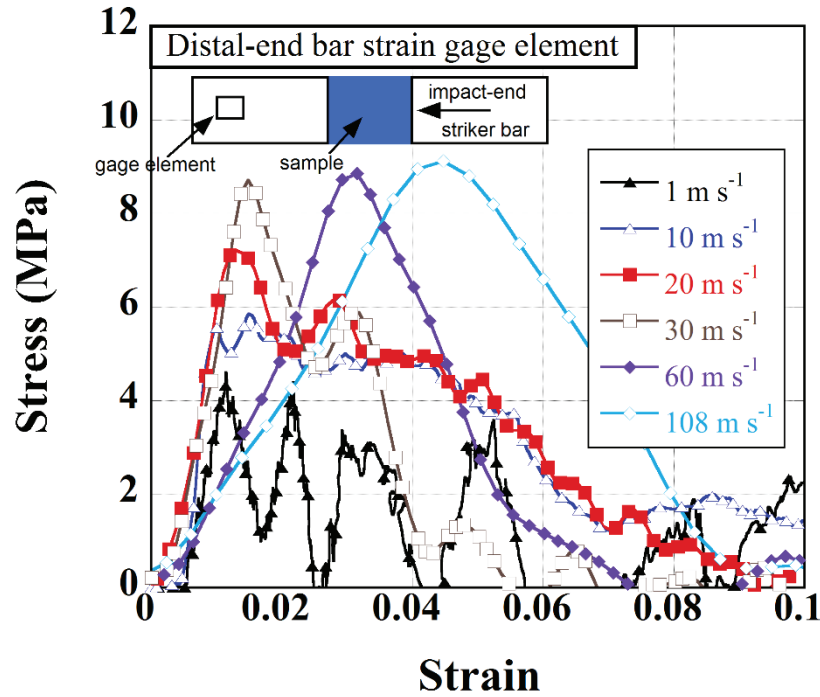
(c)

Figure 5.11. The stress-strain curves of the distal-end: (a) center element, (b) surface element and (c) SHPB gage strain

Figure 5.12(a-b) show the experimental mean DIF together with the stress triaxiality of the distal end and impact-end center and surface element as function of strain rate, respectively. The stress triaxiality is 0.33 for the uniaxial state of stress and 0.66 for the uniaxial state of strain (Appendix). The numerical stress triaxiality at the center element increases with increasing strain rate and reaches a steady value of 0.66 after about 1000 s^{-1} (Figure 5.12(a)). The increase of stress triaxiality at the surface element is more gradual and reaches a value of 0.43 at 1000 s^{-1} (30 m s^{-1}). This tends to prove a higher pressure development at the center of the specimen due to axial inertia. The increase in stress triaxiality is also more pronounced after about 30 s^{-1} (1 m s^{-1}). Somewhat a similar trend of the stress triaxiality with the strain rate is also seen in the impact-end (Figure 5.12(b)), except a sudden rise of the surface element stress triaxiality is seen after about 385 s^{-1} (10 m s^{-1}). The numerical results clearly indicated a full uniaxial state of strain attainment in the numerically tested sample after about 1000 s^{-1} (30 m s^{-1}).
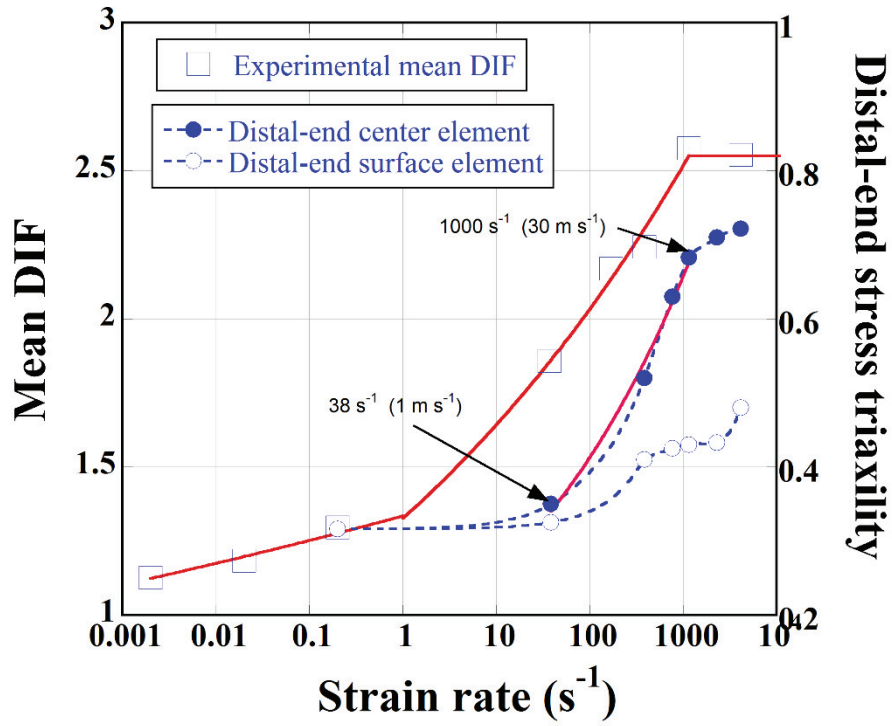
(a)
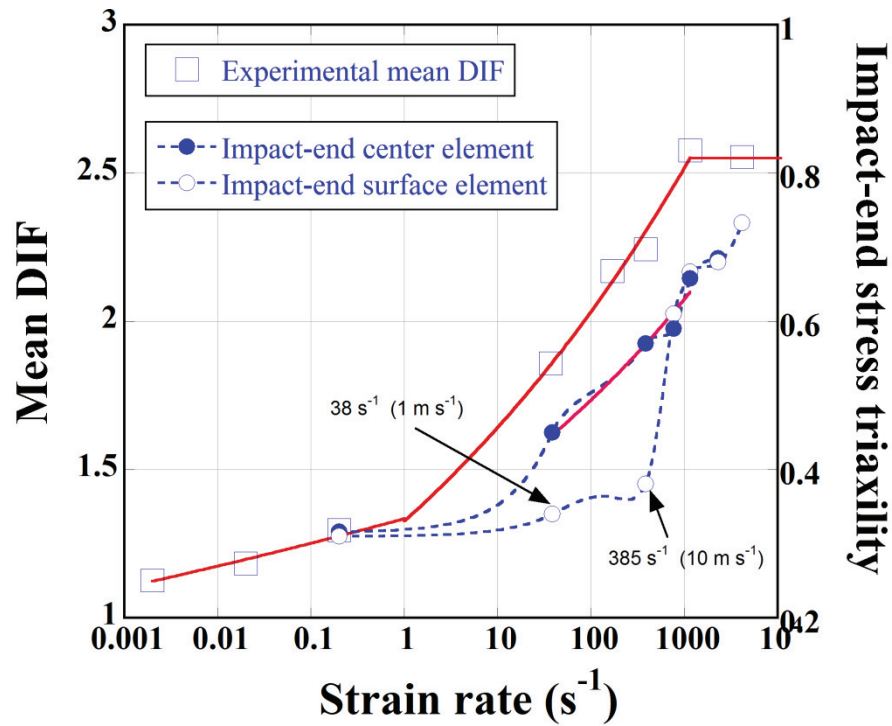
(b)

Figure 5.12. Experimental mean DIF and stress triaxiality vs strain rate (a) distal-end and (b) impact-end center and surface element

The variations of the distal and impact-end center element stress triaxiality with strain rate are shown in Figure 5.13. In the same figure, the variations of the experimental and numerical distal and impact-end contact DIF with strain rate are also shown for comparison. The increase of center element stress triaxiality with strain rate starts earlier in the impact-end than the distal-end. But, they reach the same value at about 1000 s^{-1}. The numerical contact-end stresses are very similar until about 385 s^{-1} (10 m s^{-1}); after which the impact-end contact stress increases significantly over the distal-end contact stress as shown in the same figure. This results are very much consistent with the previous numerical modelling studies on the concrete where 1D stress state was reported at 47 s^{-1} and 1D strain state ~795 s^{-1} when v=0.2 [68]. In the present study, a higher strain rate for the 1D strain state was determined since the sample diameter was smaller than the sample size modelled in reference [68].
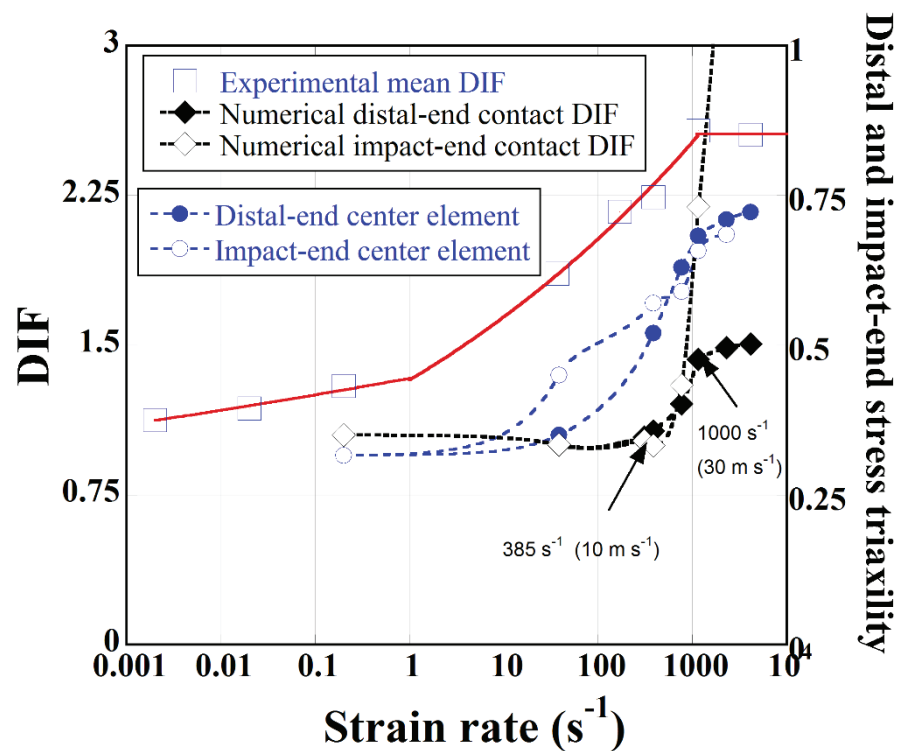
Figure 5.13. Experimental and numerical DIF values and the stress triaxiality vs strain rate

CHAPTER 6

CONCLUSIONS

The mechanical behavior of AAC samples at increasing strain rates from quasi-static ($1x10^{-3}$ s^{-1}) to dynamic strain (4150 s^{-1}) rates was investigated both experimentally and numerically. The numerical models of the experimental tests performed at different strain rates were also implemented in order to identify the effect of inertia on the compressive strength at increasing strain rates. Various test methods were used in the thesis including quasi-static and dynamic compression tests, quasi-static indentation tests, quasi-static and dynamic confined compression tests and quasi-static and dynamic Brazilian tests. The quasi-static compression tests were performed at the velocities between $5x10^{-5}$ to $5x10^{-3}$ m s^{-1}, corresponding to $2x10^{-3}$ and $2x10^{-1}$ s^{-1}. The low velocity impact tests were performed in a Drop Tower test set-up at a velocity of 1 m s^{-1} corresponding to ~30 s^{-1}. The dynamic compression tests were performed in a compression type SHPB at the velocities between 8 and 108 m s^{-1}, corresponding to 180 and 4150 s^{-1}. The numerical models of these tests were further implemented at the same velocities using a strain rate independent material model in order to determine solely the effect of inertia on the compressive strength. The confined compression and indentation tests were performed to determine the strength behavior in the uniaxial state of strain and the Brazilian tests the tensile strength variations at different strain rates.

The compression tests clearly indicated three distinct regions of compressive strength dependence on strain rate. A lower strain rate dependent crushing stress was determined in the quasi-static strain rate-regime, $2x10^{-3}$-$2x10^{-1}$ s^{-1}, a higher strain rate dependent crushing stress in the dynamic strain rate-regime, 180-10^3 s^{-1} and a cut-off stress above 10^3 $s^{-1.}$ The DIF varied between 1 and 2.5 from static to dynamic strain rate-regime with a sudden increase after about 100 s^{-1}. The indentation tests at quasi-static strain rate-regime however showed moderate DIF (1-1.13), very similar with those of the quasi-static compression strain-rate regime (1-1.15). The confinement tests

between 2×10^{-3}-380 s^{-1} resulted in a DIF of 1.35 at 380 s^{-1}, lower than the DIF of the compression test at the same strain rate, 2.04. These experimental results clearly indicated that the indentation and confinement tests decreased the DIF significantly and also confirmed the numerically determined DIF of concrete at 1000 s^{-1} (~1.30) without radial and axial inertia. The compression (1 and 8 m s^{-1}) and direct impact (10, 20, 30, 60 and 108 m s^{-1}) tests in the SHPB set-up were implemented numerically in LS-DYNA using an anisotropic material model, MAT_096 (MAT BRITTLE DAMAGE), with no strain rate sensitivity. The stress readings at different velocities at the fracture strength were performed at the specimen bar contacts, at the center and near the surface of the sample at sample/bar contact area and from the strain gage locations of the SHPB. The stress readings at the facture indicated that radial and axial inertia were dominant between 1 and 30 m s^{-1}, corresponding to the strain rates between 100-1000 s^{-1}.

APPENDIX A

DEFINITION OF THE STRESS TRIAXIALITY

The stress triaxiality discussed in Section 5.2 is defined as,

$$\eta_{1D\ stress} = \frac{\sigma_x + \sigma_y + \sigma_z}{3\sigma_{eq}}$$

(A.1)

where σ_x, σ_y and σ_z are stresses on x, y and z directions, while σ_{eq} is equivalent stress. The sum of the stresses in different directions represents the hydrostatic pressure on the sample.

The equivalent stress in the Von-Misses criterion is expressed as the following equation

$$\sigma_{eq} = \frac{1}{\sqrt{2}} \left[(\sigma_x - \sigma_y)^2 + (\sigma_y - \sigma_z)^2 + (\sigma_z - \sigma_x)^2 + 6(\tau_{xy}^2 + \tau_{yz}^2 + \tau_{xz}^2) \right]^{\frac{1}{2}}$$

(A.2)

In quasi-static tests, the equivalent stress is the same with the stress on x-direction (impact direction) since there is no stress in another direction and shearing stresses are zero.

$$\sigma_x = \sigma_{eq}$$

(A.3)

$$\eta_{1D\ stress} \approx 0.33$$

(A.4)

In high strain rate tests, strain in the y and z directions are zero, assuming with the impact loading in x-direction. Because of the confinement effect at dynamic loadings, the stresses in the y and z-directions are not zero and they are equal to each other. The superposition of components of strain in x, y and z-directions are

$$\varepsilon_x = \frac{1}{E}\left[\sigma_x - v(\sigma_y + \sigma_z)\right]$$

$$\varepsilon_y = \frac{1}{E}\left[\sigma_y - v(\sigma_z + \sigma_x)\right]$$

$$\varepsilon_z = \frac{1}{E}\left[\sigma_z - v(\sigma_x + \sigma_y)\right]$$

(A.5)

where v is Poisson's ratio. As the strain values in the y and z-direction are zero,

$$\sigma_y = \sigma_z = \frac{v\sigma_x}{1 - v}$$

(A.6)

Therefore, the equivalent stress and stress triaxiality on the sample at high strain rates according to the Von-Misses criterion,

$$\sigma_{eq} = \frac{\sigma_x(1 - 2v)}{1 - v}$$

(A.7)

$$\eta = \frac{1 + v}{3(1 - 2v)}$$

(A.8)

In this study, the Poisson's ratio of the AAC was taken 0.2 and thereby,

$$\eta_{1D\ strain} \approx 0.66$$

(A.9)

The equivalent stress in the Tresca criterion is

$$\sigma_{eq} = 2\tau_{max} = \sigma_x - \sigma_z$$

(A.10)

and the same equation (A.7) is reached for the equivalent stress.

REFERENCES

1. Isu, N.; Teramura, S.; Ishida, H.; Mitsuda, T., Influence of quartz particle size on the chemical and mechanical properties of autoclaved aerated concrete (II) fracture toughness, strength and micropore. *Cement and Concrete Research* 1995, *25* (2), 249-254.

2. Hamad, A. J., Materials, production, properties and application of aerated lightweight concrete. *International Journal of Materials Science and Engineering* 2014, *2* (2), 152-157.

3. Nian, W.; Subramaniam, K. V.; Andreopoulos, Y., Experimental investigation on blast response of cellular concrete. *International Journal of Impact Engineering* 2016, *96*, 105-115.

4. Scheffler, M.; Colombo, P., Cellular ceramics. *Structure, Manufacturing, Properties and Applications* 2005, 670.

5. Wan, H.; Hu, Y.; Liu, G.; Qu, Y., Study on the structure and properties of autoclaved aerated concrete produced with the stone-sawing mud. *Construction and Building Materials* 2018, *184*, 20-26.

6. Liu, Y.; Leong, B. S.; Hu, Z.-T.; Yang, E.-H., Autoclaved aerated concrete incorporating waste aluminum dust as foaming agent. *Construction and Building Materials* 2017, *148*, 140-147.

7. Song, Y.; Li, B.; Yang, E.-H.; Liu, Y.; Ding, T., Feasibility study on utilization of municipal solid waste incineration bottom ash as aerating agent for the production of autoclaved aerated concrete. *Cement and Concrete Composites* 2015, *56*, 51-58.

8. Ramamurthy, K.; Narayanan, N., Influence of composition and curing on drying shrinkage of aerated concrete. *Materials and Structures* 2000, *33* (228), 243-250.

9. Kunchariyakun, K.; Asavapisit, S.; Sombatsompop, K., Effect of Fine Al-Containing Waste in Autoclaved-Aerated Concrete Incorporating Rice-Husk Ash. *Journal of Materials in Civil Engineering* 2014, *27* (8), 04014220.

10. Qu, X. L.; Zhao, X. G., Previous and present investigations on the components, microstructure and main properties of autoclaved aerated concrete - A review. *Construction and Building Materials* 2017, *135*, 505-516.

11. Malaszkiewicz, D.; Chojnowski, J., Influence of addition of calcium sulfate dihydrate on drying of autoclaved aerated concrete. *Open Eng.* 2017, *7* (1), 273-278.

12. Huang, X. Y.; Ni, W.; Cui, W. H.; Wang, Z. J.; Zhu, L. P., Preparation of autoclaved aerated concrete using copper tailings and blast furnace slag. *Construction and Building Materials* 2012, *27* (1), 1-5.

13. Cong, X.; Lu, S.; Yao, Y.; Wang, Z., Fabrication and characterization of self-ignition coal gangue autoclaved aerated concrete. *Materials & Design* 2016, *97*, 155-162.

14. Li, X. G.; Liu, Z. L.; Lv, Y.; Cai, L. X.; Jiang, D. B.; Jiang, W. G.; Jian, S. W., Utilization of municipal solid waste incineration bottom ash in autoclaved aerated concrete. *Construction and Building Materials* 2018, *178*, 175-182.

15. Hauser, A.; Eggenberger, U.; Mumenthaler, T., Fly ash from cellulose industry as secondary raw material in autoclaved aerated concrete. *Cement and Concrete Research* 1999, *29* (3), 297-302.

16. Baltakys, M.; Siauciunas, R.; Eisinas, A., Influence of hardening conditions of autoclaved aerated concrete on tobermorite formation. *Rev. Rom. Mat.* 2017, *47* (4), 455-461.

17. Baspinar, M. S.; Demir, I.; Kahraman, E.; Gorhan, G., Utilization potential of fly ash together with silica fume in autoclaved aerated concrete production. *KSCE J. Civ. Eng.* 2014, *18* (1), 47-52.

18. Isu, N.; Ishida, H.; Mitsuda, T., Influence of quartz particle size on the chemical and mechanical properties of autoclaved aerated concrete (II) fracture toughness, strength and micropore. *Cement and Concrete Research* 1995, *25* (2), 243-248.

19. Kurama, H.; Topcu, I. B.; Karakurt, C., Properties of the autoclaved aerated concrete produced from coal bottom ash. *J. Mater. Process. Technol.* 2009, *209* (2), 767-773.

20. Mostafa, N. Y., Influence of air-cooled slag on physicochemical properties of autoclaved aerated concrete. *Cement and Concrete Research* 2005, *35* (7), 1349-1357.

21. Rasheed, M. A.; Prakash, S. S., Behavior of hybrid-synthetic fiber reinforced cellular lightweight concrete under uniaxial tension–Experimental and analytical studies. *Construction and Building Materials* 2018, *162*, 857-870.

22. Song, Y.; Li, B.; Yang, E.-H.; Liu, Y.; Chen, Z., Gas generation from incinerator bottom ash: potential aerating agent for lightweight concrete production. *Journal of Materials in Civil Engineering* 2016, *28* (7), 04016030.

23. Fapohunda, C.; Ikponmwrosa, E.; Falade, F., Evaluation of strength relations in foamed aerated concrete ntaining pulverized bone (PB) as a partial replacement of cement. *Engineering Review* 2018, *38* (1), 20-29.

24. Pehlivanlı, Z. O.; Uzun, İ.; Yücel, Z. P.; Demir, İ., The effect of different fiber reinforcement on the thermal and mechanical properties of autoclaved aerated concrete. *Construction and Building Materials* 2016, *112*, 325-330.

25. Dey, V.; Bonakdar, A.; Mobasher, B., Low-velocity flexural impact response of fiber-reinforced aerated concrete. *Cem. Concr. Compos.* 2014, *49*, 100-110.

26. Serrano-Perez, J. C.; Vaidya, U. K.; Uddin, N., Low velocity impact response of autoclaved aerated concrete/CFRP sandwich plates. *Compos. Struct.* 2007, *80* (4), 621-630.

27. Bonakdar, A.; Babbitt, F.; Mobasher, B., Physical and mechanical characterization of Fiber-Reinforced Aerated Concrete (FRAC). *Cem. Concr. Compos.* 2013, *38*, 82-91.

28. Pehlivanli, Z. O.; Uzun, I.; Demir, I., Mechanical and microstructural features of autoclaved aerated concrete reinforced with autoclaved polypropylene, carbon, basalt and glass fiber. *Construction and Building Materials* 2015, *96*, 428-433.

29. Wang, B.; Wang, P.; Chen, Y.; Zhou, J.; Kong, X.; Wu, H.; Fan, H.; Jin, F., Blast responses of CFRP strengthened autoclaved aerated cellular concrete panels. *Construction and Building Materials* 2017, *157*, 226-236.

30. ASTM, C., Standard test method for compressive strength of cylindrical concrete specimens. 2012.

31. Gibson, L. J.; Ashby, M. F., Cellular Solids: Structure and Properties. 2 ed.; *Cambridge University Press*: Cambridge, 1997.

32. J. Newman, B. S. C., and P. Owens, , Advanced Concrete Technology Processes. *Elsevier Ltd*: 2003.

33. Hu, W.; Neufeld, R. D.; Vallejo, L. E.; Kelly, C.; Latona, M., Strength properties of autoclaved cellular concrete with high volume fly ash. *Journal of energy engineering* 1997, *123* (2), 44-54.

34. Jin, H.-Q.; Yao, X.-L.; Fan, L.-W.; Xu, X.; Yu, Z.-T., Experimental determination and fractal modeling of the effective thermal conductivity of autoclaved aerated

concrete: Effects of moisture content. *International journal of heat and mass transfer* 2016, *92*, 589-602.

35. Jerman, M.; Keppert, M.; Výborný, J.; Černý, R., Hygric, thermal and durability properties of autoclaved aerated concrete. *Construction and Building Materials* 2013, *41*, 352-359.

36. Wilsea, M.; Johnson, K.; Ashby, M., Indentation of foamed plastics. *International Journal of Mechanical Sciences* 1975, *17* (7), 457-IN6.

37. Timoshenko, S.; Goodier, J. N., *Theory of Elasticity, by S. Timoshenko and J.N. Goodier, ... 2nd Edition*. McGraw-Hill Book Company: 1951.

38. Kou, S.-Q.; Huang, Y.; Tan, X.-C.; Lindqvist, P.-A., Identification of the governing parameters related to rock indentation depth by using similarity analysis. *Eng. Geol.* 1998, *49* (3-4), 261-269.

39. Yankelevsky, D. Z.; Avnon, I., Autoclaved aerated concrete behavior under explosive action. *Construction and Building Materials* 1998, *12* (6-7), 359-364.

40. Mespoulet, J.; Plassard, F.; Hereil, P. L., Strain rate sensitivity of autoclaved aerated concrete from quasi-static regime to shock loading. In *Dymat 2015 - 11th International Conference on the Mechanical and Physical Behaviour of Materials under Dynamic Loading*, Cadoni, E., Ed. E D P Sciences: Cedex A, 2015; Vol. 94.

41. Khosravani, M. R.; Weinberg, K., A review on split Hopkinson bar experiments on the dynamic characterisation of concrete. *Construction and Building Materials* 2018, *190*, 1264-1283.

42. Lee, S.; Kim, K. M.; Park, J.; Cho, J. Y., Pure rate effect on the concrete compressive strength in the split Hopkinson pressure bar test. *International Journal of Impact Engineering* 2018, *113*, 191-202.

43. Lv, T.; Chen, X.; Chen, G., Analysis on the waveform features of the split Hopkinson pressure bar tests of plain concrete specimen. *International Journal of Impact Engineering* 2017, *103*, 107-123.

44. Ravichandran, G.; Subhash, G., Critical appraisal of limiting strain rates for compression testing of ceramics in a Split Hopkinson Pressure Bar. *J. Am. Ceram. Soc.* 1994, *77* (1), 263-267.

45. Ai, D. H.; Zhao, Y. C.; Wang, Q. F.; Li, C. W., Experimental and numerical investigation of crack propagation and dynamic properties of rock in SHPB indirect tension test. *International Journal of Impact Engineering* 2019, *126*, 135-146.

46. Chen, J. Y.; Xiang, D.; Wang, Z. H.; Wu, G. Y.; Wang, G. W., Dynamic tensile strength enhancement of concrete in split Hopkinson pressure bar test. *Adv. Mech. Eng.* 2018, *10* (6), 7.

47. Atiezo, M. K.; Chen, W.; Dascalu, C., Loading rate effects on dynamic failure of quasi-brittle solids: Simulations with a two-scale damage model. *Theor. Appl. Fract. Mech.* 2019, *100*, 269-280.

48. Weibull, W., A statistical distribution function of wide applicability. *Journal of applied mechanics* 1951, *18* (3), 293-297.

49. Pan, X. H.; Xiong, Q. Q.; Wu, Z. J., New Method for Obtaining the Homogeneity Index m of Weibull Distribution Using Peak and Crack-Damage Strains. *Int. J. Geomech.* 2018, *18* (6), 20.

50. Li, Z.; Chen, L.; Fang, Q.; Hao, H.; Zhang, Y.; Chen, W.; Xiang, H.; Bao, Q., Study of autoclaved aerated concrete masonry walls under vented gas explosions. *Engineering Structures* 2017, *141*, 444-460.

51. Halquist, J., LS-DYNA keyword user's manual version 971. *Livermore Software Technology Corporation, Livermore, CA* 2007.

52. Oliver, J., A consistent characteristic length for smeared cracking models. *Int. J. Numer. Methods Eng.* 1989, *28* (2), 461-474.

53. Govindjee, S.; Kay, G. J.; Simo, J. C., Anisotropic modelling and numerical simulation of brittle damage in concrete. *Int. J. Numer. Methods Eng.* 1995, *38* (21), 3611-3633.

54. Bischoff, P. H.; Perry, S. H., Compressive behaviour of concrete at high strain rates. *Materials and Structures* 1991, *24* (144), 425-450.

55. Zhang, Q. B.; Zhao, J., A Review of Dynamic Experimental Techniques and Mechanical Behaviour of Rock Materials. *Rock Mech. Rock Eng.* 2014, *47* (4), 1411-1478.

56. Plauk, G., Concrete structures under impact and impulsive loading. 1982.

57. Lu, D. C.; Wang, G. S.; Du, X. L.; Wang, Y., A nonlinear dynamic uniaxial strength criterion that considers the ultimate dynamic strength of concrete. *International Journal of Impact Engineering* 2017, *103*, 124-137.

58. Rossi, P.; Toutlemonde, F. J. M.; Structures, Effect of loading rate on the tensile behaviour of concrete: description of the physical mechanisms. 1996, *29* (2), 116.

59. Lindholm, U. S.; Yeakley, L. M.; Nagy, A., The dynamic strength and fracture properties of dresser basalt. *International Journal of Rock Mechanics and Mining Sciences & Geomechanics Abstracts* 1974, *11* (5), 181-191.

60. Reinhardt, H. W.; Rossi, P.; van Mier, J. G. M. J. M.; Structures, Joint investigation of concrete at high rates of loading. 1990, *23* (3), 213-216.

61. Wang, Q. F.; Liu, Y. H.; Peng, G., Effect of water pressure on mechanical behavior of concrete under dynamic compression state. *Construction and Building Materials* 2016, *125*, 501-509.

62. Rossi, P. J. M.; Structures, A physical phenomenon which can explain the mechanical behaviour of concrete under high strain rates. 1991, *24* (6), 422-424.

63. E.D.H. Davies; Hunter, S. C., The dynamic compression testing of solids by the method of the split Hopkinson pressure bar. *Journal of the Mechanics and Physics of Solids* 1963, *11* (3), 155-179.

64. Brace, W. F.; Jones, A. H., Comparison of uniaxial deformation in shock and static loading of three rocks. *Journal of Geophysical Research* 1971, *76* (20), 4913-&.

65. Sfer, D.; Carol, I.; Gettu, R.; Etse, G., Study of the behavior of concrete under triaxial compression. *J. Eng. Mech.-ASCE* 2002, *128* (2), 156-163.

66. Grady, D. E., Shock-wave compression of brittle solids. *Mechanics of Materials* 1998, *29* (3), 181-203.

67. Yu, S. S.; Lu, Y. B.; Cai, Y., The strain-rate effect of engineering materials and its unified model. *Lat. Am. J. Solids Struct.* 2013, *10* (4), 833-844.

68. Liu, F.; Li, Q. M., Strain-rate effect on the compressive strength of brittle materials and its implementation into material strength model. *International Journal of Impact Engineering* 2019, *130*, 113-123.